

Master Thesis, Department of Geosciences

Sedimentology, petrology and geochemistry of the Kilimatinde Cement, central Tanzania

Katrine Fossum



UNIVERSITY OF OSLO

FACULTY OF MATHEMATICS AND NATURAL SCIENCES

Sedimentology, petrology and geochemistry of the Kilimatinde Cement, central Tanzania

Katrine Fossum



Master Thesis in Geosciences

Discipline: Geology

Department of Geosciences

Faculty of Mathematics and Natural Sciences

University of Oslo

August, 2012

© **Katrine Fossum 2012**

This work is published digitally through DUO – Digitale Utgivelser ved UiO

<http://www.duo.uio.no>

It is also catalogued in BIBSYS (<http://www.bibsys.no/english>)

All rights reserved. No part of this publication may be reproduced or transmitted, in any form or by any means, without permission.

Acknowledgments

First, I would like to express my gratitude to NORAD for their financial support during this project. I will forever be grateful for the opportunity of being a part of this; both for the field experience and...

I want to thank professors Dr. Charles Kaaya and Dr. Nelson Boniface at the University of Dar Es Salaam for making me feel welcome in their country their assistance in the field. Our driver, Abbas, also deserves “a thank you” for providing safe transportation along the many bumpy roads between field locations. Professor Arild Andresen, PhD-student Lars Riber, and my fellow master student Synnøve Knivslund deserve thanks for their great company during the two field weeks in Tanzania. I would like to give special gratitude to Arild Andresen for his field teaching in structural geology and Lars Riber for assisting me in the field. The cold Safari-beer in the bar after a long, warm day in the field will be something to remember.

Thank you to Mofak Naoroz for teaching me how to operate the diamond saw and the sling mill; Maarten Aerts for running my XRD`s; Berit Løken Berg, for assisting me during SEM analysis; and Muriel Erambert, for Electron microprobe analysis. I always enjoyed spending time in the basement with these cheerful ladies.

To my supportive and loving family who have helped and encouraged me throughout my academic years, especially my father who has always believed in me. I want to express my gratitude to my beloved Gjermund for your support, encouragement, always putting the smile back on my face when coming home. You all made this a lot easier for me. And, of course my dog Peanut for walking me in the park.

Last, I would not have written this thesis if it were not for my professor and supervisor Henning Dypvik. You have been a great inspiration to me for many years now. Thank you for giving me the chance to be a part of this, for your open-door policy, for your helpful guidance, support, and understanding throughout this year. If it were not for your inspiring lectures, I would have become a paleontologist. Thank you!

Abstract

Two sites (Saranda and Chiguluka) were examined to assess the depositional environment and diagenetic history of the Kilimatinde Cement deposits. The surficial deposits of the Kilimatinde Cement, mapped as silcretes and calcretes, are situated in the semi-arid central Tanzania, in the Dodoma and Singida regions. The Cement has not been dated but is assumed to be possibly Late Miocene to Early Pliocene in age. The Cement is known to locally contain uranium, and is being mined for this purpose in several places within the region.

The study area is situated at the southern extent of the East African Rift System, which consequently affects the sedimentation process in the area.

Sedimentary field data combined with petrographical and mineralogical studies (thin section analysis, XRD, SEM, and EMP) have been used to interpret the depositional environment. The Saranda profile is roughly an upwards coarsening succession, and is highly cemented by silica. The profile can be divided into three units on the basis of lithology and mineralogical composition. The lower section, composed mainly of a greenish gray sandy siltstone, has been interpreted to be of lacustrine origin. The sandy middle section is of fluvial origin, while the upper section is made of valley fill sediment. The surface and the interior of the upper section deposits are composed of irregular, rounded glaebules. The glaebules have been formed *in situ* by pedogenic processes and display geopetal structures, indicating their formation through mineral accretion related to hydration/dehydration of the unconsolidated sand.

Both groundwater and pedogenic silcretes have been recognized in the Saranda profile.

Opal has precipitated from silica-rich groundwaters in the lower section, and is classified as a groundwater silcrete. The middle and upper section are classified as pedogenic silcretes and have been silicified by the downward percolation of silica-saturated solutions.

Opal is restricted within the lower and middle sections, with several stages of silicification having been recognized. The earliest phase of silicification is noted as the replacement of sedimentary clays by opal-A. Dissolution and re-precipitation leads to the formation of increasingly well-ordered opal-CT, and the eventual development of chalcedony in

residual cavities. Opal-CT commonly occurs as opal-CT lepispheres in the middle and lower sections. The upper section does not contain any opal, and has been cemented by microcrystalline quartz indicating precipitation from solutions that are undersaturated with respect to opal-A or opal-CT.

Trace element analysis reveals uranium enrichments in the Saranda profile. The lower section shows extreme enrichments, the highest recorded values being 94 and 394 ppm. Uranium-bearing minerals have not been found in any samples, which indicate uranium absorption on clay minerals, but also apatite. The highest uranium distributions however have been found in samples containing apatite.

The lower section has a contrasting mineralogical composition comparatively to the middle and upper sections. Heavy minerals in the lower section have been studied using SEM and EMP, and strongly suggest a kimberlitic source with the presence of Cr-spinels, Mg-rich ilmenite, and Cr-garnet. The middle and upper sections display a granitic signature with the dominance of quartz, K-spar, and kaolinite.

Contents

1	INTRODUCTION.....	6
1.1	PURPOSE OF STUDY.....	6
1.1.1	<i>Project description and main objectives.....</i>	<i>7</i>
1.1.2	<i>Purpose of study.....</i>	<i>7</i>
1.2	GEOGRAPHIC SETTING AND CLIMATE.....	8
1.3	GEOLOGICAL FRAMEWORK.....	9
1.3.1	<i>Geology of Tanzania.....</i>	<i>9</i>
1.3.2	<i>Regional Geological Setting.....</i>	<i>14</i>
1.3.3	<i>The Kilimatinde Cement.....</i>	<i>17</i>
1.4	THEORETICAL BACKGROUND.....	19
1.4.1	<i>Silcrete.....</i>	<i>19</i>
1.4.2	<i>Silica polymorphs.....</i>	<i>23</i>
2	METHODS AND MATERIALS.....	28
2.1	FIELDWORK.....	28
2.2	FACIES AND FACIES ASSOCIATIONS.....	29
2.3	PETROGRAPHICAL AND MINERALOGICAL ANALYSIS.....	30
2.3.1	<i>Thin sections.....</i>	<i>30</i>
2.3.2	<i>Point counting and rock characteristics.....</i>	<i>30</i>
2.3.3	<i>X-ray diffraction analysis (XRD).....</i>	<i>33</i>
2.3.4	<i>Scanning Electron Microscope (SEM).....</i>	<i>35</i>
2.3.5	<i>Electron microprobe.....</i>	<i>35</i>
2.4	TRACE ELEMENT GEOCHEMISTRY.....	36
3	SARANDA RESULTS.....	38
3.1	FACIES DESCRIPTION, AND FACIES ASSOCIATIONS.....	38
3.1.1	<i>Facies description.....</i>	<i>40</i>
3.1.2	<i>Facies associations.....</i>	<i>43</i>
3.2	PETROGRAPHICAL AND MINERALOGICAL ANALYSIS.....	49
3.2.1	<i>Thin section analysis, and point counting.....</i>	<i>49</i>

3.2.2	<i>XRD results</i>	58
3.2.3	<i>SEM, and electron microprobe results</i>	63
3.3	TRACE ELEMENT GEOCHEMISTRY.....	72
3.3.1	<i>Element concentrations</i>	72
3.3.2	<i>Rare earth elements (REE)</i>	74
3.3.3	<i>Th/U ratios, and the distribution of Ni and Cr</i>	75
4	CHIGULUKA RESULTS	77
5	DISCUSSION	90
5.1	DEPOSITIONAL ENVIRONMENT.....	90
5.2	MINERALOGICAL COMPOSITION.....	92
5.2.1	<i>Lower sections</i>	93
5.2.2	<i>Middle section</i>	93
5.2.3	<i>Upper section</i>	94
5.3	NODULE FORMATION.....	95
5.3.1	<i>Formation of concentric coatings on individual grains</i>	95
5.3.2	<i>Formations of glaebules</i>	97
5.3.3	<i>Development of nodular surface</i>	99
5.4	SILISIFICATION.....	100
5.5	SILCRETE CLASSIFICATION.....	104
5.5.1	<i>Groundwater silcretes</i>	105
5.5.2	<i>Pedogenic silcretes</i>	105
5.6	GEOCHEMISTRY.....	106
5.7	URANIUM.....	107
5.8	PROVENANCE.....	113
5.9	CHIGULUKA – similarities and differences.....	116

6	CONCLUSION.....	118
	References.....	121
	Appendices.....	129

1 Introduction

This thesis is a part of a joint international research project, PITRO III (Programme for Institutional Transformation, Research and Outreach), and is financed by the Norwegian Agency for Development Cooperation (NORAD). The project is a collaboration between the University of Oslo (UiO) and the University of Dar es Salaam (UDSM), United Republic of Tanzania, with the project title: Environmental geology and ground water dynamics in part of semi-arid area of central Tanzania.

1.1 Project description and objectives

The main purpose of this project is to address the groundwater problems in the Bahi Basin and adjacent areas, in the Singida and Dodoma regions in central Tanzania. Groundwater is the most important and reliable water source in the semi-arid parts of Tanzania. However, rift-associated toxic elements, like arsenic, fluoride, barium, and uranium, can occur in high concentrations within the groundwater in the area.

The main objectives of this project are:

- Study how geomorphology, sediment composition, and the structural grain influence the groundwater distribution in the area. Groundwater dynamics, accumulation, and water quality is of particular importance.
- Establishing a source area for the various toxic element, especially uranium, and to study the distribution and concentrations of these elements in sediments and soils.

By better understanding the groundwater circulation, the water resources can be utilized in a more efficient way. Hopefully, results from this project can be applied in the planning of new water wells in the area.

Purpose of M.Sc. study

The purpose of this thesis is to study the depositional environment and diagenetic history of the Kilimatinde Cement to obtain a better understanding of past groundwater circulations and related element enrichments. The Kilimatinde Cement has been defined as silcretes and

calcretes, and locally ferricrete, and it is assumed that precipitation from groundwater has played an important role in cementing these rocks. The Kilimatinde Cement is locally enriched in uranium. Uranium mining is currently ongoing in the area, with several new projects planned. Main objectives for this study are to determine the depositional environment and cementation processes, and the uranium distribution within these deposits.

Two field sites have been chosen for this thesis based upon geochemical data. The Saranda profile is the main objective in this thesis, due to its very high uranium distribution. The other site, Chiguluka, is not enriched in uranium or any other elements, and will be used as a comparison.

Participants from both universities carried out fieldwork in two field seasons in 2010 and 2011. Samples collected from the 2010 season were brought to Norway and analyzed by the author. In 2011, the author visited the three most interesting localities during fieldwork, and additional sampling was done. Of the three localities visited, two have been chosen for this thesis (Saranda and Chiguluka, Fig. 1.7) on the basis of time spent in the field, geochemical data and what is most relevant for this project. The Saranda profile is of particular interest since it is heavily enriched in toxic elements, especially uranium, and will be the main focus of this thesis. Because the Chiguluka profile does not show major enrichments and has a simple mineralogy compared to Saranda, the results from this locality will only be briefly described, and used as a comparison between the two profiles. Similarities and differences will be discussed.

This thesis is based upon data collected in the field that have been analyzed by XRD, thin section, and trace element geochemistry. An SEM and electron microprobe have been used for detail studies of some selected samples.

1.2 Geographic setting and Climate

The United Republic of Tanzania is situated in East Africa, just south of equator between latitudes 1° and 12° S and longitudes 29° and 41° E (Fig.1.1).



Figure 1.1 Map of The United Republic of Tanzania. The red square marks the study area. From United Nations (available at www.un.org/Depts/Cartographic/english/htmain.htm.)

Tanzania is bordered by Kenya and Uganda to the north; Rwanda, Burundi, and the Democratic Republic of the Congo to the west; Zambia, Malawi, and Mozambique to the south; and the Indian Ocean to the east.

The two field sites, Saranda and Chiguluka (Fig.1.6), are located in the Singida and Dodoma regions in the central part of the country, close to the political capital of Dodoma (Fig.1.1).

The Dodoma and Singida regions (Fig. 1.1) have a semi-arid climate, which is largely controlled by the movement of air masses associated with the inter-tropical convergence zone, McCartney (2007). The rainy seasons are of short duration and extend from December to March. Mean annual rainfall in the Bahi Basin is about 600 mm, while the mean potential evapotranspiration is approximately 1,620 mm/year. Additionally the mean annual temperature is 25°C (McCartney, 2007).

1.3 Geological framework

The geology of Tanzania is strongly dominated by Precambrian rocks as illustrated by Figure 1.2. The study area is situated on the Tanzania Craton, which forms the highest part of the East African Plateau and is mainly composed of Archean granitoids and metasediments, along with the rocks of Dodoman, Nyanzian, and Kavironian systems. The proterozoic rocks of Tanzania are situated as mobile belts that enclose the craton. These mobile belts are of various ages and have undergone different grades of metamorphism. The Cenozoic rift faults related to the East African Rift System are assumed to follow weak lines within these mobile belts.

1.3.1 Geology of Tanzania

Archean

The Archean rocks of Tanzania, which make up the Tanzania Craton, are an amalgamation of several terrains, some older than 3,000 Ma (Bell and Dodson 1981). The craton is situated in the central part of the country and consists mainly of granitoids, forming the “central plateau” of Tanzania (Fig.1.2). Three formations interfere with the granitoids, having distinct compositions and ages: the Dodoman, the Nyanzian, and the Kavironian (Figs.1.2, 1.3) (Bell & Dodson, 1981; Schlüter, 1997). Granites have intruded the craton and migmatized by three tectono-metamorphic events dated to 2,900, 2,700, and 2,400 Ma. A minor, intrusion has been dated to approx. 1,850 Ma, (Bell and Dodson, 1981; Chesley, 1999).

The *Dodoman System*, which is the oldest formation (Fig. 1.2, 1.3), is a small inlier of metasediments and metavolcanics, situated as elongated outcrops trending ESE-WNW (Fig. 1.2). The system is highly metamorphosed and has undergone amphibolite facies metamorphism (Bell and Dodson 1981).

The *Nyanzian System*, also known as the greenstone belt, is found in the area around Lake Victoria in the northern parts of Tanzania and is associated with gold bearing granites (Figs. 1.2, 1.3) (Schlüter, 1997). The system occurs as inliers of basic and siliceous volcanics with banded ironstones and other sediments within the granites, formed 2,550 - 3,150 Ma (Bell and Dodson, 1981). The metamorphic grade is not as high as those found within the Dodoman System, and has undergone greenschist facies metamorphism (Figs. 1.2, 1.3).

The *Kavirondian System* is limited to the Musoma district north of the Mara River, northernmost Tanzania (Fig.1.1) and is primarily composed of coarse sands and conglomerates, which unconformably overlie the Nyanzian System (Figs.1.2, 1.3). A period of granitic intrusions and folding separates the two systems, and the sedimentary rocks of the Kavirondian System have been interpreted as molasse deposits from the Nyanzian System (Schlüter, 1997).

Proterozoic

The Proterozoic rocks of Tanzania are identified as remnants of ancient orogenic belts that surround the craton (Figs.1.2, 1.3); the Ubendian system to the west and southwest, the Usagaran System to the southeast; the Mozambique belt east of the craton; the Karagwe-Ankolean to the west; and Bukoban System to the northwest (Nyblade *et al.* 1996; Schlüter, 1997; Owen *et al.*, 2000; Bellucci, 2011).

The Ubendian Belt is named after the Ubendian orogeny of 1,800-1,700 Ma, during the Paleoproterozoic Era, and is a linear, NW-SE elongated orogenic belt that forms the southwesterly margin of the Tanzania Craton (Figs. 1.2, 1.3) (Schlüter 1997; Boniface and Schenk 2012). The Ubendian System mainly consists of high-grade metamorphic rocks of sedimentary and igneous origin (Kilimanjaro Mining Company, 2008)

The Usagaran Belt is situated along the southeastern margin of the Tanzania Craton (Figs. 1.2, 1.3). The Usagaran mountain belt and suture developed as a result of a subducted plate below the more stable and cold Tanzania Craton (Möller *et al.* 1995). The dating of eclogites suggest that subduction took place approx. 2,000 Ma.

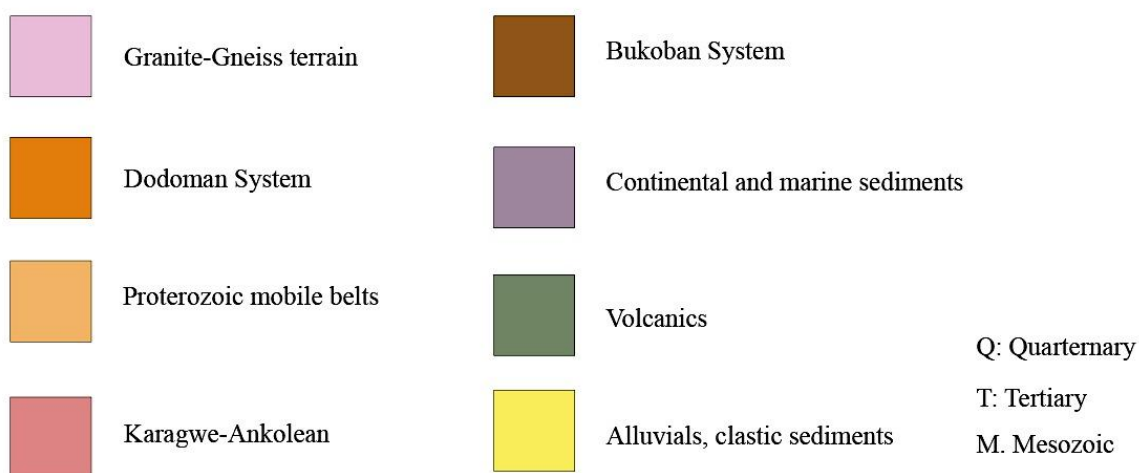
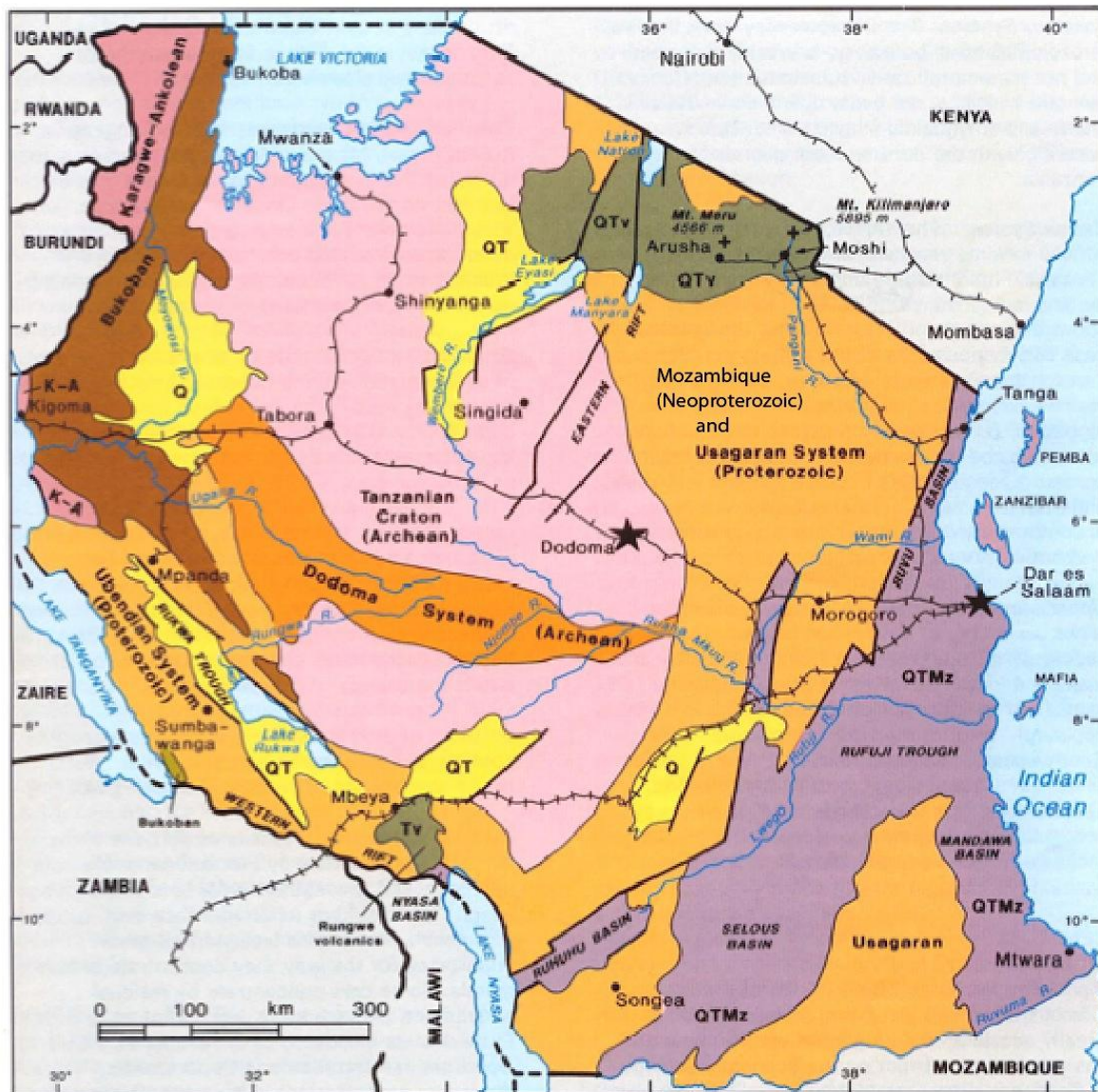


Figure 1.2 Generalized geological map of Tanzania, Semkiwa et al. (2005).

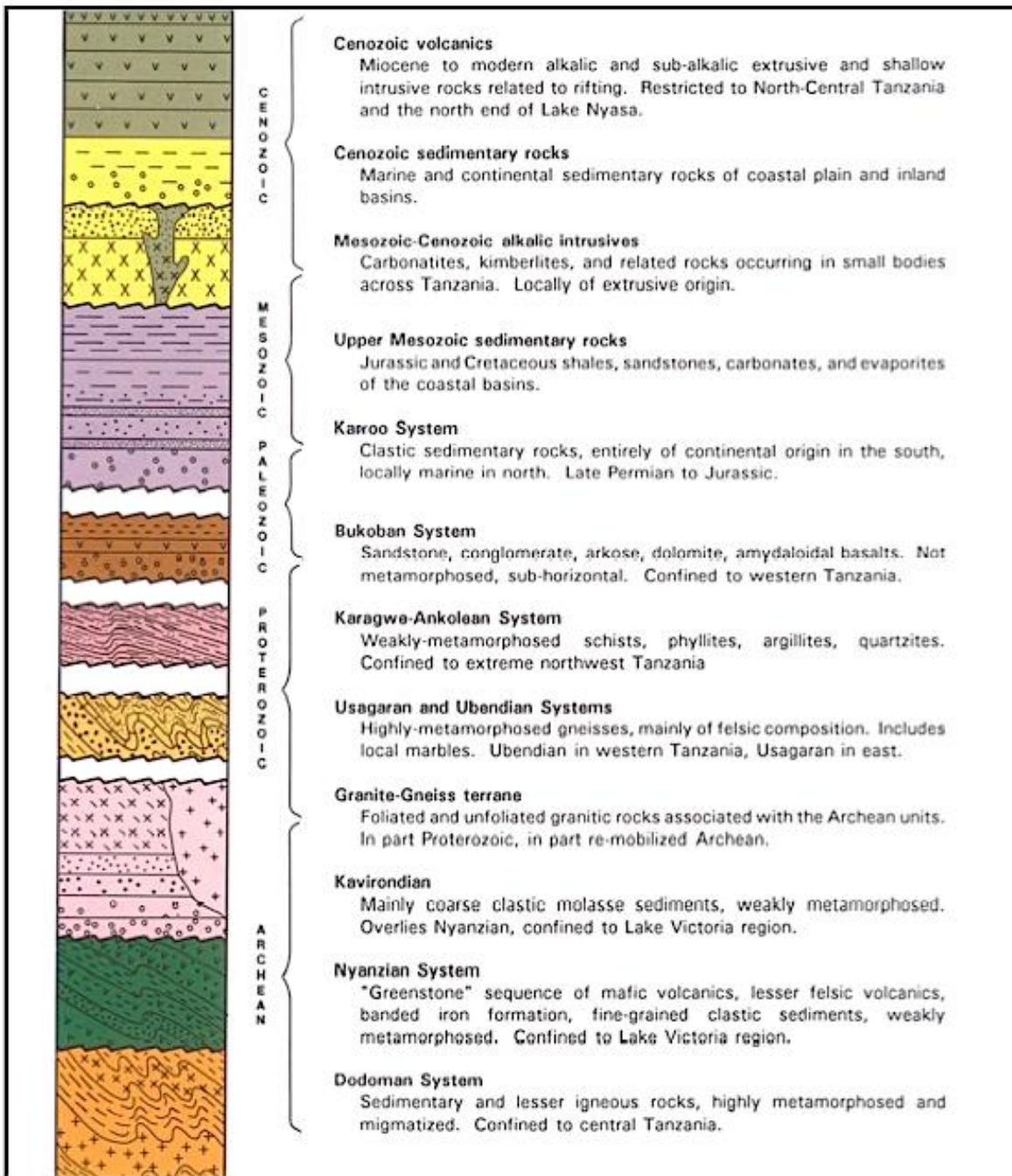


Figure 1.3 Simplified stratigraphical column displaying the main lithological units. Remark: Mozambique belt is not included in this illustration. From Semkiwa et al. (2005).

The belt is divided into two major lithological units: the Konse group composed of metasedimentary and metavolcanic rocks, and the gneissic-amphibolitic Isimani Suite (Schlüter 1997).

The N-S trending *Mozambique Belt* is the longest zone of crustal mobility in Africa and extends from Mozambique in the south to the Red Sea in the north (Schlüter, 1997). The belt lies to the east of the Tanzania Craton (Fig.1.2) and marks the suture between east and west Gondwana. It is comprised of the western granulite section of the Mozambique Belt and has been reworked during the Pan-African orogeny ca. 560 Ma (Cutten *et al.* 2006; Fritz *et al.* 2009). The metasediments and intrusions in the system have been subjected to intense deformation.

Paleozoic

After the Mozambiquan orogenic event, a long erosional interval followed, which resulted in a missing geological record from the Precambrian to Upper Paleozoic in Tanzania (Schlüter, 1997). During the time of the Carboniferous to Lower Jurassic, rocks belonging to the *Karoo Supergroup* were deposited in NE-SW trending half grabens (Fig. 1.2, 1.3, 1.4) (Schlüter, 1997; Wopfner, 2002).

Rocks of the *Karoo System* lie unconformably above the Precambrian rocks, and are known for their coal deposits. These are mainly continental

sediments deposited in intercratonic basins, although some grabens located in the coastal regions have been marine influenced the in Late Permian times (Kreuser *et al.*, 1990). The Karoo sediments can be divided into eight units (K1 to K8) on the basis of lithology (Schlüter 1997). The Ruhuhu Basin (Fig. 1.4), in the southwestern part of Tanzania, provides a typical depositional sequence of the Karoo basin in eastern Africa (Schlüter, 1997; Wopfner, 2002). In major portions of Godwana, a continental glaciation took place during the Carboniferous to Permian periods evident by tillites and varves with dropstones in the

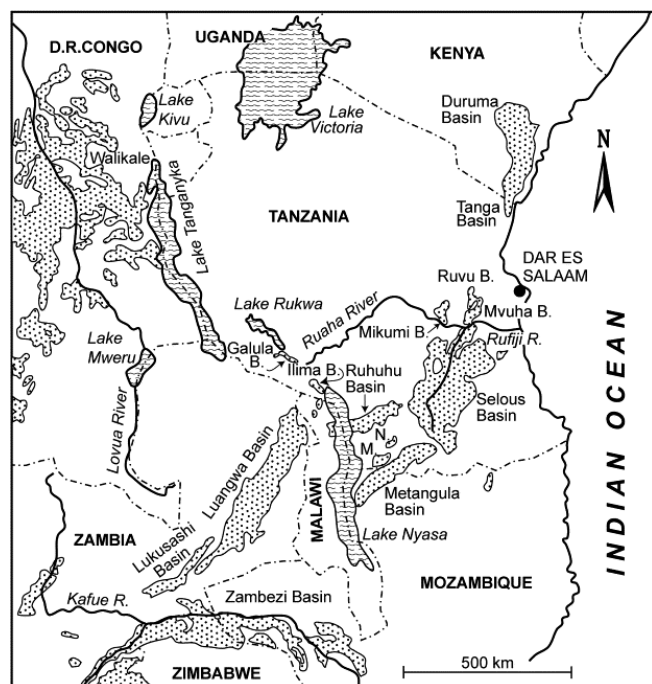


Figure 1.4 Locations of Karoo basins in eastern Africa (dotted areas). From Wopfner (2002)

lowermost (K1) Karoo formation (Schlüter, 1997). A change in climate from cold to semi-arid, to warm and temperate followed, and the K1 unit was overlain by fluvial-deltaic coal-bearing deposits and succeeded by arkoses and continental red beds (Wopfner, 2002).

Cenozoic

Paleogene rocks are only exposed in the southeastern part of coastal Tanzania, overlain by marine and continental Neogene rocks. The deposits are calcareous sandstones, limestones, grey clays, marls, and reef deposits (Schlüter, 1997). For See Schlüter (1997) for more information on these deposits. Cenozoic deposits (the Kilimatinde Cement) from the study area will be presented in chapter 1.3.3.

1.3.2 Regional geological setting

The East African Rift System, henceforth

referred to as *EARS*, is an active zone of continental rifting, which is a part of the Afro-Arabian Rift System originating at the Afar triple junction in the Red Sea (Fig.1.5). The Afro-Arabian Rift System stretches from Turkey in the east, to Mozambique in the south (Schlüter, 1997; Chorowicz, 2005). The area of study is situated in the southern limit of the EARS (Schlüter, 1997; Nyblade and Brazier, 2002).

The EARS contains several segments, which cut through the African continent. The two main branches, the western branch (known as the Ethiopian Rift) and the eastern branch (known as the Gregory or the Kenyan Rift) are wrapped around the Tanzania Craton (Figs. 1.5, 1.6) (Schlüter, 1997; Nyblade and Brazier, 2002; Dawson, 2008; Macheyekei, *et al.*, 2008; Bellucci *et al.*, 2011).

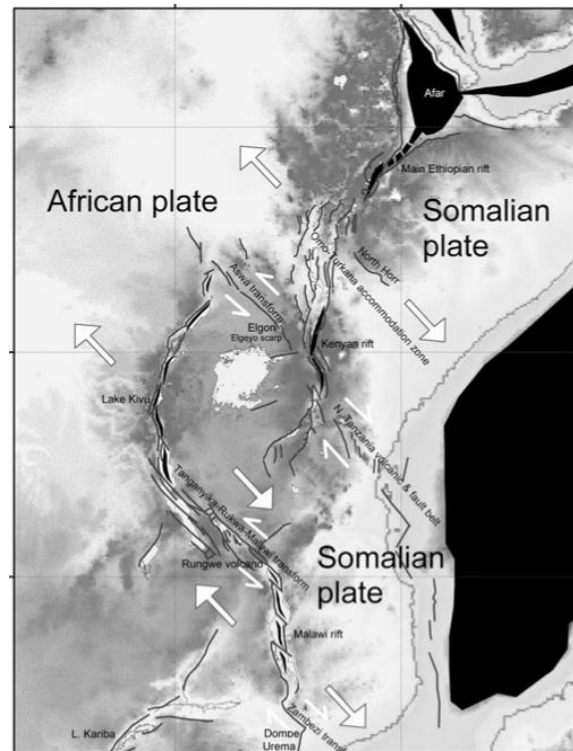


Figure 1.5 showing how the African and Somalian plates are pulling away from each other. The third plate, the Arabian, is situated north of the Afar triple junction. From Chorowicz (2005).

Rifting is discontinued where it reaches the base of the Tanzania Craton (Fig. 1.6). Nyblade and Braziers (2002) argue that the cold and thick lithosphere of the Craton has resisted modifications by the Cenozoic rifting and acted as an inflexible tectonic block during time of deformation. It is assumed that the propagating stress followed weak lines in the already deformed crust that surrounds the Craton. The Cenozoic rift faults have been found to extend along lines of former weakness in the mobile belts molded to the ancient shields (McConnel 1972; Chorowicz



Figure 1.6 Display who the two branches of the EARS is situated against the Tanzania craton. Modiefied from Chorowicz (2005)

2005). The two branches of the EARS show this stalling trend at the contact with the Tanzania Craton, and overlie these mobile belts (Schlüter 1997; Nyblade and Brazier 2002; Dawson 2008). The rift fades into the North Tanzanian Divergence, henceforth referred to *NTD*. South of the *NTD* the extension is less visible, and Chorowicz (2005) states that the EARS does not exist significantly south of the Kenyan Rift, though Macheyekei *et al.* (2008) have found evidence of an ongoing deformation that has effected the N-S trending belt extending southwards from the *NTD* reaching as far as the Bahi depression in the Dodoma region. An earthquake with magnitude 5.5 struck Dodoma in November of 2002, illustrating the active tectonic deformation in this area (Macheyekei *et al.*, 2008). The Kenyan rift parts into three segments in the Arusha area (*NTD*), with two segments are running southeast towards the coast, while the third segment propagate southwards towards Dodoma (Macheyekei *et al.*, 2008).

The regional character and NE-SW trend of the major faults in the Bahi area suggest that it is an extension of the EARS that is so well expressed in the northern part of the country (Brock, 1988). Rifting was initiated in Tanzania around eight million years ago (Dawson, 2008). The first rifting stage was in the Middle to Late Miocene, when the Kenyan rift

reached the Craton margins (12-10 Ma), at which point the Western rift started to develop (Nyblade and Brazier, 2002). The second rifting stage is set to have been initiated at about 1.3-1.2 and 0.9 Ma. The oldest rift-related fault in the area of study is the NW-trending Sanzawa fault (Fig. 1.6) (Macheyeki *et al.* (2008), though the age of faulting has not been dated precisely.

Macheyeki *et al.* (2008) have completed detailed studies of the southwest trending faults that are found in the Bahi depression and adjacent areas; with the most prominent marked on Figure 1.6. The Bubu (also known as the Makutapora fault) and Hombolo Faults cut across the Sanzawa fault, partly affecting the Chenene Hills. Hot springs are found in the area where the Bubu Fault cross-cut the Chenene Hills, Macheyeki *et al.* (2008)

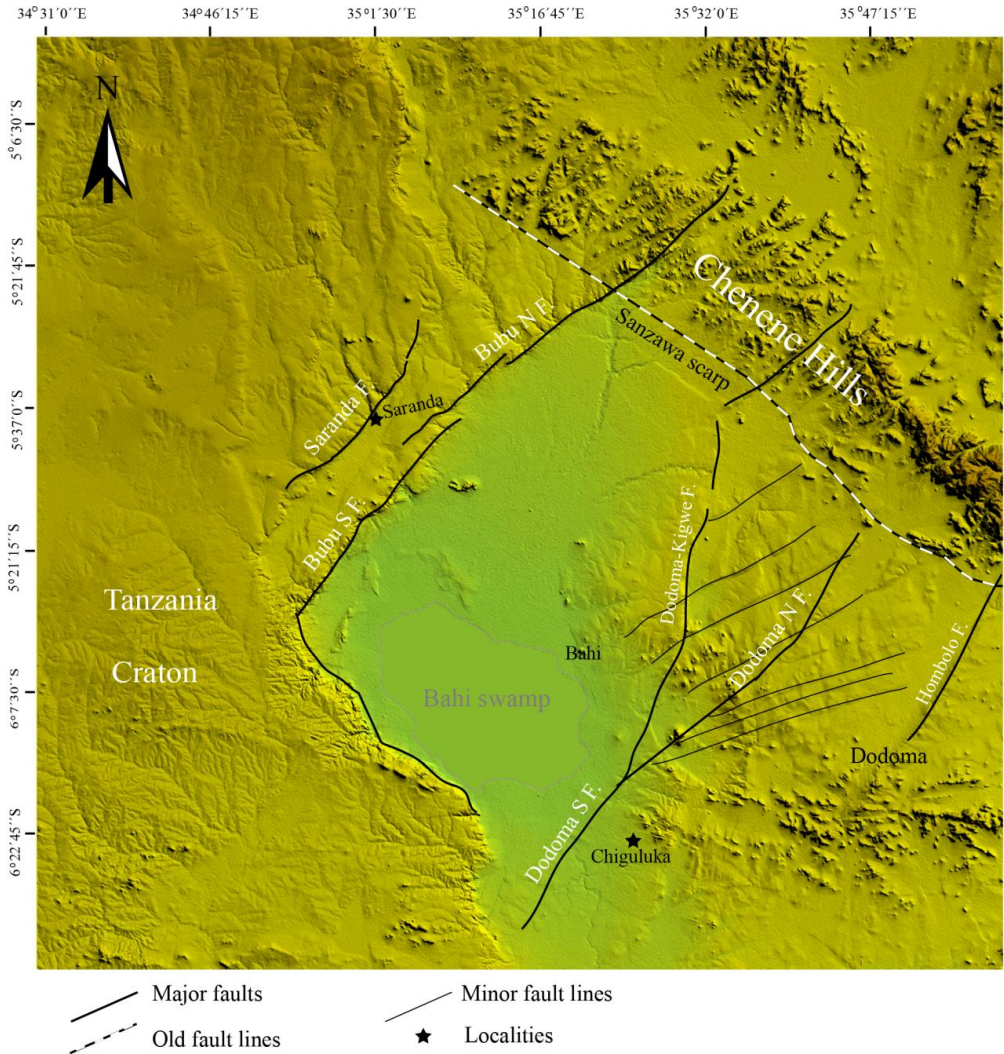


Figure 1.7 Simplified map of the study area. The most important structural features are marked on the map. The Sanzawa fault scarp separates the Bahi depression (940 m a.s.l.) from the Chenene Hills (2060 m a.s.l.), and is no longer active today. The two localities studied in this thesis are marked on the map. Information of fault lines have been collected from Macheyeke *et al.* (2008).

1.3.3 The Kilimatinde Cement

The Kilimatinde Cement is named after the village of Kilimatinde (Fig.1.8) and is the oldest sedimentary unit within the Dodoma and Singida region, lying unconformably upon the Archean rocks, and consists mainly of silicified sandstone (silcrete), but locally ferricrete and calcrete are known (Milne 1947; Fozzard 1959; Macheyeke *et al.* 2008). Where erosion has extended down to the sediment-weathered basement contact, the Kilimatinde Cement has a thickness of 15-30m, and is overlain by 75m thick layer of lacustrine sediment in the Bahi depression (Fozzard 1961; Macheyeke *et al.*, 2008).

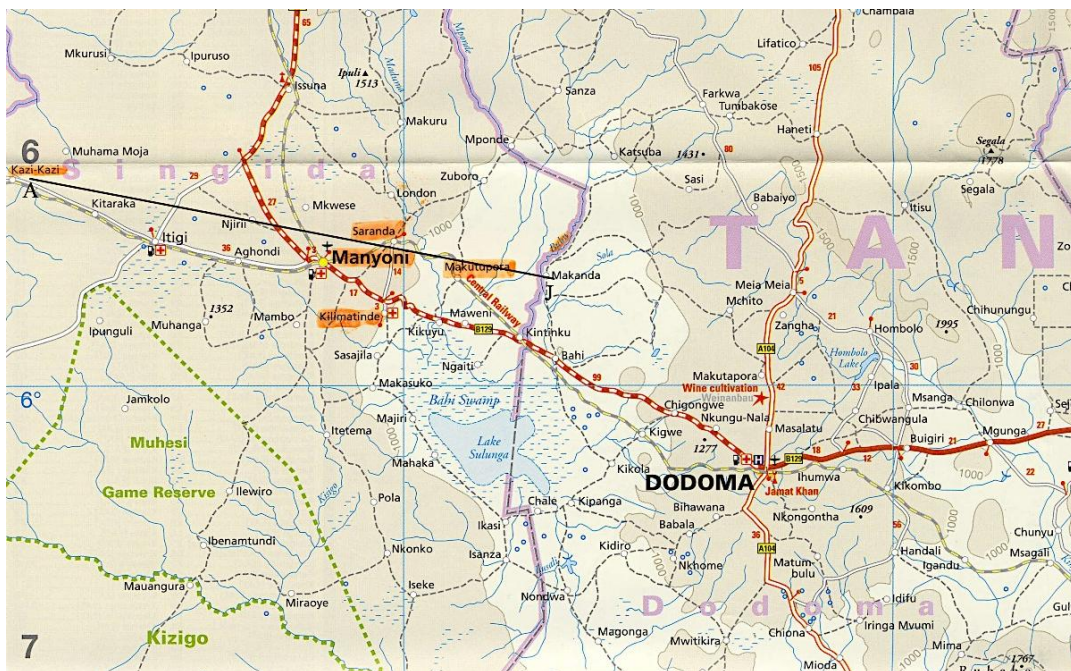


Figure 1.8 Map section of the study area in the Singida and Dodoma region. The line, A to J, h marks the area for the topographical profile (Fig.1.8). The highlighted locations are those mentioned in the same profile. From Reise Know-How, Tanzania 1:1 200 000(2011).

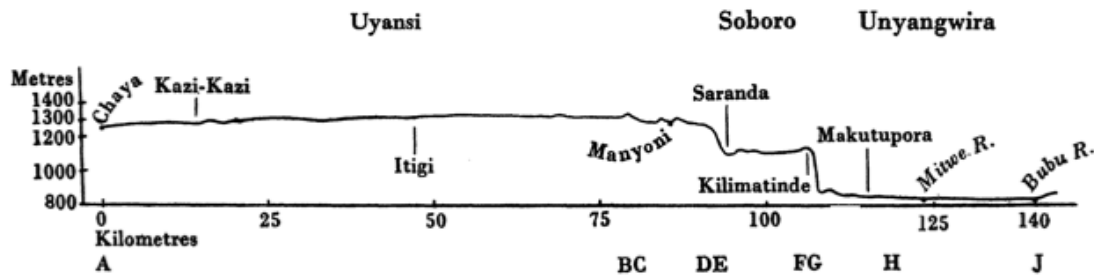


Figure 1.9 Topographical profile from Kazi-Kazi to the Bubu river. Places marked on the profile are the topographic situation and not their true projected positions (Fig. 1.8). Scale of heights 25 x scale of distance. From Milne (1947).

Milne (1947) groups the cement that overlies the granites into two parts: *conglomerates* of quartz rubbles bounded by siliceous and ferruginous cement, and *opaline rocks*, composed of quartz grains loosely bound in an amorphous opaline or partly chalcedonized/siliceous matrix.

Spence (1951) evaluated outcrops of the same surficial siliceous deposits, exposed along the Central Railway Line between Makutupora and Manyoni (Fig.1.9). He described the outcrop as pale gray to brown, consisting of quartz of variable grain sizes in a chalsedonic matrix. He also reported conglomeratic units and grain sizes up to boulder size with mixed angularity.

Fozzard (1959) believed the Kilimatinde Cement was formed in shallow evaporate basins that were developed on a quasi-planar land surface between residual hills. This view was also supported by Hugh (1961, *in* Newman, 1970), a master student from South Africa, who wrote a thesis on the cement, and concluded that the silcrete formed within shallow basins which were fed by alluvial fans and sandy rivers.

The cement has never been dated, but a possible age has been estimated e.g. by studying the faults located in the area. Fozzard (1961) points out that the Kilimatinde Cement has been subjected to tectonic stress along the Bubu and Saranda rift zones, which indicate that the formation is older than the rifting action (Fig. 1.7). He points out that the Kilimatinde Cement has not been found north of the Sanzawa fault line and concludes that the Sanzawa fault predates the Kilimatinde Cement (Fig. 1.7). Spence (1951) also remarks that the silcrettes he studied are older than the Bubu and Saranda fault scarps since the Cement has been found on both sides of the fault scarps. Additionally, veins of chalcedony have been found to cut the silcrettes at the Bubu fault scarp, and he argues that they are of the same age

as the Bubu faulting activity. Recent studies by Macheyeke *et al.* (2008) support this theory and confirm that the Kilimatinde Cement is found in the Bahi depression and to the NW of it, but its extent is limited to the NE by the Sanzawa Scarp. All faults surrounding the Bahi depression except the Sanzawa fault, have displaced the Kilimatinde deposits and are therefore related to a younger rifting stage (Fig.1.7). According to Fozzard (1961) and Macheyeke *et al.* (2008), the Chenene Hills were already hanging over the depositional area of the Kilimatinde Cement, separated by the Sanzawa fault, and was acting as the main sediment source. The most accepted age estimate is of Late Miocene to Early Pliocene (Fozzard, 1961; Macheyeke *et al.*, 2008).

There are limited publications on the Kilimatinde Cement, and not much research has been done in the recent years, therefore background information used in this thesis is primarily from the late 1940s to early 1960s.

1.4 Theoretical background

1.4.1 Silcrete

Lamplough first introduced the term silcrete in 1902. “*I have proposed the short term “silcrete” for sporadic masses in loose material of the greywether type, indurated by a siliceous cement*”. He also included the terms *calcrete* and *ferricrete* for indurated duricrusts cemented by either calcite or iron oxides, respectively.

Silcrete research has advanced considerably since the 1980s. The majority of silcretes found today has formed in arid to semi-arid environments and can be found on every continent except Antarctica (Summerfield, 1983). The most studied silcrete sites are from the Paris Basin (France), Stuart Creek opal field and the Yilgarn Craton (Australia), and the Kalahari region (southern Africa, e.g. Botswana and South Africa).

Summerfield (1983) defined silcretes as duricrusts containing more than 85 wt.% of SiO₂. They form by cementation and/or silica replacement of the rock, soil, weathering deposits, or unconsolidated sediments, by low-temperature physico-chemical processes. Silcretes occur in relatively young deposits, mostly of Tertiary age, that have never undergone burial diagenesis (Thiry 1999).

Though much research has been done on silcretes in the past decades, the process of formation is still very much debated. This is mainly due to the variety of silcretes found around the world, the number of silica sources available, and the different silicification processes in operation. Additionally, numerous classification schemes have been suggested in the past years. The classification and models of silcrete formation used in this thesis will be presented in this chapter.

Classification

Summerfield (1983) proposed a classification based upon micromorphology after investigating a variety of South African silcretes (Table 1.1). Micromorphology reflects both original host material characteristics and the effect of subsequent silica diagenesis as well as the conditions that were present during the precipitation of silica. Summerfield (1983) differentiated between four main types of fabric; grain supported (GS), floating (F), matrix (M), and conglomeratic (C).

Table 1.1 Morphological classifications of silcretes. Modeled after Summerfield (1983)

Fabric	Description	Sub-types	Remarks	Formation
Grain-supported fabric (GS)	Skeletal grains constitute a self-supporting framework	-Optically continuous quartz overgrowth -Microquartz, cryptocrystalline silica, or microquartz	Most common cements are cryptocrystalline silica or microquartz.	Passive infilling and/or replacement by silica in unconsolidated material
Floating-Fabric (F)	Skeletal grains comprise more than 5%, floating in the matrix, and do not form a self-supporting framework.	-Massive (glæbules absent) -Glæbular (glæbular present)	Most common type of silcretes. The matrix component is highly variable, and can grade into GS-fabric to M-fabric within a single thin section. Opaline silica is the main matrix component.	Displacement or partial replacement of skeletal grains or by silicification of an existing F-fabric host material. Glæbules are normally associated with pedogenic silcretes.
Matrix-Fabric (M)	Skeletal grain content is less than 5%.	As for F-fabric	Matrix consists usually consists of cryptocrystalline silica, microquartz, or opaline silica, but also clay minerals, iron oxides,	? Replacement of pre-existing F-fabric? Glæbules are normally associated with pedogenic silcretes
Conglomerate-fabric (C)	Skeletal grains include fractured bedrock, gravel, or duricrust fragments (>4mm)	...	Matrix may be of the GS-, F-, or M-fabric types	Passive infilling and/or replacement by silica in unconsolidated material

These fabric types are not mutually exclusive. Ulliyott *et al.* (2004) argued that F-fabrics may grade into GS- or M-fabric within individual units, or even in a single hand sample.

Examination of thin sections and scanning electron microscope analysis reveal that silcretes can have varying proportions of detrital minerals, silica cements, and void spaces. Small voids in the rock can be partially filled with secondary silica or other minerals, and the nature of these components not only reflects the diagenetic processes during formation, but the nature of the host material as well (Nash, 2011).

Silcrete mineralogy

Silcretes, by definition, are composed of more than 85 wt. % SiO₂, and are associated with a wide range of silica polymorphs. The mineralogy of silcretes reflects both the properties of the host rock, as well as the diagenetic conditions under which silica precipitation occurred. Opal, chalcedony, and quartz are the most common silica species found in the matrix, and can exist in a variety of forms (Summerfield, 1983; Nash and Ulliyott, 2007; Nash, 2011). The mineral sequence is determined by the solubility of each mineral phase, which, again is controlled by the purity and degree of order in the crystal structure (Williams *et al.*, 1985; Williams and Crear, 1985; Nash, 2011). Degree of order is controlled by foreign ions incorporated into the lattice, and by the degree of silica supersaturation of the solution in the system. The most disordered minerals are the most soluble, and will precipitate first (Thiry and Milliot, 1987).

Models for silcrete genesis

Summerfield (1978, 1983) suggested that silcretes could be placed into two broad groups, *weathering profile silcretes* characteristic for formations in low pH environments in more humid tropical climates, and *non-weathering silcretes* typically forming in environments with high pH. After investigation of silcretes from the Paris Basin and Southern Australia, Milnes and Thiry (1992) revealed that the environment for silcrete formation and their interrelationship is more complex than Summerfield's model. They proposed a new model of silcrete formation based on a non-environmental setting, dividing silcretes into two broad groups: (1) *pedogenic silcretes*, and (2) *groundwater silcretes*.

(1) Pedogenic silcretes

Pedogenic silcretes are directly linked to the surface and the conditions operating at the surface (Thiry, 1999), and are formed within the vadose zone by pedogenic processes (Ullyot *et al.*, 1998). Near surface processes are important factors in pedogenic silcretes and are reflected in the profile development. They form mainly in low latitude settings with alternating wet and dry seasons (Ullyott *et al.* 1998; Thiry 1999; Thiry 2009;), and provide good markers for the reconstruction of palaeosurfaces, indicating long periods of palaeolandscape stability (Thiry, 1999).

Normally, pedogenic silcretes show evidence of downwards movement of soil water. Consequently, illuviations and cappings are a common feature in this type of silcrete (Ullyott *et al.*, 1998, Nash, 2011). Furthermore, sedimentary structures in the host sediments have normally been destroyed, and are absent, or rare in most pedogenic silcretes (Milnes and Thiry, 1992; Ullyott *et al.*, 1998; Thiry, 1999; Nash, 2011).

(2) Groundwater silcretes

Groundwater silcretes can develop in both weathered and non-weathered materials, and are most commonly found as discontinuous lenses or sheets (Ullyott *et al.*, 1998). Silicification is normally related to the water table or groundwater flow within the sediments, and groundwater level is the main factor that controls the genesis (Thiry, 1992). Ultimately, forming in a wide range of climatic and pH conditions under phreatic conditions, at the water table, or near groundwater outflow zones (Ullyott, 2007),. The groundwater silcretes usually develop between depths of 5 and 50-100 m (Thiry, 1999), and are less dependent upon climate, though topography has been thought to be of great importance (Nash and Ullyott, 2007).

Primary sedimentary structures are usually well preserved and various silica polymorphs can be present (Ullyott *et al.*, 1998; Thiry, 1999; Nash, 2011), while illuvitaion structures are less common or absent (Thiry, 1992; Ullyott *et al.*, 1998; Ullyott, 2007)

Silica sources and transport

Silica can be derived locally from within the host rock, or be transported by wind as dust, or in dissolution by water from distal sites. The most important source of silica associated with silcretes is products of chemical weathering of silicate minerals (Summerfield, 1983; Ulllyott *et al.*, 1998; Nash, 2011).

Silica in solution will be transported by water, either through lateral and/or vertical movement, or a combination of the two (Summerfield 1983).

1.4.2 Silica polymorphs

Opaline silica

Opal is a naturally hydrated silica mineral with the chemical formula $\text{SiO}_2 \cdot n\text{H}_2\text{O}$. Opal is a common silica polymorph in nature, associated with sedimentary environments. Many organisms (e.g. diatoms) precipitate opal-A to form siliceous tests, which can accumulate in sediments after the organisms death (Williams *et al.*, 1985; Smith, 1997) Opal is also associated with inorganic precipitation, such as groundwater leaching of silica from siliceous rocks and soils, and hot springs (Smith, 1997).

Jones & Segnit (1971) proposed a three-fold classification of these hydrous silica species based on crystal stability: opal-A, opal-CT, and opal-C

1. Opal-C

well-ordered α -cristobalite

2. Opal-CT

disordered α -cristobalite,

α -tridymite

3. Opal-A

highly disordered, near amorphous

A comparison of the crystal structure of quartz and cristobalite is given in Figure 1.10. In cristobalite, the six-membered oxygen ring is almost planar, while it appears more irregular in quartz. Opal-CT and opal-C differ from opal-A since they have domains of short-range ordered structures which mimic intergrowths of cristobalite and tridymite, Smith (1998).

All opal species lack sufficient crystal order to be considered crystalline, even opal-C, which is the polymorph with the highest order, but contains between 3 to 8% water in the structural make-up (Smith, 1998).

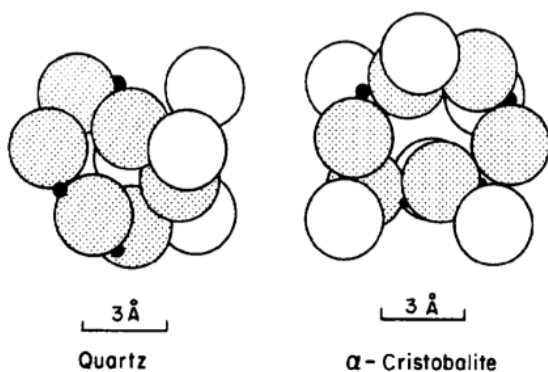


Figure 1.10 Crystal structures of quartz and α -cristobalite. In quartz, six-membered oxygen rings are projected onto (1100). Six-membered oxygen rings projected onto (111) of a pseudo-cubic cell in α -cristobalite. From Jones and Segnit (1972).

Elzea *et al.* (1994) states that x-ray diffraction based identification are the only way for true identification since the various opaline silica species have similar physical properties and are mainly chemically indistinguishable.

Opal-A

Silica can precipitate from natural aqueous solutions as amorphous silica (opal-A) in a number of low-temperature environments (Williams *et al.*, 1985). This low temperature amorphous variant can either be precipitated organically by organisms such as diatoms in the form of skeletal material, or inorganically from silica saturated solutions (Williams *et al.*, 1985a; Elzea *et al.*, 1994). Opal-A will then be precipitated when the solution becomes supersaturated with respect to silica, which causes silicic acid polymers to precipitate (Eleza *et al.*, 1994). Opal-A can be subdivided into opal-A_G and opal-A_N depending on whether the silica linkage is more gel-like (G), or network-like (N) (Smith, 1997b).

Opal-CT

Opal-CT consists of disordered α -cristobalite with tridymitic stacking, and often occur as spherical aggregates of platy cristobalite crystallites, known as lepispheres (Gaillou, 2008). Opal-CT has arrangements of silica based on six-membered rings, which resemble the arrangement of atoms in cristobalite and tridymite (Smith, 1998). Opal-CT can be found in a variety of forms and structures on the microscale, such as random aggregation of individual grains, nanograins arranged in fibers, nanograins arranged in platelets, and in lepispheres. Lepispheres can further be subdivided into two types: *well-bladed* and *poorly bladed* (Flörke *et al.*, 1976). The variety of the different structures can be a response to different precipitation rates, and Gaillou *et al.* (2008) proposed that random piling of individual nanograins are the result of rapid growth rates where the individual grains do not have the time to arrange themselves into a larger structure. Gaillou *et al.* (2008) also suggest that lepisphere formation may be a result of a slower growth rate. Platelets are suggested to be the intermediate structure. The cauliflower-like opal-CT structures have been referred to as *composite lepispheres* by Flörke *et al.* (1976). They argue that composite lepispheres form when the entire pore space has been filled with tightly packed microspheres, that have grown together to form coalescent lepispheres.

Opal-C

In the opal-CT, the proportion of cristobalite is much greater than that of tridymite, and differs from opal-CT by its higher stacking order, though it is still addressed to as a paracrystalline (Smith, 1998).

Silica solubility

At 25 °C the solubility of quartz is 6-10 ppm; cristobalite is 20-30; amorphous silica is 60-130 ppm, and the aqueous solubility of silica parallels the diagenetic sequence above (Williams *et al.* 1985).

Diagenetic transformations

According to Williams *et al.* (1985), the diagenetic transformations follow a dissolution-precipitation pathway, which is controlled by aqueous solubility of the phases, which is primarily a function of crystal structure, and particle size and shape.

The generalized silica diagenetic sequence is as follows:

Opal-A → opal-CT → better ordered opal-CT →
cryptocrystalline quartz or chalcedony → microcrystalline quartz.

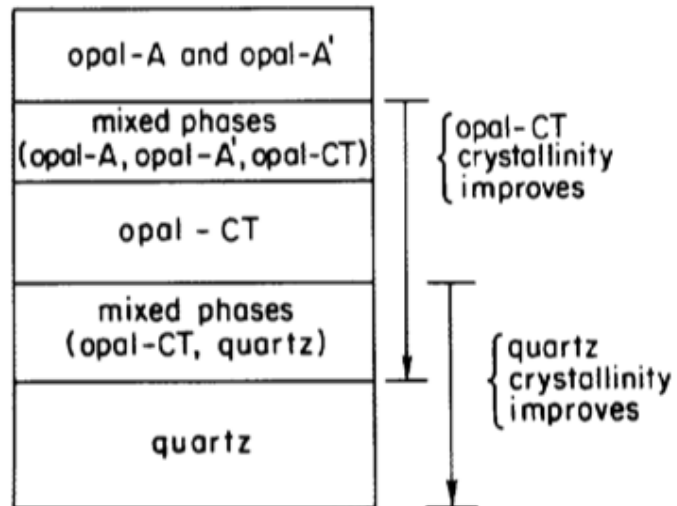


Figure 1.11 Schematic diagram for diagenetic transformation of opal in a sedimentary stratigraphical column. Crystal stability improves with time and burial depth. From Williams et al. (1985)

2 Methods and material

2.1. Fieldwork

Fieldwork and sedimentological sampling in the Bahi area was first carried out for three weeks in December of 2010 by Professor Henning Dypvik (UiO) and Dr. Charles Kayaa (UDSM). They visited several localities where sampling and logging were performed. The samples were brought back to UiO where the writer prepared samples for XRD, thin sections and trace element analysis.

Based on the geochemical analysis, sections of interest were chosen to form the base of additional fieldwork for the following year. The author spent eight days in the field in late October to early November of 2011. The localities visited included Chiguluka and Saranda, with locality reference “CHIG”, and “SARP”, respectively. The locality reference is used when naming samples followed by the sample number and year of collection. Both sections were logged using a standard logging sheet in the scale of 1:20. During logging, the author worked on the logged sections from 2010, and samples were collected from the same units but more closely spaced. The two sections (CHIG and SARP) were re-logged and samples collected in 2011 were intergraded with the log samples collected in 2010. Thus, all logs presented in this thesis display levels of sampling from both field seasons.

A hand-held NaI (Tl) scintillation detector (Canberra SG-2P Radiagem 2000) was used to measure natural gamma radiation at both locations. The instrument measures natural gamma radiation emitted from K, Th, and U (Canberra Industries Inc., 2010). Radiation is given in counts per second (cps). At both localities, radiation was measured from the base to the top of each profile, and samples were collected in all layers. Measured variations in radiation within a single layer can be high. In those cases an average measured radiation was used.

The instrument turned out to be sensitive to heat, and consequently during the last day at the SARP-location it broke down. The plan was to measure the gamma-trend in the profile by taking measurements at every meter. This plan failed, but the radiation collected in every sample was registered.

PhD Student Lars Riber and Professor Arild Andresen assisted the author in the field, and Dr. Charles Kayaa was very helpful with localizing the sections visited during the field season in 2010.

2.2 Facies and facies associations

Field observations and thin section analysis were used to define a sedimentary facies on the basis of sedimentary structures, texture, and bedding characteristics. The facies is the sum of total features that reflect the specific environmental conditions under which the given rock was deposited. Folk's classification (1954) of sedimentary rocks based on sand, clay, and mud content, Figure 2.1, have been used in this thesis. The Wentworth grain-size scale was used to determine grain size, Table 2.1.

The facies that are genetically related to one another, reflecting a specific sedimentary environment, are grouped together in facies associations.

Table 2.1 The Wentworth (1922) grain size scale for sediments, with equivalent with phi units and grain size in mm.

Wentworth size class	Phi (ϕ) units	Millimeters
Boulder.....	- 8	>256 mm
Cobble.....	- 6	64-256 mm
Pebble	- 4	4-64 mm
Granule.....	- 2	2-4 mm
Very coarse sand.....	- 1.....	1-2 mm
Coarse sand.....	0	0.5-1 mm
Medium sand.....	1.....	0.25-0.5 mm
Fine sand.....	2.....	0.125-0.25 mm
Very fine sand	3.....	0.063-0.125 mm
Silt	4.....	0.004-0.063
Clay.....	8.....	<0.004 mm

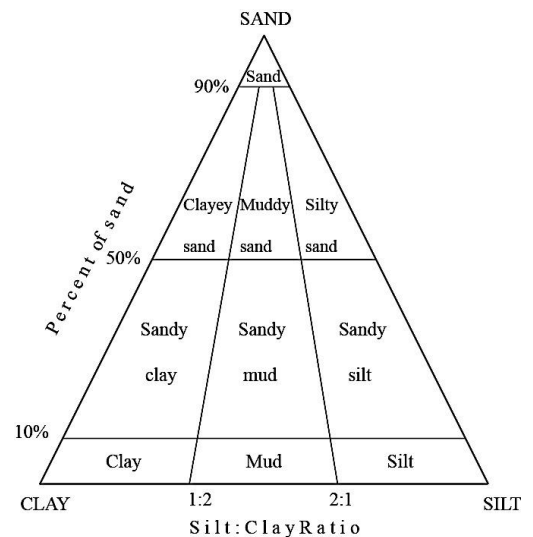


Figure 2.1 Terminology of sedimentary rocks lacking gravel, based upon the percentage of sand, and the silt to clay ratio. From Folk (1954).

2.3 Petrographical and mineralogical analysis

A diamond saw was used to cut the samples into three pieces; one small piece for thin sections, and one small piece to be grinded up. The remaining piece was placed at the Department of Geosciences storage room for future work. The samples were ground into rock powder by a slinging mill that was carefully cleaned with ethanol between samples. The rock powder was used in XRD- and geochemical analysis. The author carried out all the preparation work at the Department of Geosciences, UiO.

2.3.1 Thin sections

A total of 79 rock samples were sent to PETRO-Sec at Institute of Energy Technology (Institutt for energiteknikk, IFE), Oslo, where thin sections were produced. The rock samples were impregnated in blue epoxy and glued to 2.5 cm x 4.5 cm glass slides, then polished down to a thickness of about 30 μm .

2.3.2 Point counting and rock characteristics

Forty-nine thin sections were studied in detail under a petrographic microscope in order to give information about mineral composition and rock texture. When working with the microscope, the following features were noted: minerals present, lithology, sorting, whole rock grain size, the average of the ten largest grains, porosity, permeability, roundness, grain supported vs. matrix supported, preservation of grains (especially feldspars), grain contacts, cementation, secondary precipitation features, and primary and secondary structures (Appendix A)

The degree of sorting was determined by using Compton's classification scheme (1962), (Fig. 2.2), and rounding was determined by Powers' (1953) terminology for degree of rounding (Fig. 2.3). Terry and Chilingar's (1955) guide for visual estimation of porosity was used to determine porosity in each thin section, (Fig. 2.4)

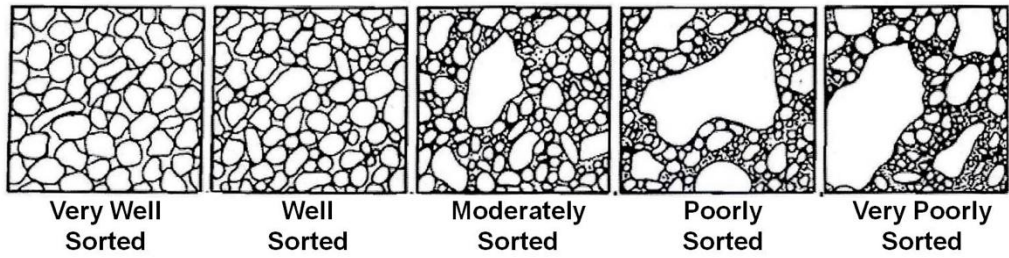


Figure 2.2 Classification of degree of sorting, (Compton, 1962).

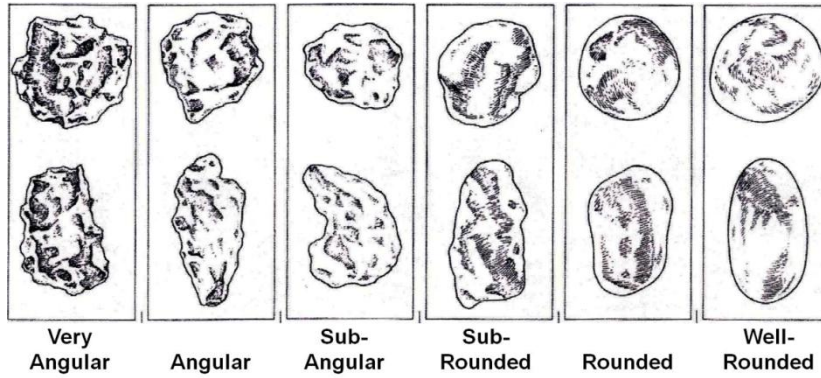


Figure 2.3 Terminology of degree of rounding of detrital grains, (Powers, 1953).

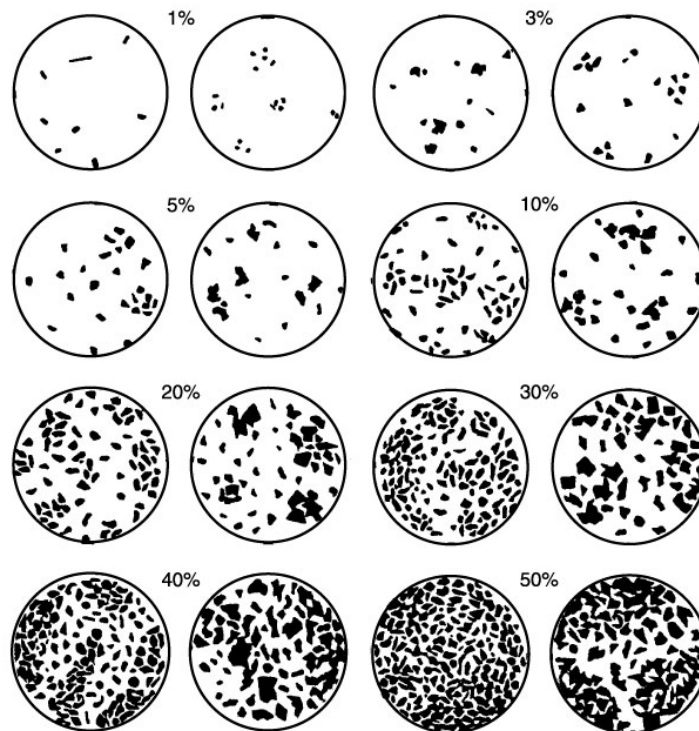
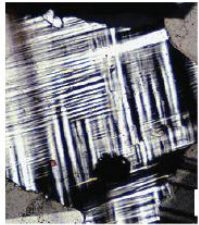
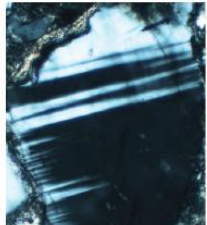

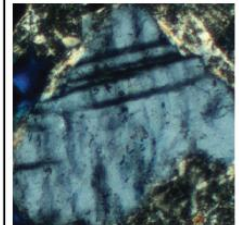
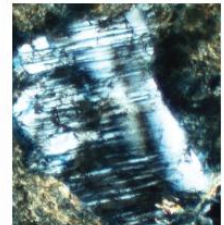


Figure 2.4 Comparison chart for visual estimation of percentage, (Terry and Chilingar, 1955).

Identified feldspar grains were placed in one of five categories (Table 2.2), each category representing a specific preservation of feldspar, with category one being “fresh” with perfect preservation, and five, indicating the lowest preservation of the grain, as barely recognizable as feldspar.

Point counting was performed on 43 thin sections (Appendix B). Four-hundred points were counted by using a Swift point counter installed on a standard petrographic microscope. Quartz grains were divided into monocrystalline and polycrystalline grains. The extinction angles of quartz grains were also noted. Extinction angles above 5 degrees were noted as undulatory extinction. Feldspar grains were divided into plagioclase and potassic feldspar, along with the degree of preservation (Table 2.2). Other visible characteristics counted are as follows: rock fragments, heavy minerals, opaque and isotropic grains, chalcedony, iron oxide staining, illuviation structures, cement, and pores in the thin section. The cement and matrix within many thin sections are hard to distinguish. Points counted as cement could therefore be both matrix and/or cement.

Table 2.2 *Preservation of feldspars.*

Category	1	2	3	4	5
Description	Fresh, has not been subjected to weathering	Show some evidence of weathering, but twins are almost fully preserved	Intermediate. Twins start to look blurry and grain surfaces show roughness	Very rough surface. Twinning might be hard to recognize	Twins are absent or barely identified. Hard to identify plagioclase from microcline. Grain surfaces show extensive dissolution and has extreme rough surface.
Example					

2.3.3 X-ray diffraction analysis (XRD)

XRD-analysis is a useful tool for mineralogical analysis. It is in particular applicable when studying the clay fraction, since the clay is often too small for microscopic analysis. XRD-analysis was carried out at the Department of Chemistry and the Department of Geosciences at UiO. Table 2.3 shows which samples were carried out in each department, respectively.

XRD Machine Specifications: D8 advance diffractometer, 40 kV and 40 mA, variable divergence slit, sample length 15 mm, no monochromator, Ni K-beta filter, Lynxeye linear PSD detector, 2,3 degrees soller slits (primary and secondary), scatter screen and sample rotation at 30 RPM.

Table 2.3 Table displaying which samples that were analyzed at which Department.

Each rock sample was crushed to rock powder. Each mineral has a characteristic unit cell and crystal lattice. When irradiated with x-ray beams each mineral will produce a specific *d*-value and 2θ angles of diffraction pattern, a function of the unit cell (Moore and Reynolds, 1997). The *d*-spacing, intensities and the 2θ angle of a substance from the XRD-diagram can then be compared with the

Department of Chemistry		Department of Geology	
SARP 1-11	CHIG I 2-11	SARP BASE I-11	SARP 10-10
SARP 2-11	CHIG I 3-11	SARP BASE II-11	SARP 11-11
SARP 3-11	CHIG I 4-11	SARP 1-10	SARP 12-10
SARP 4-11	CHIG I 6-11	SARP 2-10	SARP 13-10
SARP 5-11	CHIG II 1-11	SARP 3-10	SARP 14-10
SARP 6-11	CHIG II 2-11	SARP 4-10	SARP 15-10
SARP 7-11	CHIG II 5-11	SARP 5-10	SARP 16-10
SARP 8-11	CHIG II 6-11	SARP 6-10	SARP 8-11
SARP 9-11	CHIG II 7-11	SARP 7-10	SARP 10-11
SARP 11-11		SARP 8-10	CHIG I 1-11
		SARP 9-10	CHIG II 3-11

JCPDS (Joint Committee for Powder Diffraction Standards) catalogue for mineral identified.

In this thesis, the author used the MacDiff software for peak interpretation (Petschick, 2011). The mineral content in each sample has been semi-quantified. Semi-quantification is based on the intensity of the strongest reflection of the mineral of interest. Some minerals have their main reflection in the same position as many other minerals (e.g. quartz), and the second largest peak is than used. It is important to keep in mind that these are not true percentages, only estimations; the results are therefore presented as XRD percentages in this thesis (Appendix C). It is also worthy to keep in mind that for the minerals where the second largest peaks have been used, the XRD% is most likely higher than what is presented here.

Mineral identification

A common peak for several minerals has a d -spacing of 3.34 Å, and can therefore not be used. For more accurate identification, the second largest peak is used instead, e.g. quartz. For orthoclase, the peak with the highest intensity is too close to the 3.34 Å peak, and therefore the second largest peak is used instead. Table 2.4 displays the peaks used.

Table 2.4 The peak value in Å for minerals of interests.

* = the second most intense peak after 3.34Å.

Mineral	d -value (Å)	Mineral	d -value (Å)
Quartz	*4.26	Dolomite	2.88 - 2.90
Opal	4.1	Kaolinite	7.17
Microcline	3.24	Saponite	4.48
Plagioclase	3.18	Illite	10?
Orthoclase	*3.77	Montmorillonite	15?
Calcite	3.03	Apatite	2.8

Identification of hydrous silica polymorphs in XRD

Opal-A, opal-CT and opal-C can be identified by their diffraction patterns. Opaline silica produce broad reflections with low intensity on an XRD recording, which makes them more difficult to interpret (Eleza *et al.* 1996). The literature on the subject lists several characteristic d spacings for the different opal species. In this thesis the diagnostic peak positions found in Ghisoli *et al.* (2010) will be used (Table 2.5).

Opals are differentiated primarily by their d -value and their main reflections. The most common reflections used in practice of classification are listed in Table 2.5 below.

Table 2.5 Identification of opal-A, opal-CT, and opal-C in XRD recordings, based on d -values of their most important reflections. Peak information collected from Ghisoli *et al.* (2010)

	Main peak (Å)	Main peak Characteristics	Secondary Peak (Å)	Tridymitic Shoulder (Å)	Other diagnostic Peaks (Å)
Opal-A	4.1	Very broad and diffuse reflection	X	X	X
Opal-CT	4.06-4.11	Broad, less intense reflection	2.5	4.3	X
Opal-C	4.02-4.05	Sharp, intense reflection	2.5	4.3	3.13 and 2.84

In opal-CT, the main peak is situated at about 21.80 2°θ, and the recording is a result of α-tridymite (4.107 Å) and α-cristobalite (4.04 Å) stacking in the crystal. A higher crystal disorder will produce higher d values and visa versa. The secondary peak, situated at about

36.05 $2^\circ\theta$ is recorded together with the main peak. This reflection is also due to stacking of *hkl* α - tridymite and α - cristobalite. A peak situated at the low angle side of the main peak is often associated with opal-CT. This peak can only be detected in opals that have a quite orderly structure since the background camouflages the recording as the crystallographic disorder increases.

Opal-C is identified by the presence of two other peaks, 3.13 and 2.84 Å. These two peaks are only found in this polymorph and are reflections of α - cristobalite. The tridymitic shoulder, common in many opal-CT, is also often associated with opal-C.

The degree of ordering in these silica polymorphs can be determined by dividing the peak width at half height by the peak position (FWHM / $d(1\ 0\ 1)$ Å), Eleza *et al.* (1994).

2.3.4 Scanning Electron Microscope (SEM)

An SEM was used to identify minerals, study the preservation of individual grains, detect for authigenic minerals, and search for uranium bearing minerals. Both gold-coated stubs and carbon coated thin sections were investigated.

SEM analyses were executed at the Department of Geoscience, UiO, with a JEOL-JSM-6460LV scanning electron microscope, by the author under the supervision of Berit Løken Berg.

Secondary electron image (SEI) was used on stubs, while backscatter electron image (BEI) were used on thin sections.

2.3.5 Electron microprobe (EMP)

Electron microprobe (EMP) analysis was performed using a Cameca SX100 instrument fitted with 5 wavelength-dispersive spectrometers. The electron microprobe was used to study the matrix composition and for quantitative analysis of garnet, illmenite and spinel grains. The microprobe was also used in the search of uranium-bearing minerals.

The electron microprobe analyses were performed at the Department of Geoscience, UiO, with assistance from Muriel Marie Laure Erambert.

2.4 Trace element geochemistry

Crushed rock samples were sent to Activation Laboratories Ltd., Ancaster, Ontario, Canada, for trace element geochemical analysis. Fused samples from both field seasons were diluted and analyzed on a Perkin Elmer Sciex ELAN 6000, 6100 or 9000 ICP/MS. Two different analytical packages were used on the 2010 and 2011 samples. For the 2010 samples, the Ultratrace-7, (UT-7), Peroxide Fusion ICP & ICP/MS package was used, and the Ultratrace-6, (UT-6), Total Digestion ICP & ICP/MS was chosen for the 2011 samples. Results are given in parts per million (ppm) (Appendix 5).

The UT-6 Total Digestion ICP & ICP/MS package combines a 4-acid digestion (HF, HClO₄, HNO₃ and HCl) with analysis by ICP and ICP/MS. Resistate minerals are not digested. For the ICP portion, a 0.25 g aliquot of sample is digested with HF and then HClO₄-HNO₃ at 260°C to fuming and is diluted with dilute aqua regia. This leaching process is specifically designed for magnetite, chromite, barite, spinels, zircon and massive sulphides. The solutions are read on a Varian 735ES ICP. The ICP/MS portion determines the additional elements on the multi-acid digest solution. One blank is run for every 40 samples. In-house control is run every 20 samples. Digested standards are run for every 80 samples. After every 15 samples, a digestion duplicate is analyzed. The instrument is recalibrated every 80 samples.

The UT-7 Sodium Peroxide fusion ICP & ICP/MS package combines a Sodium Peroxide Fusion with ICP and ICP/MS. All metals are solubilized. The fused blank is run in triplicate for every 22 samples. Controls and standards fused with samples are run after 22 samples. Fused duplicates are run for every 10 samples, and the instrument is recalibrated for every 44 samples.

The analytical package used on the 2010 samples has higher detection limits than the analytical package used for the 2011 samples, e.g. 5 ppm for vanadium contra 1 ppm in 2011 samples. The fact that two different methods have been used in this analysis therefore has some misleading results. Detection limits for the different elements in UT-7 and UT-6 is given in Appendix D.

The correlation coefficient was calculated for selected elements to study element-element and element-mineral associations.

- Positive correlation if value is equal or larger than + 0.7
- Negative correlation if value is equal or smaller than - 0.7

The correlation coefficients were calculated by using Excel analysis toolbox. Values for rare earth elements (REE) were added to this analysis.

Th/U ratios and distribution of nickel and chromium

The ratio between thorium and uranium was calculated. This ratio together with the distribution of nickel and chromium has been used as an indicator for oxygen availability Dypvik et al. (2006). Low Th/U and high concentrations of Ni and Cr can be used as a signal for reducing/anoxic conditions. High Th/U together with low Ni and Cr values can indicate oxidized conditions.

3 Results

3.1 Facies description and facies associations

The SARP locality (Fig.1.6) is situated at an elevation of 1107 – 1136 m and is located not far from the village of Saranda, at latitude S 05°39, 163 and longitude E 35°00, 194.

Outcrops are exposed along the main roadside and the formation thickness is 24.6 m from base to top. The section was logged in the scale of 1:20 and the measured gamma radiation was noted in the logs. The log is displayed in Figure 3.2, and field measurements of natural gamma radiation can be found in Appendix 6.

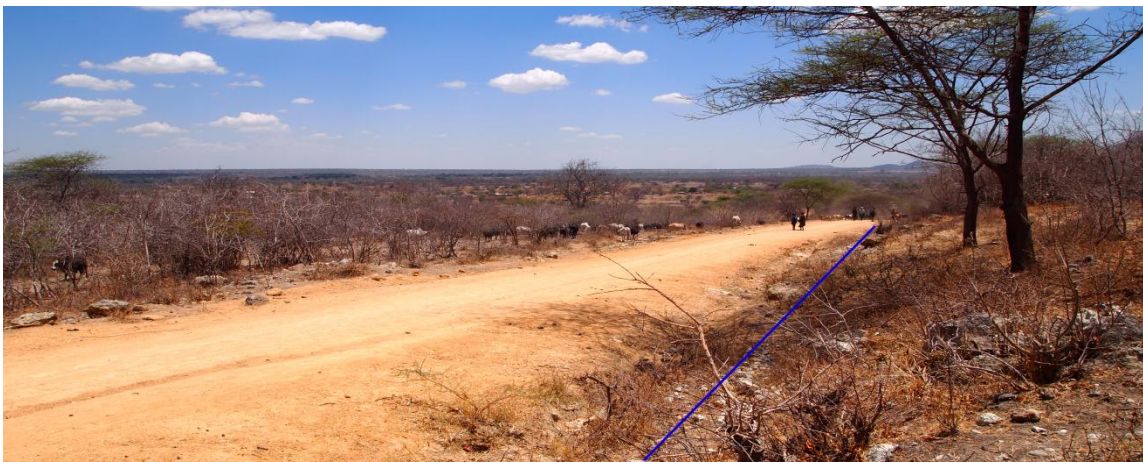


Figure 3.1 This photo shows the lowest part of the Saranda locality. The blue line marks the first few meters of the logged section.

The SARP profile consists mainly of silicified horizontally stratified silt- and sandstones. The sedimentary succession is located unconformably above weathered Archean granite. Seven different facies, and three facies associations have been identified in the Saranda profile, Table 3.1.

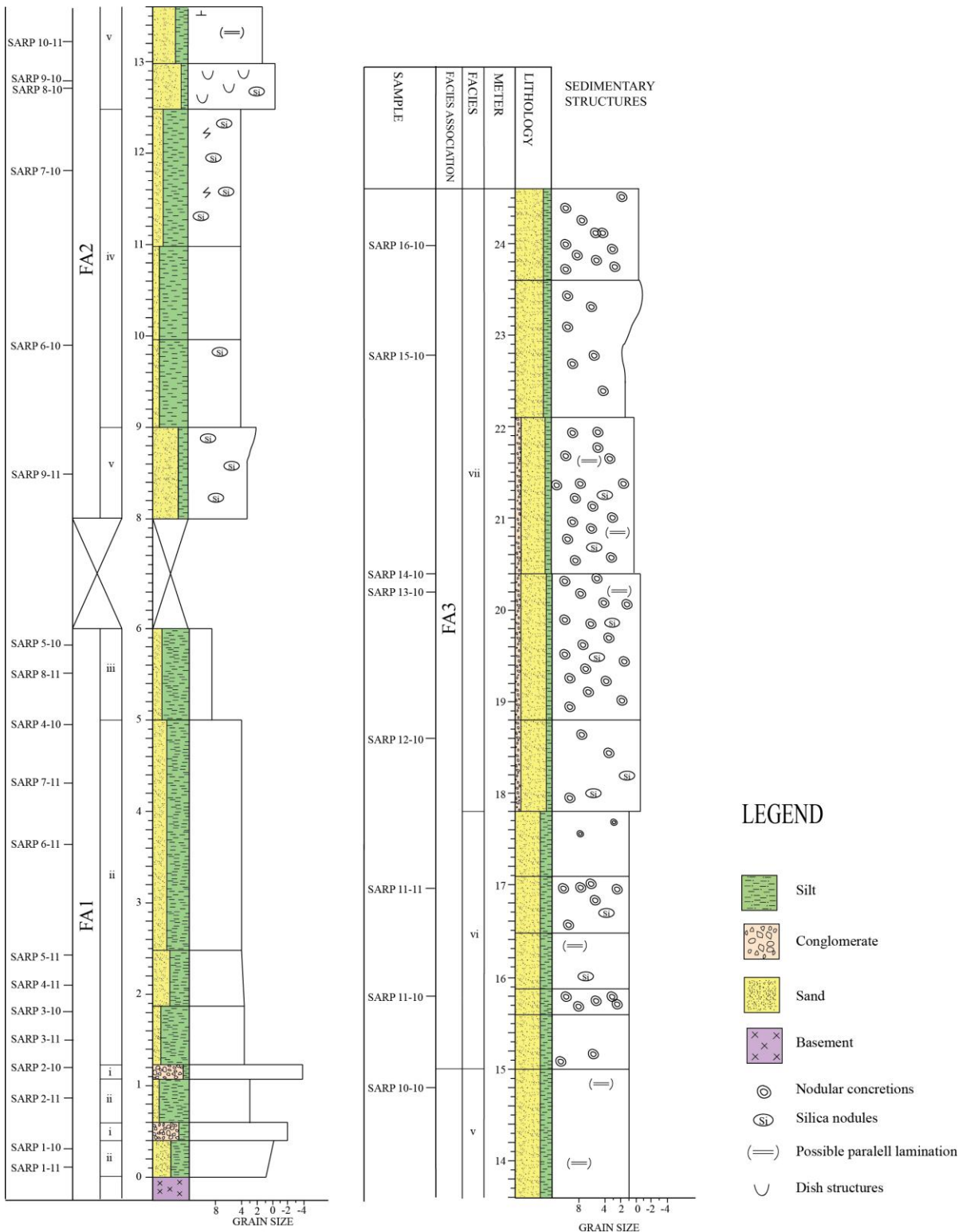


Figure 3.2 Sedimentological log, SARP.

3.1.1 Facies description

Table 3.1 Sedimentary facies in the SARP-profile

Facies nr.	Facies	Grain size	Physical appearance	Samples
<i>i</i>	Matrix supported conglomerate	Granule to pebble	Angular grains (qtz., heavy minerals) floating in a very fine matrix	2-10
<i>ii</i>	Greenish gray siliceous sandy siltstone	Silt to very fine sand	Angular millimeter sized quartz grains floating in a green matrix. Sedimentary structures absent.	1-10, 2-11, 3-11, 3-10, 4-11, 5-11, 6-11, 7-11, 4-10
<i>iii</i>	Greenish gray siliceous claystone	Clay to silt	Few detrital grains, freely floating in a pale green matrix. Heavily silicified with white silica bands and small geodes with opal.	8-11, 5-10
<i>iv</i>	Siliceous sandy siltstone	Silt to very fine sand	Structureless, poorly sorted, angular to sub-angular grains. Well silicified. Silica veins and nodules present in large numbers. Light gray colour.	6-10, 7-10
<i>v</i>	Siliceous silty sandstone	Fine to medium sand	Structureless, poorly sorted, angular to sub-angular grains. Well silicified. Light gray colour.	9-11, 8-10, 9-10, 10-11, 10-10
<i>vi</i>	Nodular silty sandstone	Medium sand	Concentric nodules, typically with iron staining, in a light gray matrix. Nodules range in size from 0.5 - 2 cm. Angular to sub-rounded quartz grains. Possibly horizontally bedded.	11-10, 11-11
<i>vii</i>	Nodular sandstone	Very coarse to coarse sand	Similar to <i>vi</i> , but nodules are larger and less rounded. Iron oxide staining, angular to sub-angular grains. Possibly horizontally bedded.	12-10, 13-10, 14-10, 15-10, 16-10

- i. Matrix supported conglomerate:** this facies is present in two units in the lowermost part of the section (Fig. 3.2). Each layer is approx. 20 cm thick. The grains do not show any preferred orientation or grading, and no sedimentary structures are identified. Grains vary in size, shape and composition (Fig.3.3a) Identified grains include: granitic rock fragments, quartz, red garnets, and small black to dark red grains. The granitic grains tend to be sub-rounded, quartz grains are angular to sub-rounded, and the small black grains are usually no more than one to two millimeter in size and are very angular. The conglomerate is matrix supported with individual grains floating freely in a very fine, pale green

matrix. The rocks are well cemented by silica. Natural gamma radiation from these units are approximately 300 cps (Appendix 6).

ii. Greenish gray siliceous sandy siltstone: the most common lithofacies in the lower part of the profile (Figs.3.2, 3.3d). It is characterized by a lack of sedimentary structures, poor sorting, and angular to sub angular quartz grains which float in a pale greenish gray matrix. Silicified white bands are widespread for all rocks of this facies. These rocks are well-cemented by silica, and are very dense and hard to break. The rocks belonging to this facies are the most radioactive, from 300 to 1200 cps (Appendix 6)

iii. Greenish gray siliceous sandy claystone: found in a one meter layer from five to six meters above the basement (Figs.3.2, 3.3b,c). Colour varies from dark to pale green. Sedimentary structures are absent.

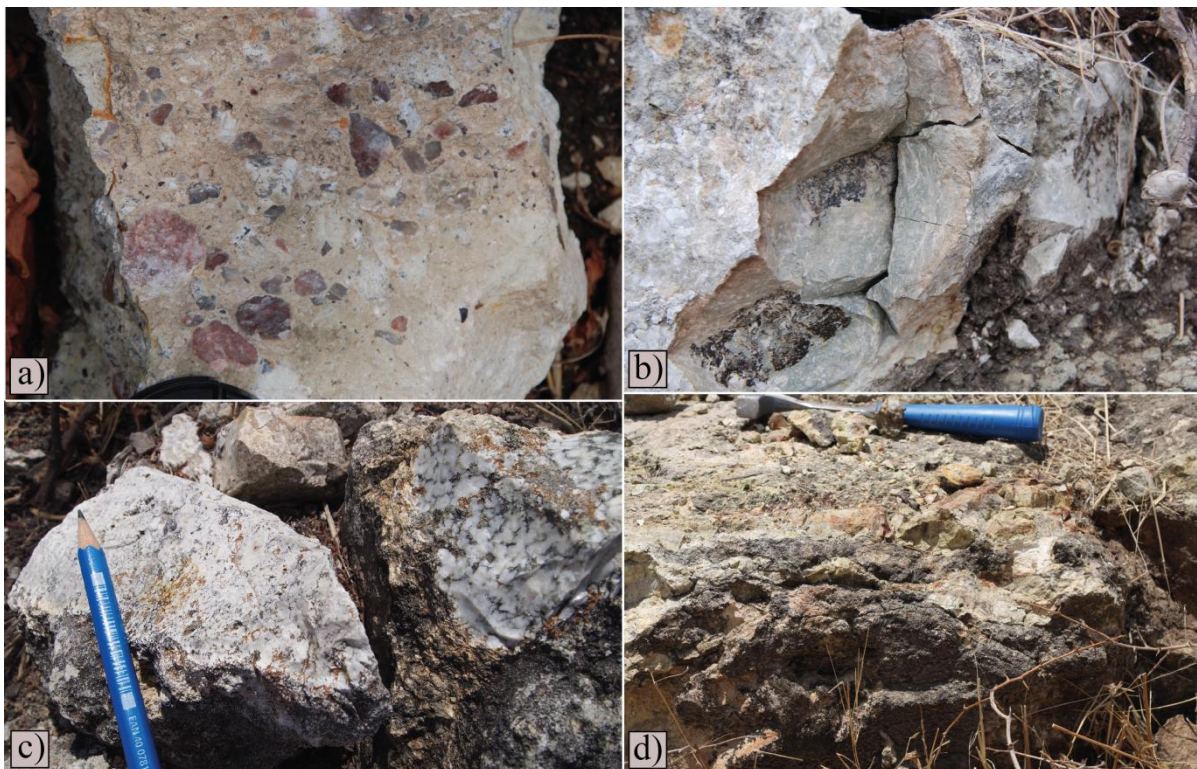


Figure 3.3 a) The conglomeratic facies (i), from which SARP 2-10 has been collected. The matrix-supported conglomerate contains angular to rounded grains of various species, mostly quartz. Examples of the greenish gray siliceous claystone facies (iii) are displayed in

photos b) SARP 5-10, and c) SARP 8-11. d) Example from the sample SARP 5-11, the highly radioactive unit within the greenish gray siliceous sandy siltstone facies (ii).

- iv. **Siliceous sandy siltstone:** this facies is found between 9-12.5 meters above the basement (Fig. 3.2). It has a light brownish gray colour and sedimentary structures are absent, but possible bioturbation tracks have been noted in one layer of this facies. White silica nodules and veins are numerous and widespread in rocks belonging to this facies (Fig. 3.4 d,e). Quartz grains are angular to sub-angular. Red iron oxide staining are scattered, but normally associated with silica veins. Natural gamma radiation varies from 150 to 200 cps (Appendix E).

- v. **Massive siliceous silty sandstone:** is similar to facies *iv* in appearance but coarser. Located between 8-9 m, and 12.4 -15 m above the basement (Fig.3.2). The concentration of grains is somewhat denser but still matrix supported (Fig.3.4a, b, c). Silicification is not as pronounced as in facies *iv*. Possible dish structures and weak indications of horizontal bedding are seen in the uppermost unit of this facies. Natural gamma radiation is measured to be 150 to 200 cps (Appendix E).

- vi. **Nodular silty sandstone:** Situated between 15-17.8 m above the basement (Fig.3.2) and is a medium massive sand, characterized by concentric nodules of unknown origin (Fig.3.5). The round nodules are framed by white, possibly siliceous, rims. Small quartz grains, no larger than one millimeter, are scattered around in the matrix, but clast concentration is somewhat higher within the nodules. The rocks belonging to this facies have a dark gray weathered surface. They appear to be slightly horizontally bedded in some places, but the structures are not very distinct. The gamma radiation was measured at 150 to 160 cps (Appendix E).

- vii. **Nodular sandstone:** situated between 17.8 -24.5 m above the basement (Fig.3.2). Similar to facies *vi*, but coarser grained, nodules appear larger and less rounded (Fig. 3.5). Staining by red iron oxide is common in this facies. Quartz grains are

angular to sub-angular and in higher concentration within the nodules. This facies has weak indications of possible horizontal bedding at some levels, but these structures are not very distinct. Natural gamma radiation is 140 cps. except for one unit, which has a higher radiation of 220 cps. (Appendix E).

3.1.2 Facies associations

(1) FA1: Greenish gray siltstone association: (0 -5 m)

- *Matrix-supported conglomerate (i), green siliceous sandy siltstone (ii), green siliceous sandy claystone (iii)*
- *(Figs. 3.2, 3.3)*

(2) FA2: Silicified sandstone association: (8-15 m)

- *Siliceous sandy siltstone (iv), massive siliceous silty sandstone (v)*
- *(Figs. 3.2, 3.4)*

(3) FA3: Nodular sandstone association: (15-24.6 m)

- *Nodular silty sandstone (vi), nodular sandstone (vii)*
- *(Figs. 3.2, 3.5)*

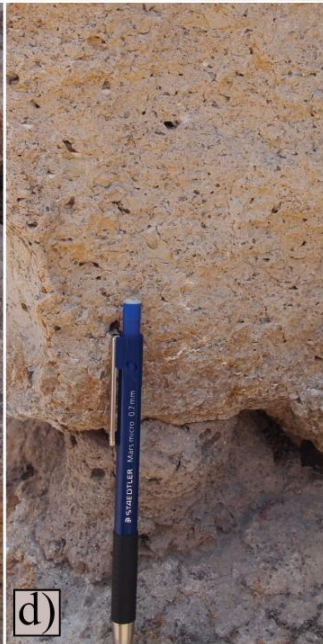


Figure 3.4 a) displays the more massive sands found above the cover at 8 meters where SARP 9-11 has been collected in the massive siliceous silty sandstone facies (v). b) Secondary precipitated silica clusters (facies v). c) Vertical oriented chalsedony vein cutting through the well cemented silty sandstone facies (v). d) Well-cemented sandstone with iron oxide staining and silica clusters with large quartz grains floating in the silty matrix in the siliceous sandy siltstone facies (iv). The surface displays small dissolution cavities. e) Centimeter sized silica veins resembling fossil bones of a vertebrate with iron oxide staining, collected approx. ten meters above basement in the same unit as the SARP 6-10 sample was collected (facies iv)

Figure 3.5 (Next page) displays some examples from the upper eight meters (nodular sandstone facies, vi) of the Saranda profile. a) Sample SARP 12-10 with light gray weathering surface, nodules are less than one cm in size. b) Size of nodules and packing increases upwards, sample SARP13-10. c) Displays common characteristics of the nodular section in a hand sample, silty white circular structures has a high concentration of small, angular quartz grains in the center of the structure, commonly found with iron oxide staining inside, sample SARP 14-10 (Photographed by H. Dypvik). d) Weathering is more pronounced towards the surface, where nodules become more irregular. The interior of the nodules weathers more easily than the crust leaving hollow structures. e) Towards the top, nodules have weathered more, and nodules, example from approx. 21 meter above basement, located between sample SARP 14-10 and SARP 15-10. f) Top of the profile. The uppermost 1,5 meters is highly weathered; individual nodules are no longer visible at the weathering surface, and dissolution cavities are common for this part of the section.

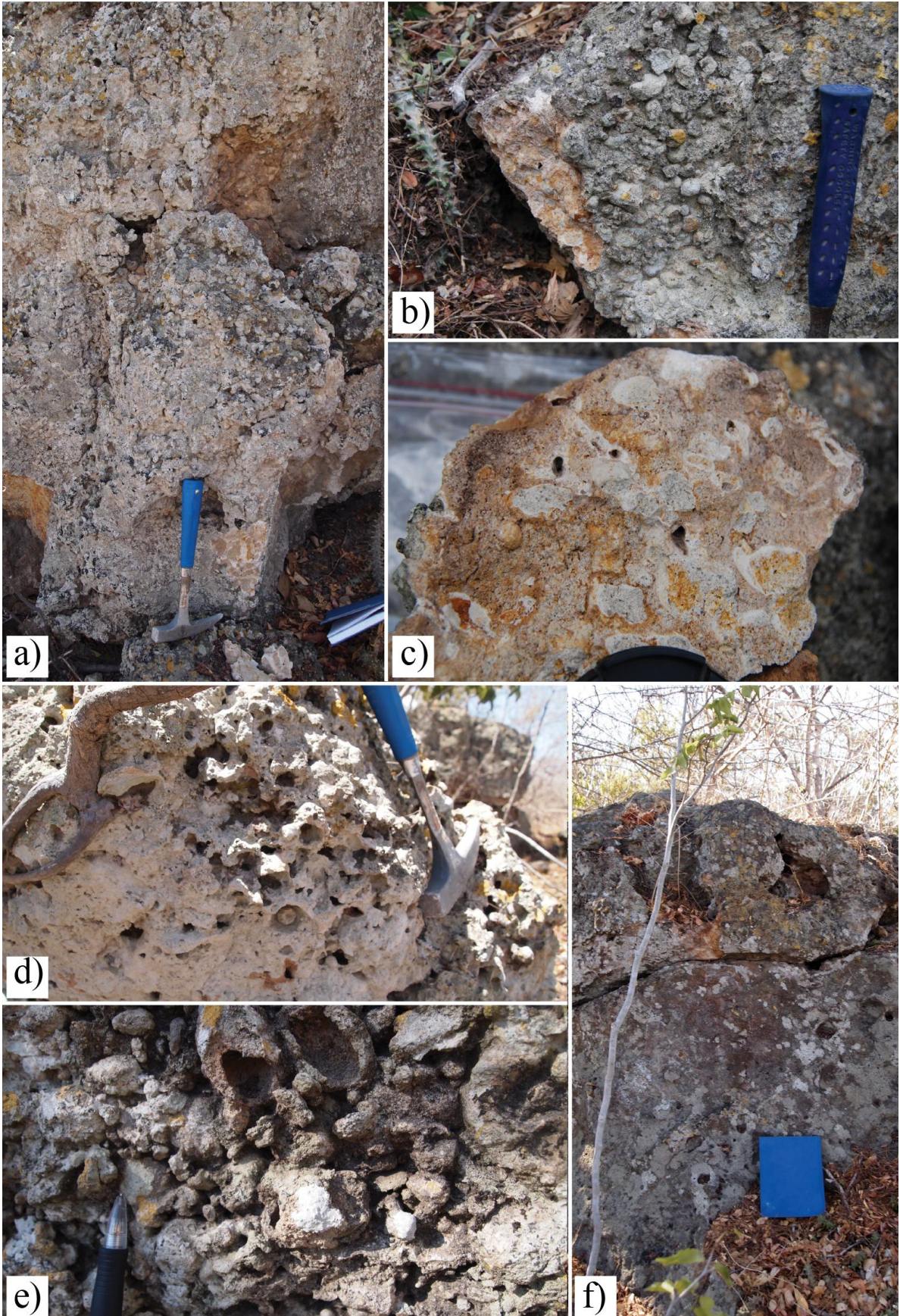


Figure 3.5

(1) The Lower Saranda greenish gray siltstone association

The lowermost facies association is an overall upwards fining sequence with no sedimentary structures observed and has a characteristic pale green colour. The sediment-basement contact is irregular, and the sediments lie unconformably on the weathered pink granite. A coarsening-upwards medium to coarse sand lies at the base (*ii*). Two thin matrix-supported conglomeratic layers (*i*) are situated within the first meter. Siliceous, highly radioactive sandy siltstone (*ii*) is found below and above the conglomerates. A claystone unit (*iii*) is situated at the top of this facies association. Vertical chalcedonic veins cut this unit.

The boundary between FA1 and FA2 was not observed due to a two meter cover.

(2) The Middle Saranda silty sandstone association

The middle facies association is a 7 m upwards coarsening unit, and is composed of two facies: a siliceous silty sandstone (*v*), at the base and the top, and a siliceous sandy siltstone (*iv*) inbetween (*v*). This unit is light beige to off-white in colour and is well-silicified. Sedimentary structures are absent in the lowest five meters, possible bioturbation tracks have been noted in the upper sandy siltstone facies (*iv*). Weak parallel bedding and dish structures have also been observed in the uppermost silty sandstone facies (*v*). Numerous vertically oriented chalcedonic veins have also been found to cut this unit.

The transition between FA2 and FA3 (Figs. 3.2, 3.6) is somewhat irregular. Rocks of FA3 is more weathered than the well silicified FA2 deposits.

(3) The Upper Saranda nodular sandstone association

The nodular facies association is situated at the upper 9.5 m of the Saranda profile (Fig. 3.2). The silty sandstone unit (*vi*) is located at the base of this facies association, and is three meters thick. Nodules in this facies are approximately less one cm in diameter, and have irregularly rounded shapes. Weak indication of parallel bedding is observed in one layer of this facies. A nodular sandstone facies (*vii*) lies above and can be followed to the top. Nodules are bigger and the shape is less rounded than for (*vi*). The size of nodules increases towards the top of the profile, and the nodules become more irregular with increasing distance from the basement. Possible horizontal has been noted in two layers of this facies.

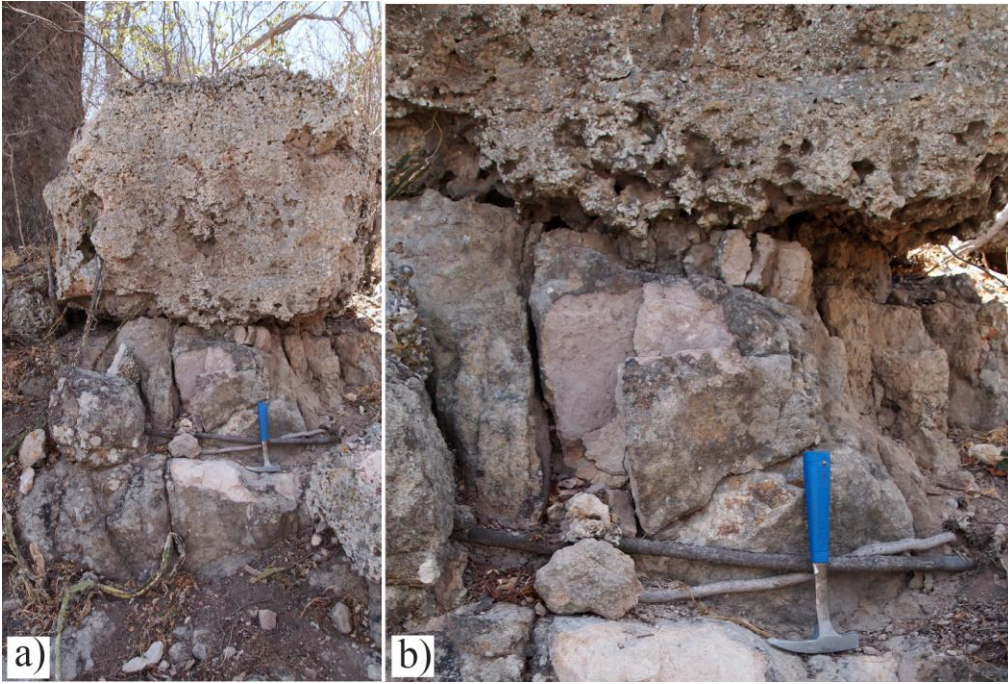


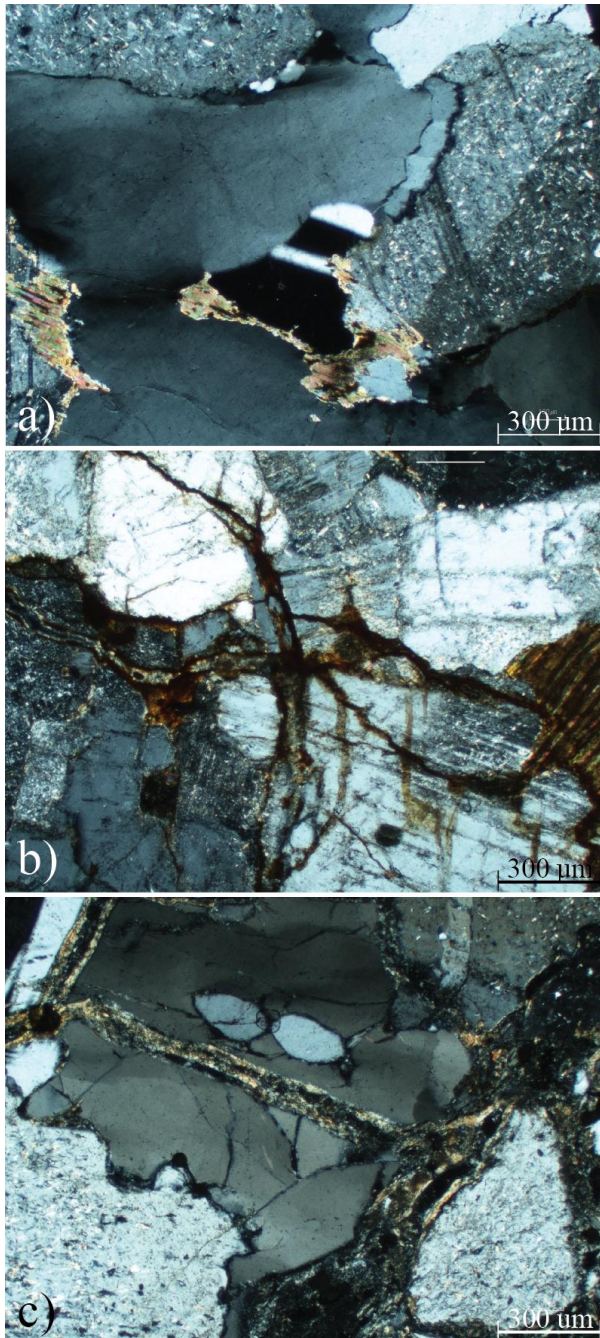
Figure 3.6 Photo of the transition between FA2 and FA3, 15 meter above basement. a) Nodular silty sandstone facies (vi) of FA3, underlain by the siliceous silty sandstone facies (v) of FA2. b) Closer view of the irregular contact between FA2 and FA3. SARP 11-10 has been sampled just above the transition between the two facies associations.

3.2 Petrographic and mineralogical description

3.2.1 Thin section analysis, and point counting

A detailed description of thin section analysis point and counting can be found in Appendix A and B. Twenty-nine thin sections from the Saranda profile were studied in detail. The most important findings are presented here.

Basement



Two samples, SARP Base I and SARP Base II were collected from the granite basement, at 30 and 10 cm below the sediment-basement contact, respectively (Fig. 3.2). The Base II (Fig.3.7b) sample is more weathered than that of Base I (Fig.3.7a), which has a pink colour of fresh rock sample. Base II has a weak pink to greenish colour. Seritization of feldspars is common in both samples, but is more extensive in Base II. Mica is more common in Base II, where biotite and chlorite grains/fragments are fractured into smaller pieces.

Figure 3.7 Basement samples (xpl). a) quartz, chlorite, plagioclase and seritization of plagioclase in SARP Base I. b) the more weathered and fractured SARP Base II shows extensive seritization of feldspars, and fractures are filled with mica and biotite fragments. c) Sample SARP 1-11, a sediment sample collected approximately 20 cm above basement (Fig.3.2) and is very similar to the SARP Base II, but contain a significant amount of fine mica compared to the basement samples.

Facies Association 1

The samples from the lower five meters of the profile are poorly sorted with major variations in grain sizes. The rocks belonging to this facies association are all matrix-supported except from SARP 1-11 (Fig 3.7c), which is grain-supported with small amounts of matrix involved (Appendix A and B). SARP 1-11 appear somewhat similar to the weathered pink granite situated just below (Fig.3.7b).

Grains, independent of size in most cases, are angular to sub-angular and floating in the matrix. The degree of silicification also varies in the lower section, but samples are cemented by silica. The most highly silicified units have chalcedonic quartz infillings in cavities. Three forms of chalcedony have been identified (Fig.3.8c-f): *zebraic chalcedony*, a fibrous mega quartz located in cavity lining with alternating black and white fibre when viewed along the fibre elongation; *radiating bundles of fibres*, which increase in size from the margins of the cavity to the centre; and *chess-like chalcedony*, precipitated in small cracks on detrital grains and are too small to have well-developed radiating bundles (Fig.3.8h). These thin sections also contain large amounts of opaline silica, recognizable by its dark brown appearance (Fig. 3.8 a, g, h) in plain polarized light (ppl), which show isotropic properties under crossed polarized light (xlp).

Point counting (Appendix 3) reveals that these rocks are strongly matrix dominated and can contain up to 81% matrix. Quartz is the most abundant detrital mineral grain, with an average content of 16.8 %. Most of the quartz shows undulatory extinction (> 90%). The total percent of framework grains (qtz, feldspar and rock fragments) in this section is 20%, the average matrix content is 49%. In the lower most samples belonging to this facies association have a very high content of polycrystalline quartz grains, of both pegmatitic and granitic origin. The rocks have low porosity, usually below 10%. No illuviation structures have been observed in this section.

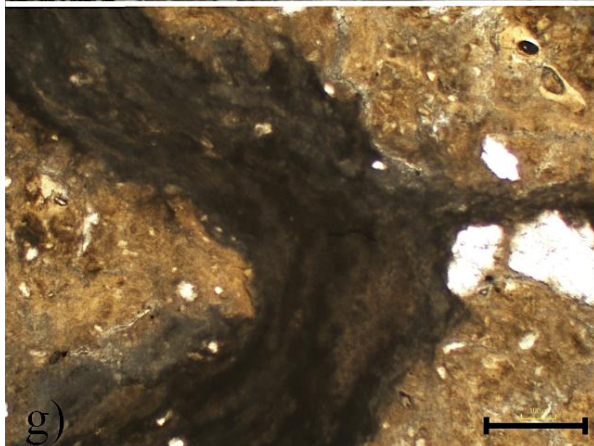
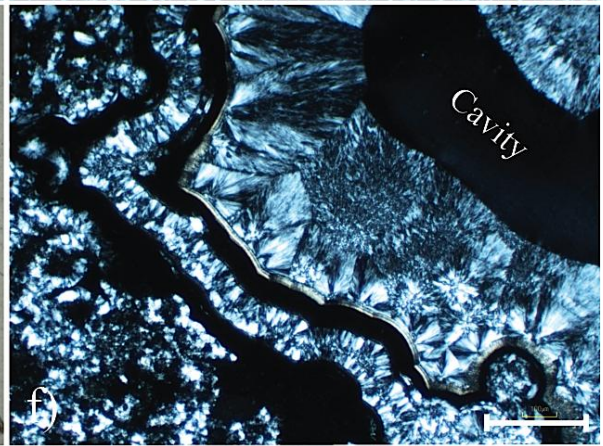
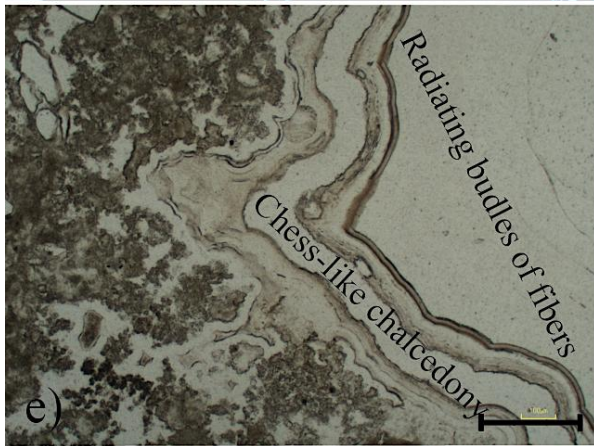
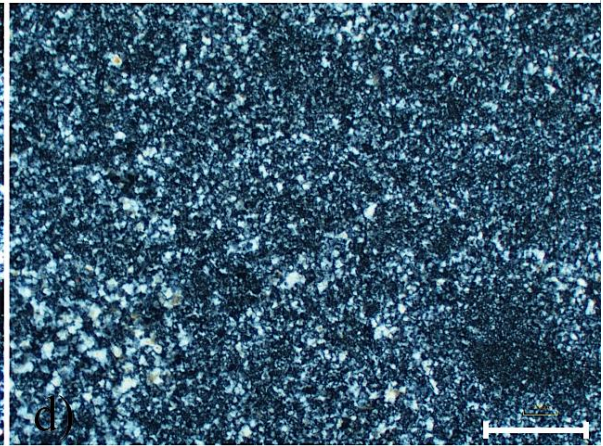
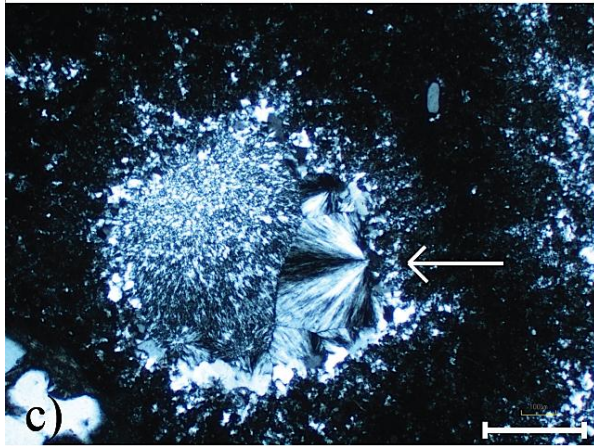
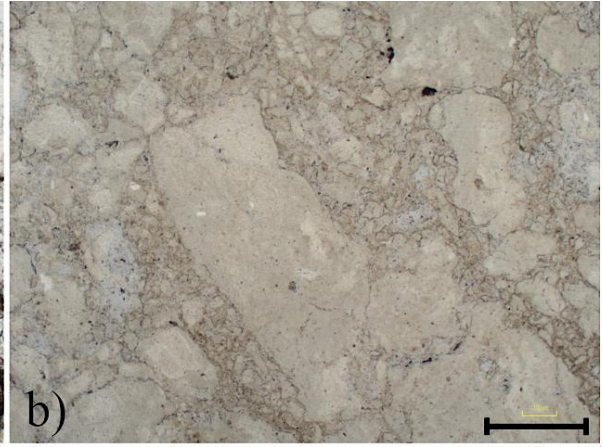


Figure 3.8 Thin section pictures from FA1 samples, displaying different silica species. (Scale line = 300 μm) a, b) White and brown opaline silica in sample SARP 5-11. The entire thin section is of this appearance, and turns black under xpl. Few detrital grains are found within this sample, for most parts, only the outline is seen. c) Zebraic chalcedony (marked by white arrow) together with micro-chalcedony in sample SARP 6-11. d) A huge portion of the sample SARP 8-11 thin section (1/4) is composed of a huge field of micro-chalcedony. e, f) Display zebraic chalcedony, chess-like chalcedony, and radiating bundles of fibers in sample SARP 8-11. Chalcedony has precipitated in a large cavity; the structure is very large, approximately 10 mm in size. g) Brown “cloudy” opal in sample SARP 5-10. Opaline silica is also present in the yellow matrix. h) The poorly sorted SARP 5-10 sample, displaying two silica species; brown “dusty” opal (yellow arrow) , together with a siliceous vein with chess-like chalcedony precipitated in the lining (black arrow)

Facies association 2

In the massive siliceous sandstone unit, grain size increases from the base towards the top of this section while the matrix content decreases upwards (Appendix B). The concentration of grains is higher in this facies association than in FA1, though there are few grains that are in contact with one another, and grain concentration can vary greatly within a single thin section (Fig.3.9 c, d). All samples are matrix supported, and are very fine grained. Grains are angular to sub-rounded with high variations in grain sizes. Colour of the matrix varies from light beige/yellow to brown, green, turquoise and purple, the most common type being the light beige/yellow variant. Brown opaline is present as well, and is easily detectable by its isotropic properties (Fig.3.9 a, b, e). This silica species is restricted to the first five meters of FA2, where its abundance decreases upwards. Some samples also contain chalcedony crystals and microquartz (Fig.3.9 f) precipitated in small cavities and veins, but these are in much smaller quantities than for in FA1. Illuviation structures are found in all samples and are normally associated with veins and pores.

Point counting results reveal that this unit contains an average of 50% more detrital quartz grains than in FA1 (Appendix B). The framework grains make up to 42 % of these rocks. The average portion of matrix is approximately 29%, the remaining amount has mostly been counted as opaline silica or illuviations. The majority of quartz grains show undulatory

extinction, similar to that of FA1. Polycrystalline quartz is extremely abundant in some layers, and both granitic and pegmatitic grains are present in almost equal amounts. This unit also contains the most illuviation structures.

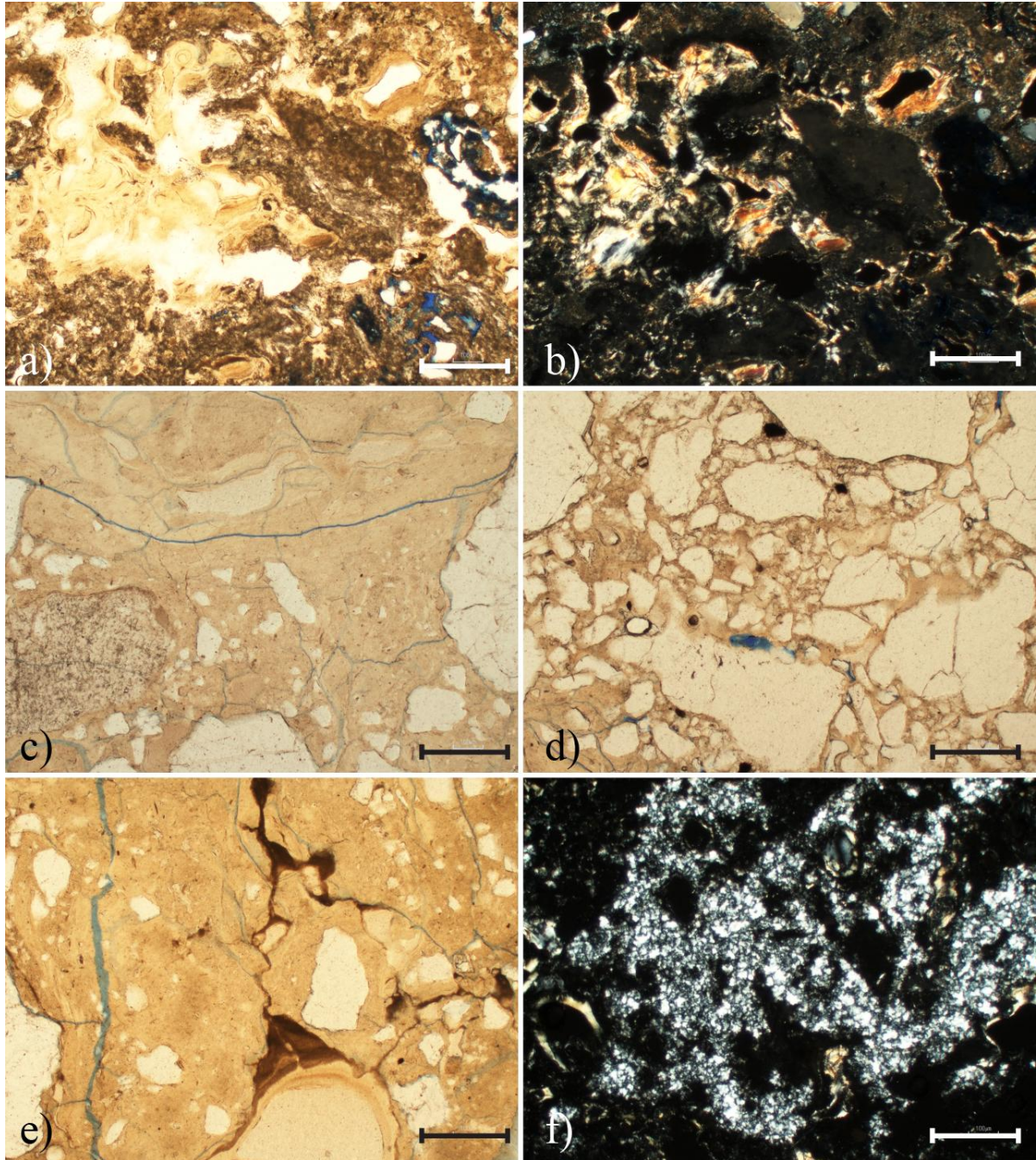


Figure 3.9 Thin section pictures from FA2 samples. (Scale line = 300 μm) a) Ppl picture of brown cloudy opal, interfingering with the matrix, in sample SARP 7-11. b) Xpl view of a) displaying the isotropic appearance of opal under crossed nicols. Photo c and d) from

sample SARP 8-10, displays the variations in fabric that is common for samples collected from FA3. Concentration of grains is low, and poorly sorted in photo c), while in d), the concentration is much higher, and better sorted. e) Brown opal, in SARP 8-10. f) Chess-like chalcedony precipitated in pore spaces, in sample SARP 8-10.

Facies association 3

The samples of FA3 consist of angular to sub-rounded grains of various sizes cemented together by a brown to yellow siliceous matrix (Fig.3.11), which are dark brown/black to yellow in xpl (Fig.3.11b, f). The matrix is not as fine grained as in FA1 and FA2. These rocks are mainly matrix supported, but variations in grain concentration can vary greatly within a single sample. Point counting data show that framework grains in this unit are less abundant than in FA2, approx. 37 %, with quartz making up 36.5 % of this value (Appendix 3). Both polycrystalline and monocrystalline quartz grains are present. Rock fragments have been observed in thin sections, but in such low number that they were missed during point counting. Only a few isotropic and opaque grains have been found. Rocks belonging to FA3 have the highest porosity, with the average value being 29%. Illuviation structures are present but to a lower extent than in the underlying unit (Appendix B).

Nodules appear in thin sections from sample SARP 11-10 and extend to the top of the section. Individual grains show several having lamina enveloped around a nucleus, a detrital grain (Fig. 3.10). Minerals have precipitated along irregularities of the grain edges, several phases of precipitation are seen, and the end product is a rounded structure. Minerals precipitated around detrital grains are not common in SARP 15-10, and are almost absent in SARP 16-10 (Fig.3.11 e, f). Thin section analysis reveals that the nodules visible on a rock sample (Fig.3.5 c) are made up of several of these grains enclosed by final sets of lamina together with regular clastic grains. On thin sections where the right way up has been marked, there is a tendency for the laminae to be thicker towards the bottom of the structure, in the direction of the gravity vector (Fig.3.12a, b).

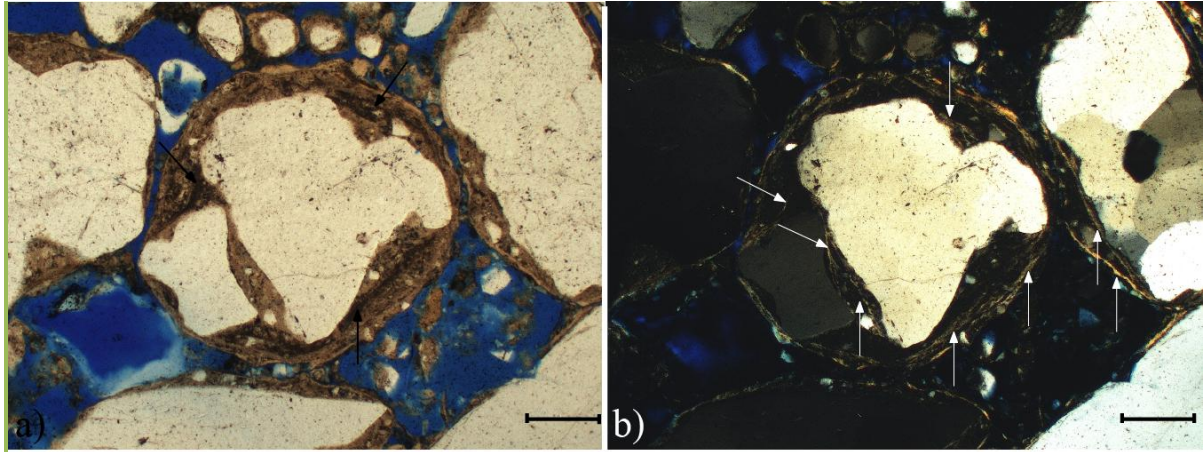


Figure 3.10 Display the development of lamina around a detrital quartz grain, in sample SARP 14-10 (Scale bar = 200 μm). Mineral grains act as a nucleus from which minerals precipitate around. a) Black arrows mark dark brown mineral laminations visible in ppl. Dark brown minerals have precipitated around the two quartz grains in the center of the photo. In xpl b) Several sets of lamina of a different character is visible (white arrows). The first set of lamina has developed around the edges of the quartz grains. The second set is situated at the outer rim of the structure. The brown set of lamina (a) lies between the two yellow laminas.

Opaline silica, in the form of brown opal and chalcedony, has not been observed in FA3 samples, but it is possible that it can exist locally. Light beige to off-white homogenous matrix (Fig. 3.11d, e), is situated around pore spaces and sets of fractures might be opal, but this can be hard to verify in the petrographic microscope.

Samples collected from FA3 have higher porosity than for samples from FA1 and FA2. Highest porosity is usually found in the area between nodules (Fig. 3.12), but high porosity is also found in less developed nodules (Fig.3.12c).

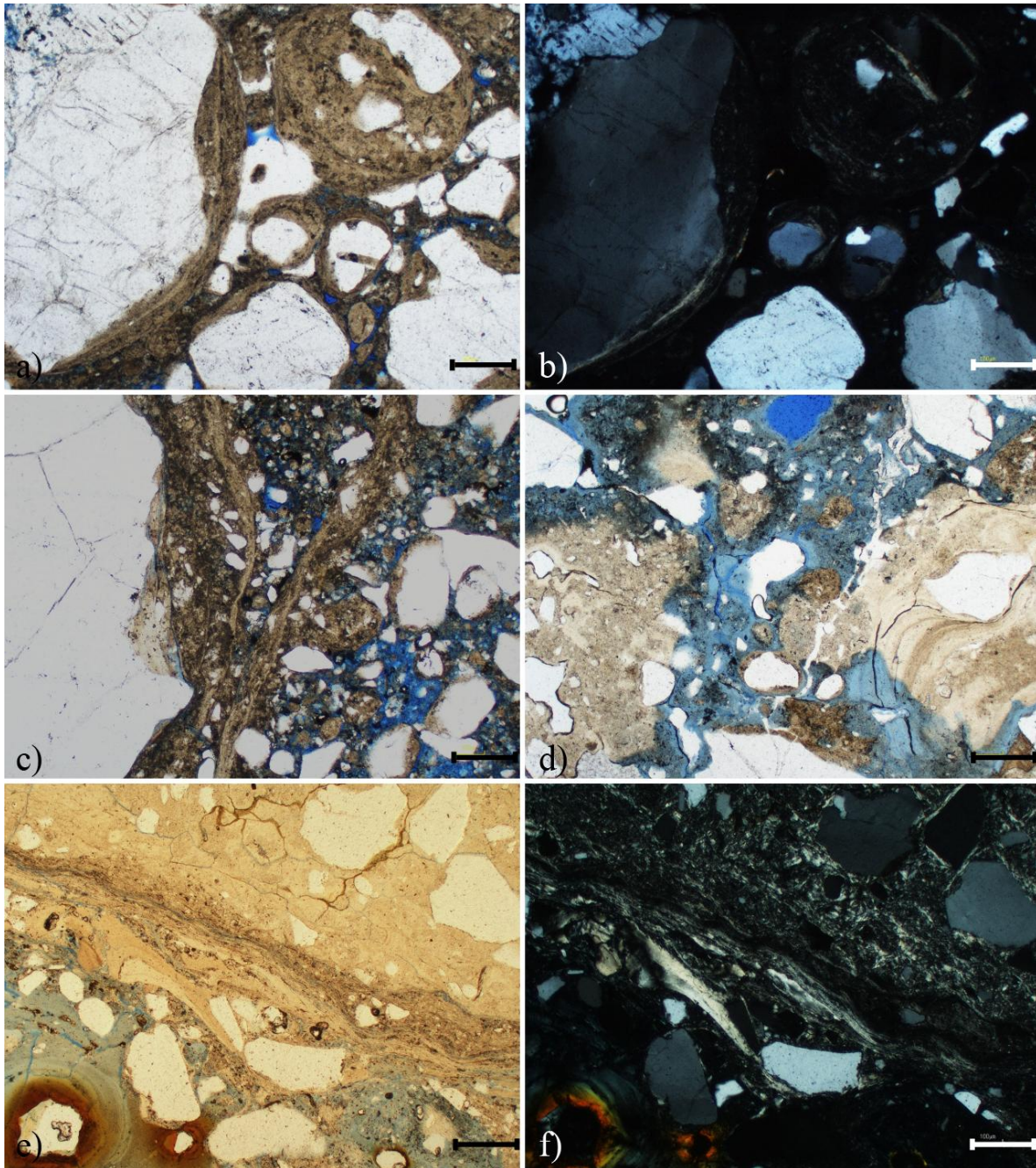


Figure 3.11 Thin section pictures of samples belonging to FA3. (Scale line = 200 µm Rock fragments, quartz and feldspar grains cemented together by a mixture of quartz, kaolinite, and iron oxides. a) Concentric mineral coating around clastic grains in sample SARP 14-10. b) Xpl view of a). c) Displays the outer rim of to nodules that have grown together. Several generations of growth can be seen in this example, SARP 11-10. d) Displays the porous part of a large nodule in sample SARP 12-10. e) Outline of big nodule in SARP 16-10, filling the

entire thin section. The contact between the nodule and the matrix is showed here, with several stages of mineral precipitation visible. f) Xpl view of e).

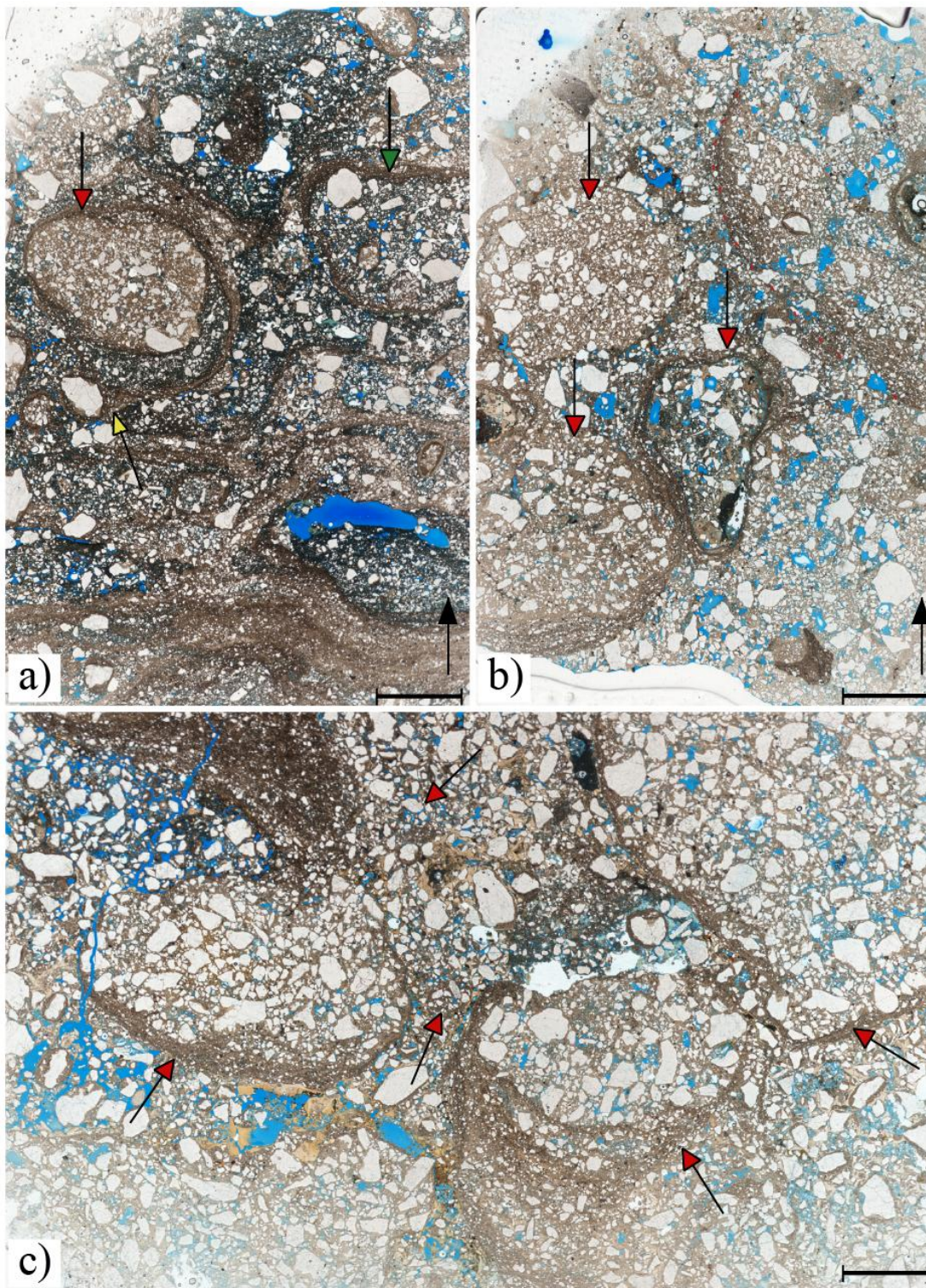


Figure 3.12 Scanned thin sections of three samples belonging to the nodular unit. The black arrow gives the right way up. Scale bare = 40mm. Detrital mineral grains are closely packed

together in the individual nodules, enclosed by dark brown laminas. a) Two nodules are visible in SARP11-10 sample: one well-developed nodule with established matrix in the interior (marked by a red arrow), and a less-developed, porous nodule (marked by a green arrow). Continued nodule growth is seen in the lower nodule, marked by yellow arrow, in the direction of the gravity vector, enclosing more detrital grains. The yellow arrow points to where the nodule growth incorporates an already capped grain, forming the new nodule crust. b) Less distinct nodules in sample SARP 12-10. The final lamina sets are not as clearly developed (as in SARP 11-10). Three clearly bound nodules are marked by red arrows. A red stippled line marks a weak outline of a bigger structure. c) Less rounded and more irregular nodules are found in sample SARP 14-10. Larger mineral grains are situated inside the nodules, than what is found in the lamina sets enclosing the structure. Right way up has not been marked on this samples, but the thickness of the enclosing rims are thicker at one side than the other side.

3.2.2 XRD Results

A total of 27 XRD-recordings were analyzed. The results are plotted as XRD% in Figure 3.13. For more details, see Appendix C.

Quartz is present in all studied SARP samples, while microcline is found in all samples except SARP 1-10. Plagioclase and orthoclase are only detected in samples from FA1. Calcite is present in thirteen of the samples. In the clay fraction, several minerals have been detected with kaolin minerals present in samples 9-11 and upwards. Opal is present in samples from FA1 and FA2.

FA1: Greenish gray siltstone association

Plagioclase and orthoclase are restricted to this facies association, where they exist together with microcline. Orthoclase is present in all samples, while plagioclase is found in eight samples, with the highest content in the SARP 1-11. The quantity of microcline varies greatly in this facies association, and is absent in the SARP 1-10 sample (Fig 3.13). The average microcline content is 26 XRD%. Quartz is present in all samples with the average content being 36 XRD%.

Opal is recognized in 62% of the samples, with an average content of 13 XRD% (Fig 3.13). Opal constitutes over 37 XRD% in SARP 8-11, making it the most abundant mineral present in that sample.

Calcite is present in five samples, and the highest calculated calcite content is found in this association. Maximum values are found in the two lowermost samples (4 and 10 XRD%). Saponite has been detected in five samples with an average content of 3 XRD%. Illite is found in five samples, highest content is found in SARP 3-10 (9 XRD%), and montmorillonite in sample SARP 1-10 (1.5 XRD%). Authigenic flour apatite is present in three samples and is restricted to this facies association. Apatite is the most abundant mineral in SARP 5-11, where it make up over 25 XRD% of the total rock. The content in SARP 3-10 and 5-10 is 2.27 and 4.95 XRD %, respectively.

FA2: Silicified sandstone association

The middle unit mainly consists of quartz, opal, microcline, and kaolinite, with minor amounts of dolomite (one sample), montmorillonite (one sample), and calcite (three samples) (Fig. 3.13).

Quartz is the predominant mineral in this part of the profile. The average quartz content is higher than for FA3, with an average content of almost 60 XRD%, and displays an increasing upwards trend. Opal is present in greater quantities than in FA1, the mean value being 16 XRD%. The four lowermost samples have very high opal content, ranging from 18 to 41 XRD% in SARP 8-10. One sample belonging to this unit (SARP 10-11) does not contain any opaline silica.

Kaolin is first introduced in this facies association (Fig.3.13), present in all samples with an average content of 9 XRD%. The highest content is found in sample SARP 8-10 (Fig.3.13). Microcline is the only feldspar recorded with a lower average content than in the underlying unit (14 XRD%). The microcline content decreases towards the top in this facies association.

SARP XRD%

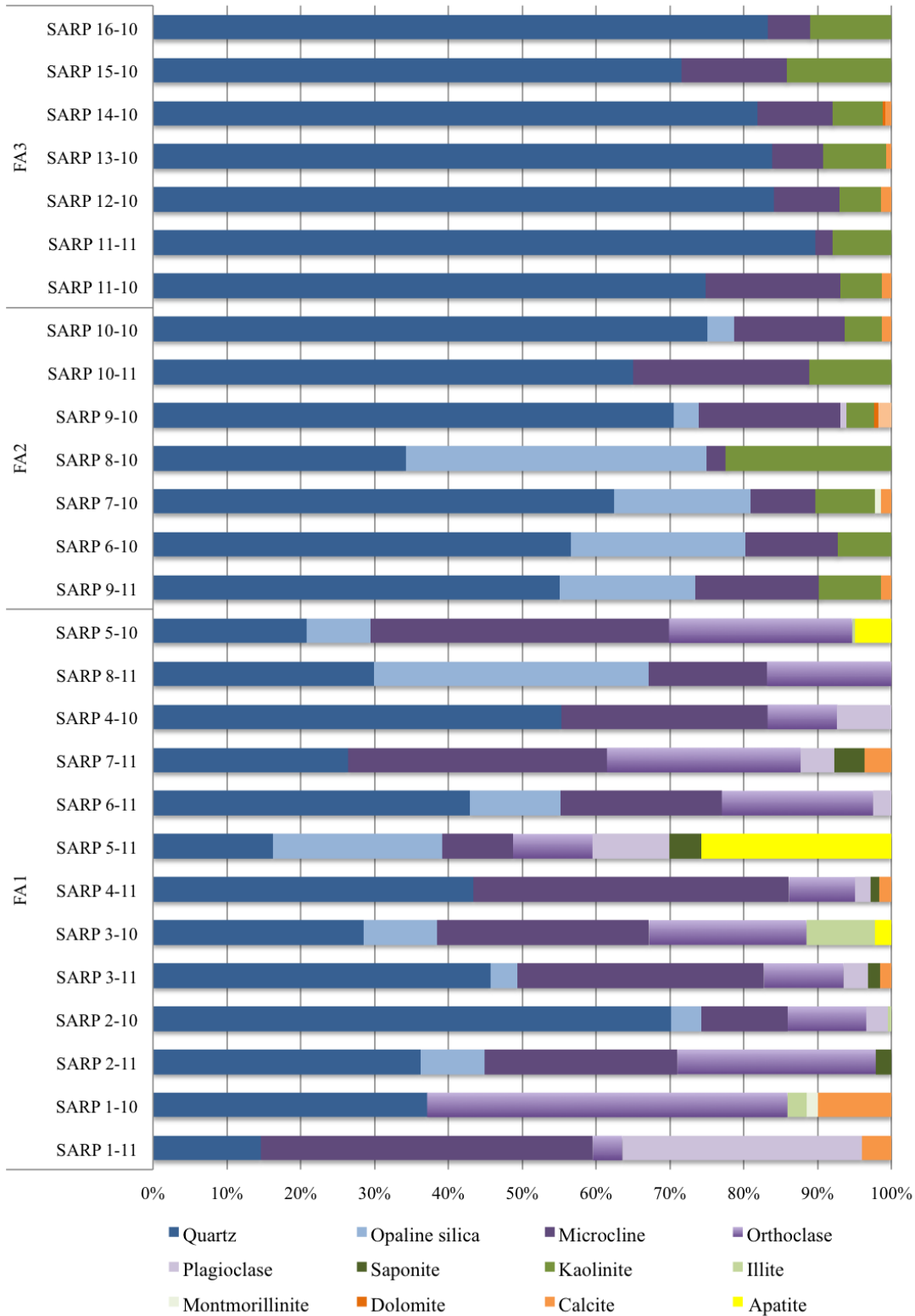


Figure 3.13 XRD % results from the SARP locality. The diagram displays samples collected in both 2010 and 2011, and are intertwined according to their height above basement.

FA3: Nodular sandstone association

The samples from this facies association have a similar mineralogical content as FA2, except it does not contain any opaline silica (Fig 3.13). This unit is characterized as having very high amounts of quartz (80-90 XRD%) which is the most abundant mineral (average XRD% of 83). Microcline is less abundant than in the underlying sections with an average content of 10 XRD%, and displays a decreasing upwards trend. Kaolinite is the only clay mineral recorded, and is found in lower concentrations than in FA2, with an average of 9 XRD%.

Microcline is present in lower concentrations than in the underlying sections. Kaolin is the only matrix component and increases upward to the top of the profile. In the two uppermost samples, kaolin is present in a greater degree than microcline. None of the samples contain any traces of opaline silica, and calcite has been detected in four samples.

Quartz / Total Feldspar ratio

Quartz / total feldspar ratio for every sample has been calculated, and is presented in **Figure 3.x**.

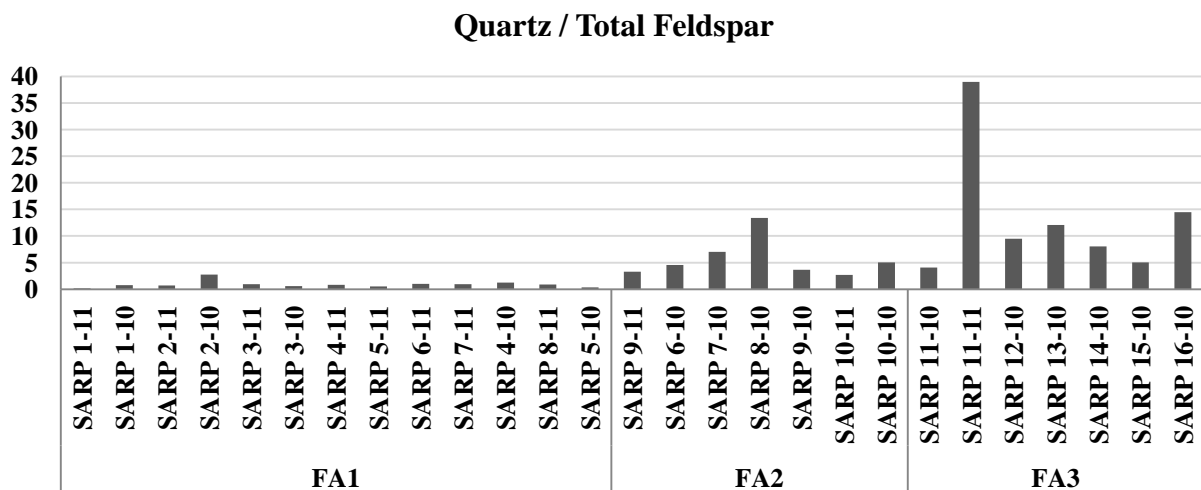


Figure 3.14 Quartz / Total Feldspar ratio for SARP samples. The ratio in FA1 samples are low compared to FA2 and FA3.

The average Quartz / Total Feldspar ratio increases upwards from FA1 to FA3. Lowest ratios are found in FA1 samples with the average ratio being 0.9. The average ratio in FA2 samples

is 5.7, and increases further in FA3 with the average ratio of 13.2. Highest quartz / total feldspar ratio is found in sample SARP 11-11 with the value 39.

Opaline silica

From XRD analysis (Fig.3.13), 14 samples were found to contain opaline silica. All opals from the Saranda profile have d -spacing values between 4.08 to 4.12 Å, and can therefore (according to Table 2.5) be classified as opal-CT (Table 3.1). The two peaks used to identify opal-C have not been recorded in any samples.

The most common d - spacing in the SARP samples is 4.11 Å, and a total of seven samples have been recorded with this value. The lowest value is recorded in the SARP 2-11 sample (4.08 Å), while the highest recorded d -value is found in the sample SARP 10-10 of the middle facies association. Opals within FA1 have lower d -values than opals found in FA2

Table 3.2 contains information about peak positions, peak width at half height of the main peak, other characteristic peaks, and the structural group each opal belongs to.

Table 3.2 Structural groups, d values for the main peaks, and peak width at half height for the main peak (ΔH). All opals are classified as opal-CT.

Opal typology	Tridymitic shoulder (Å)	Main peak (Å)	Secondary peak (Å)	ΔH	Structural group
SARP 1-11
SARP 1-10
SARP 2-11	...	4.08	2.49	0.819	CT
SARP 2-10	...	4.11	2.49	1.062	CT
SARP 3-11	...	4.10	2.49	0.8	CT
SARP 3-10	...	4.11	2.50	1.092	CT
SARP 4-11
SARP 5-11	4.32	4.10	2.50	0.965	CT
SARP 6-11	...	4.09	2.50	0.888	CT
SARP 7-11
SARP 8-11	...	4.09	2.49	1.002	CT
SARP 5-10	4.32	4.10	2.49	0.978	CT
SARP 9-11	...	4.11	2.50	1.127	CT
SARP 6-10	...	4.11	2.51	1.105	CT
SARP 7-10	...	4.11	2.51	1.197	CT
SARP 8-10	...	4.11	2.51	1.339	CT
SARP 9-10	...	4.11	2.50	1.293	CT
SARP 10-11
SARP 10-10	...	4.12	2.51	1.092	CT

3.2.3 Scanning electron microscope (SEM) and electron microprobe (EMP) results

Eleven samples (SARP 2-10, SARP 2-11, SARP5-11, SARP 5-10, SARP 9-11, SARP 7-10, SARP 9-10, SARP 11-10, SARP 14-10, SARP 15-10, SARP 16-10) from the Saranda profile have been studied under a scanning electron microscope. Additionally, one sample of a silica vein collected from the same unit as SARP 6-10 (FA2) was also analyzed. Three samples have been studied by the EMP (SARP 2-10, SARP 5-11, SARP 5-10). The main results are presented below.

FA1: Greenish gray siltstone association

SEM analysis of the very fine-grained matrix gave indication that kaolinite was the major matrix mineral. XRD recordings (Fig.3.13) indicate that this is not correct. The microprobe was then used to assist in the very fine matrix identification, since the irradiation beam used in the SEM was too large for studying the finest grains, and therefore collected additional information from the surrounding grains. The microprobe beam has a suitable size for such analysis, and revealed that the main components in the matrix were a mixture of extremely fine grained k-spar, opaline silica, and, to a smaller degree, apatite (Figs.3.15, 3.16).

K-spar appears as light gray fields in the electron microprobe, while opal has a dark gray colour (Figs.3.15, 3.16). Opal was identified by the sudden appearance of a hole after it was irradiated with the microprobe beam due to water loss in the crystal structure. Silica overgrowth was also detected around detrital quartz grains (figure 3.16).

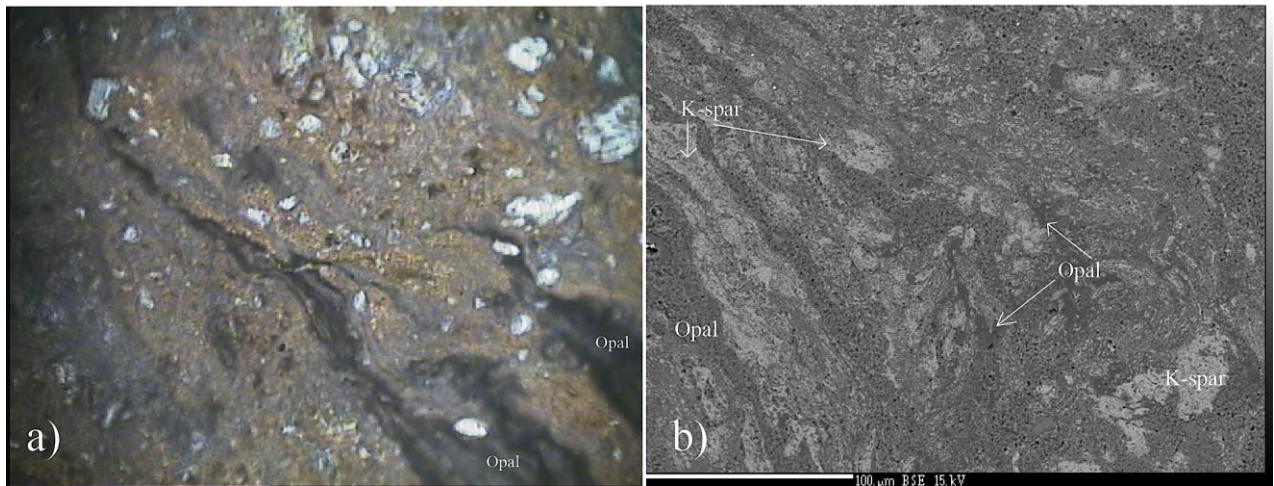


Figure 3.15 Electron microprobe photos of sample SARP 5-10. a) Close-up photo of the thin section, the dark brown feature is opal (no scale). b) Magnification of the matrix, light gray areas is k-spar, dark gray is opaline silica (scale: white line = 100 μ m).



Figure 3.16 Electron microprobe analysis of SARP 2-10. The matrix is composed of k-spar and opaline silica. Overgrowth by opaline silica on quartz grains have been detected

throughout this thin section. K-spar (appears as light gray spots) are scattered around together with opal (as dark gray).

All samples analyzed by the SEM from FA1 have been found to contain opaline silica as opal-CT. Opal-CT is commonly associated with silica growth in small cavities in the rock. Different forms of opal-CT have been found; the most common species being composite lepispheres found in cavities, resembling cauliflower (Fig.3.17 a). Individual structures can be as large as 100 μm in diameter and are commonly found in clusters. Amorphous siliceous rims surround these cavities. Small well-bladed opal-CT lepispheres ($\sim 5 \mu\text{m}$), have been found in SARP 5-11 and 2-11 (Fig.3.17 b, e). The individual opal-CT blades have intergrown at a 70 degree angle. They most commonly occur as individuals precipitated on the surface of detrital grains, but can, in some places, be found as clusters in cavities. Opal-A, together with authigenic k-spar, in sample SARP 5-10 is the only sample found to contain this opaline species (Fig.3.17 c).

Nicely developed, euhedral apatite (Fig.3.17 d) and k-spar crystals (Fig.3.17 c) have both been found in association with opal. K-spar together with opal has been found to be the main matrix components in a number of the samples from the lower section. Apatite has only been detected in three samples (Fig. 3.13), where it together with k-spar and opal, constitutes the major matrix components.

FA2: Silicified sandstone association

Three samples from the FA2 section were analyzed by SEM in addition to a silica vein sample collected from the SARP 6-10 level. All samples show clear signs of silicification, as opal-CT lepispheres are a very common feature in these rocks. Two stubs were produced from the silica vein sample, one of the interior of the vein, and one of the outer crust. The interior of the vein showed well-developed opal-CT lepispheres, 5-10 μm in diameter, closely resembling balls of yarn (Fig.3.17 i, j). The lepispheres of bladed cristobalite display the characteristic intergrowth of the individual blades at a 70 degree angle. The lepispheres are, in most cases, only visible in cavities, otherwise they form an interlocking fabric, which

forms a bright and structureless surface. Less-developed and much smaller opal-CT lepispheres are found at the outer part of the vein (Fig.3.17 k, l). The majority of the lepispheres have a diameter of 2 μm , the largest being no more than 5 μm across. A number of these lepispheres are partly covered by detritus and cemented. Examples of clay cutans have also been observed (Fig.3.17m). In other samples analyzed, only composite opal-CT lepispheres were identified (Fig. 3.17g, h).

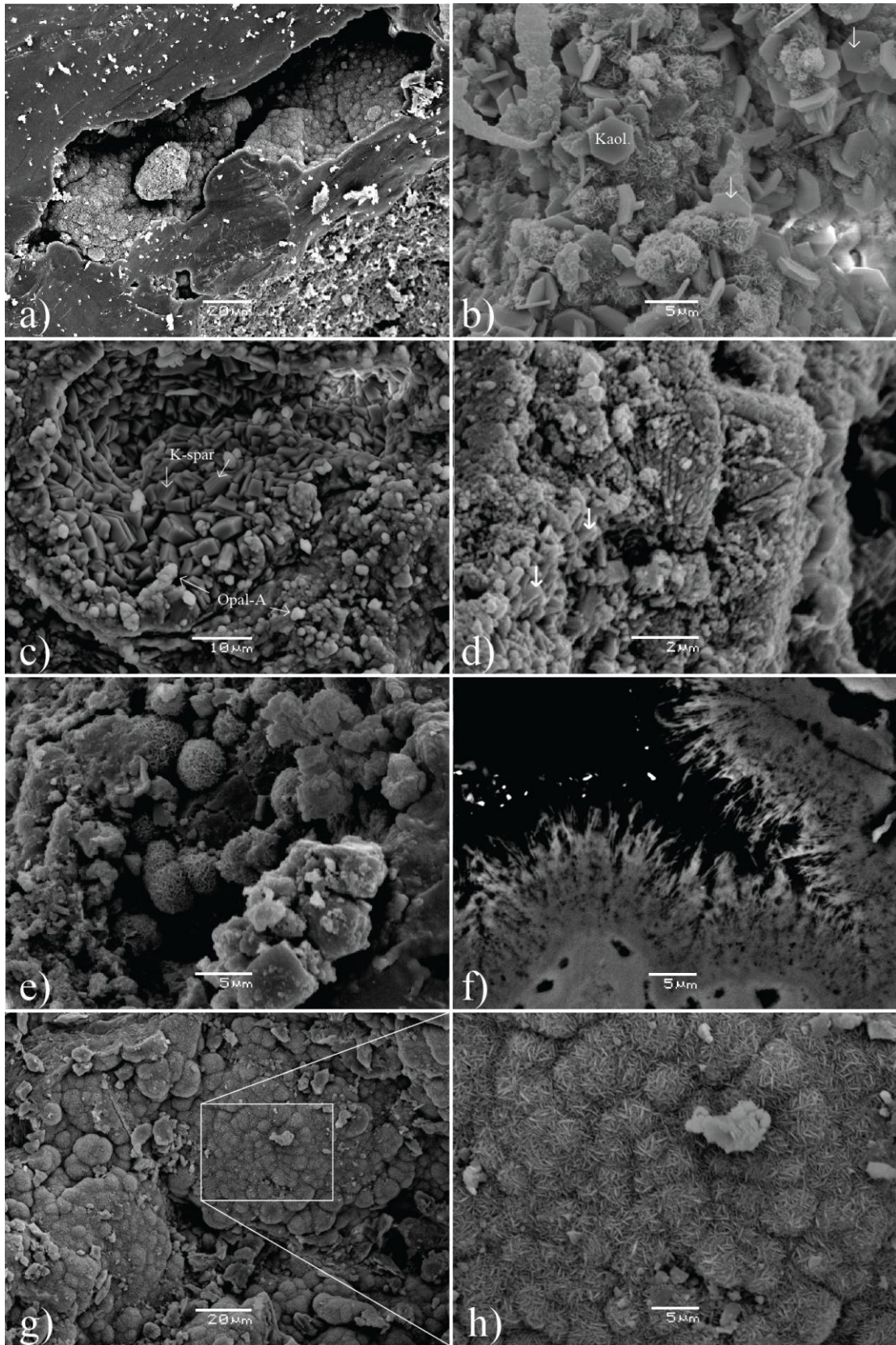


Figure 3.17

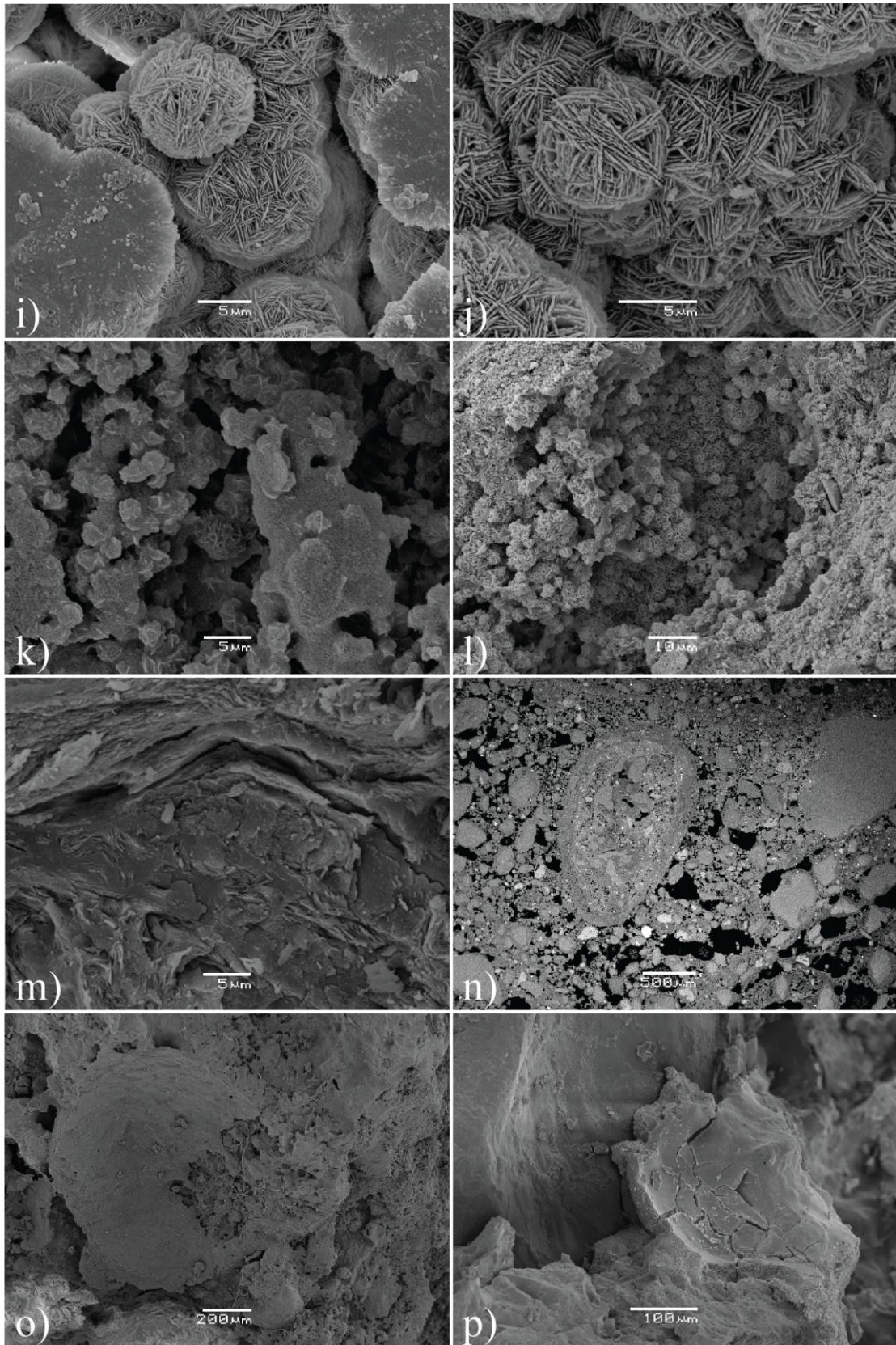


Figure 3.17 Continued

Secondary electron image (a-e, g-m,o and p), and backscatter electron images (f and n) of selected SARP samples. a) Clusters of composite lepispheres in small cavity, SARP2-10. b) Authigenic kaolinite together with small opal-CT lepispheres, SARP 2-11. c) Authigenic potassic feldspar together with opal-A in sample SARP 5-10. d) Authigenic apatite, marked by white arrow in sample SARP 5-11. e) Opal-CT lepispheres in sample SARP 5-11. f) A small part of a chalcedony crystal, precipitated at the edges of a cavity in sample SARP 5-11. g) Composite lepispheres resembling cauliflowers, precipitated in cavity in sample SARP 9-10. h) Close-up picture of g). i-l) Silica vein, one centimeter broad, collected from the same layer as SARP 6-10. Picture i and j display well-developed opal-CT lepispheres from the center of the vein. The crust of the vein, k and l, has fewer well-developed and smaller opal-CT lepispheres. m) Clay cutan consisting mainly of AlSiO, in sample SARP 9-11. n) Small nodule composed of small clastic grains of mainly quartz in sample SARP11-10. o) Small concretion in sample SARP 11-10. The concretionary surface is partially dissolved, revealing the interior which is composed of small clastic grains. p) Quartz grain, partially enclosed by a mixture of kaolinite and quartz.

FA3: Nodular sandstone association

Four samples from FA3 were studied under the SEM. This unit has a very different appearance compared to the two underlying units. First, samples analyzed by the SEM did not contain any opals. Second, the entire surface of the stubs analyzed has a crumbly texture, covered by concretions around clusters of clastic grains. Some of the concretions were partially broken/dissolved, revealing the interior (Fig. 3.17o). The BEI image, Figure 3.17 n, displays how the interior typically looks. The concretions are composed of angular quartz grains of various sizes, framed by several sets of lamina. The best developed ones have also established matrix within the concretion. Both the interior and the outer crust consist of a mixture of kaolinite and silica, the content of Al, Si, and O varies between the different laminations. Some have also been found to contain minor amounts of iron.

Quantitative analysis of garnet, spinel, and ilmenite

EMP analysis of selected isotropic and opaque minerals in the SARP 5-11 and 2-10 samples reveal different mineralogical compositions (Table 3.3). From the conglomerate sample SARP 2-10, spinel, garnets, and ilmenites were analyzed (Figs. 3.18, 3.19). Only spinel was analyzed from sample SARP 5-11. Results reveal that some of the SARP 2-10 grains are made up of minerals with quite a diverse composition.

Spinel found in SARP 5-11 have a very high Cr content, ranging from 21% to as high as 42%. Cr-rich spinels also occur in SARP 2-10 where the Cr content is even higher. A red spinel (Fig.3.18) stands out from the rest as it has an abnormally high value in aluminum (33%) and a slightly lower Cr-value than the rest of the spinels in the same sample. It is worth noting that Mg-rich ilmenites (~10%) and Cr-rich garnets were also identified in the same sample. The ilmenites have similar, but higher magnesium content. Garnets vary slightly in composition and have unusually high Cr-values. One in particular stands out from the rest, sample almost has 8% Cr and contains smaller amounts of aluminum than the other garnets.



Figure 3.18 Cross section of the SARP 2-10 sample, displaying the variety of mineral grains in the conglomerate.

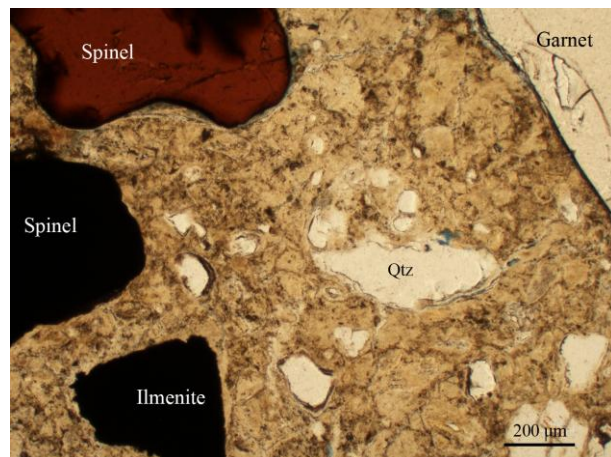


Figure 3.19 Mineral grains in sample SARP 2-10 (Fig.3.17) analyzed by EMP.

Table 3.3 Electron microprobe results from quantitative analysis of garnet, spinel and ilmenite from SARP 5-11 and SARP 2-10. Deviation from normal values are highlighted with a darker colour. Numbers are given in percent.

Mineral	Sample	SiO ₂	Al ₂ O ₃	MgO	Na ₂ O	TiO ₂	FeO	MnO	Cr ₂ O ₃	CaO	Total
Spinel	SARP 5-11	0.1	10.3	13.3	0.0	6.8	26.3	0.3	42.4	0.1	99.6
Spinel	SARP 5-11	0.1	10.4	13.7	0.0	7.8	29.4	0.4	35.9	0.1	97.7
Spinel	SARP 5-11	0.1	9.2	14.4	0.0	13.0	37.9	0.5	21.4	0.2	96.9
Ilmenite	SARP 2-10	0.0	0.4	10.3	0.0	53.9	35.2	0.2	0.1	0.0	100.0
Ilmenite	SARP 2-10	0.0	0.3	9.8	0.0	53.1	35.6	0.2	0.3	0.0	99.3
Ilmenite	SARP 2-10	0.0	0.3	10.2	0.0	53.7	35.5	0.3	0.1	0.0	100.2
Garnet	SARP 2-10	41.1	17.4	20.3	0.0	0.6	6.9	0.3	8.0	6.0	100.6
Garnet	SARP 2-10	42.3	22.2	20.9	0.1	0.6	8.9	0.3	1.0	4.7	101.1
Garnet	SARP 2-10	42.2	21.4	21.2	0.0	0.6	7.7	0.3	2.3	5.2	100.8
Garnet	SARP 2-10	41.5	22.1	20.1	0.1	0.9	9.8	0.4	0.7	5.1	100.6
Garnet	SARP 2-10	41.5	21.9	20.6	0.0	0.6	8.9	0.3	1.2	4.9	100.0
Spinel	SARP 2-10	0.2	13.8	12.3	0.0	2.8	19.8	0.1	49.9	0.0	98.9
Spinel	SARP 2-10	0.1	11.3	12.4	0.0	3.2	17.1	0.2	55.8	0.0	100.1
Spinel	SARP 2-10	0.2	9.3	10.2	0.0	3.5	21.1	0.1	54.7	0.0	99.3
Red spinel	SARP 2-10	0.0	33.3	15.5	0.0	0.1	13.2	0.1	37.8	0.0	100.0

Bismuth oxychloride

SARP 5-11 contains small grains of bismuth oxychloride mineral known as Bismoclite (**Fig.3.19**). The small mineral grains are no more than ten µm in diameter, and have an angular grain shape. This mineral has not been detected in any other samples.

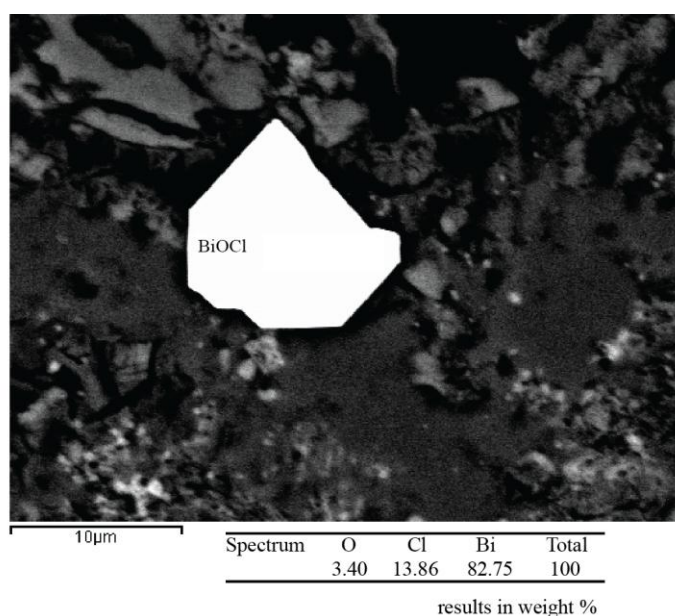


Figure 3.20 Figure x Quantitative analysis of a bismoclite mineral grain, by EMP.

3.3 Geochemical analysis

Selected data from the geochemical analysis of elements will be presented, while a complete list of the geochemical results can be found in Appendix D. Additionally, element correlation coefficients for elements in each facies association has been calculated and is given in Appendix F.

3.3.1 Element concentrations

The geochemistry of the Saranda profile is complex and major and minor variations are seen within the three facies association. Generally, the lowermost facies association, FA1, shows higher element concentrations than what is seen in FA2 and FA3. FA1 are also enriched in REE, and associated with the highest uranium distribution.

Table 3.4 Comparison between the average element concentrations of selected elements in the earths crust compared with the average concentration in each facies associations. Information on crustal values from Taylor (1965).

Element	Average value crust	Average concentration FA1	Average concentration FA2	Average concentration FA3
Sr	375	96	62	81
Ba	425	1151	538	1441
V	135	238	75	17
Cr	100	638	249	269
Co	25	14	8	3
Ni	75	127	41	22
Cu	55	15	16	14
Zn	70	58	51	35
Ga	15	17	18	19
Ge	1.5	1	1.8	2
Sn	2	2	1.6	3
Pb	12.5	16	19	30
As	1.8	11	7	7
U	2.7	54	11	8
Th	10	13	9	8
Nb	20	12	18	17
Rb	90	128	314	193
Li	20	21	249	228

FA1:

Samples from the lower section are the ones that have the highest enrichment in elements. Concentrations of nickel, chromium, vanadium, thorium and uranium generally decrease towards the top of the profile.

All samples from the lower facies association show enrichments in chromium; one sample especially (SARP 2-10) shows extreme Cr enrichments with 4520 ppm. SARP 2-10 also shows high concentration of Sn (8.7 ppm), V (503ppm), and Nb (35 ppm). FA1 samples have the highest uranium distribution (average ~54 ppm). The highest uranium concentrations are found in samples SARP 5-11(394 ppm) and SARP 5-10 (94 ppm). Natural gamma radiation in these two units has been measured to be 1,200 and 1,000 cps, respectively.

Ba, V, Ni, Pb, As, Th, and Rb are also enriched (Table 3.x). In addition, the SARP 5-11 sample displays extreme enrichments with respect to the element Bi. Sample SARP 5-11 has a concentration of 7.2 ppm (40 times the average Bi distribution in the crust, Taylor (1965)).

FA2:

Of the selected elements in Table 3.3, samples from FA2 are more enriched in Li and Rb than the two other sections. Samples contain at the average twelve times as much lithium, and over three times Rb as the average composition of the crust. From the same table, FA2 is also enriched in Ba, Cr, Pb, As, U.

FA3:

Highest barium values are found in the uppermost unit with the average Ba distribution of 1441 ppm. Highest recorded Ba concentration in this unit is 2370 ppm in sample SARP 12-10, while the lowest recording is SARP 11-11. High concentrations of Cr, Sn, Pb, As, U, Rb, and Li is also found. See Appendix D for more details.

Samples from the lower section are the ones that have the highest enrichment in elements. Concentrations of nickel, chromium, vanadium, thorium and uranium generally decrease towards the top of the profile. The highest concentrations of the elements (**table x**) are all found in the lowermost facies association.

3.3.2 *Rare Earth Elements (REE)*

Table 3.5 Comparison between the average REE concentrations in the earths crust compared with the average concentration in each facies associations. Additionally, the SARP 5-11 sample has been included, due to is very high distribution of some REE. Information on crustal values from Taylor (1965).

REE	Average value crust	Average concentration FA1	Average concentration FA2	Average concentration FA2	Concentration SARP 5-11
La	30	35	25	22	138
Ce	60	80	51	45	296
Pr	8.2	9	5	3.5	37.1
Nd	28	34	16	11	147
Sm	6	7	2.5	2	35.7
Eu	1.2	1.2	0.4	0.1	7.21
Gd	5.4	5	1.7	1.1	25.3
Tb	0.9	0.7	0.3	0.3	3.8
Dy	3	4	1.4	0.1	20.2
Ho	1.2	7	0.3	0.3	3.5
Er	2.8	2	0.7	0.7	9.6
Tm	0.48	0.3	0.1	0.1	1.4
Yb	3	2	0.9	1	9.5

The lowermost facies association show high concentration of REE, and shows enrichments in almost every REE analyzed, except for Gb, Tb, Er, Yb (Table 3.5). These high values are du to extreme enrichments in sample SARP 5-11. FA2 and FA3 have lower REE distribution.

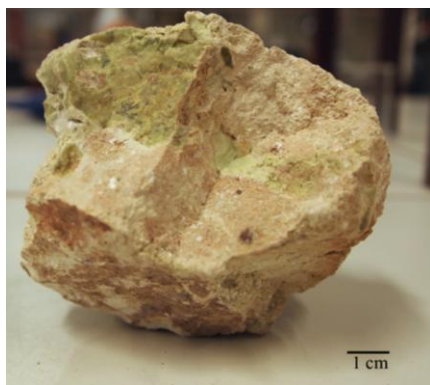


Figure 3.21 Sample SARP 5-11

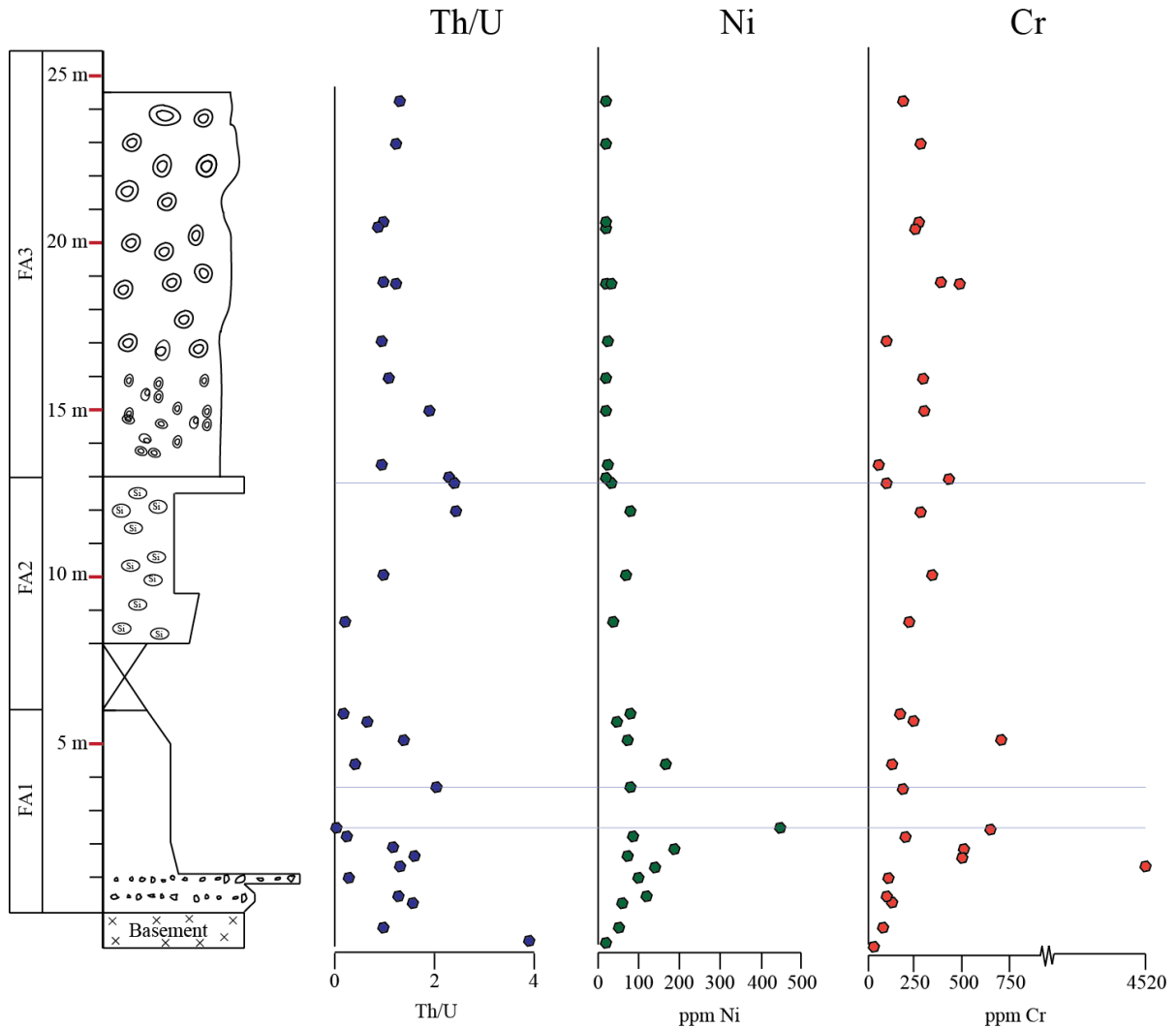


Figure 3.19 Distribution of Th/U ratios, Ni and Cr concentrations in the Saranda profile.

Three levels stand out, marked by blue lines. Lower line, the Th/U ratios are low, Ni and Cr values are high. The middle line shows the opposite trend, with higher Th/U ratios and lower Ni and Cr values. The upper line marks the level with the highest Th/U ratio, the lowest Ni content and low Cr values.

The thorium/uranium ratios vary within the profile (Fig.3.19). Two minor upwards decreasing trends of Th/U ratios in can be seen in the lower part of FA1 until it reaches the lowest limit in the SARP 5-11 sample level (lower blue line). In the same interval, Ni and Cr show an upwards increasing trend towards. Highest recorded Ni value is in sample SARP 5-11, where Cr concentrations are also very high. An abrupt increase in Th/U ratio is seen in

the SARP 6-11 sample above, with low Ni and Cr concentrations (middle blue line). From this point, Th/U ratios continue to decrease towards the top of FA1, where the Ni distribution displays a decreasing upwards trend, and Cr values roughly show an increasing upwards trend. The highest recorded Cr value is at the lower part of FA1 in sample SARP 2-10, where it shows an extreme enrichment (4520 ppm).

A upwards increase in the Th/U ratios is seen in FA2 samples, where a similar trend is seen in the Ni and Cr concentration, though not as pronounced. The uppermost unit of FA2 is marked by the highest Th/U ratio and the lowest recorded Ni and Cr concentrations (upper blue line, Fig. 3.19).

The transition between FA2 and FA3 is marked by a decrease in the Th/U ratio, and it continues to decrease until the 16 meter mark (SARP 11-10) above the basement (Fig. 3.19). From this point upwards, the Th/U ratios are more or less constant. The Ni distribution is low throughout FA3, with a similar distribution in all samples. Cr distribution varies some but roughly display a linear trend.

4 Chiguluka

Facies description

The CHIG locality (Fig.1.6) is situated in a river bed that lays dry for most of the year. Two sections were logged (CHIG I and CHIG II) in the scale 1:20 (Fig.3.22) on different sides of a river bend that flows through the village of Chiguluka

Table 4.1 Geographical positions for CHIG-localities

	Latitude	Longitude
CHIG I	06° 18, 872	35° 25, 426
CHIG II	06° 18, 819	35° 25, 445

The two sections logged are overall upwards fining and lay unconformable upon the basement rocks whereas the upper part of the exposed basement is somewhat weathered. The sediment-weathered basement-basement contacts are uneven and it is apparent that there have been some infilling of sediments in the weathered basement.

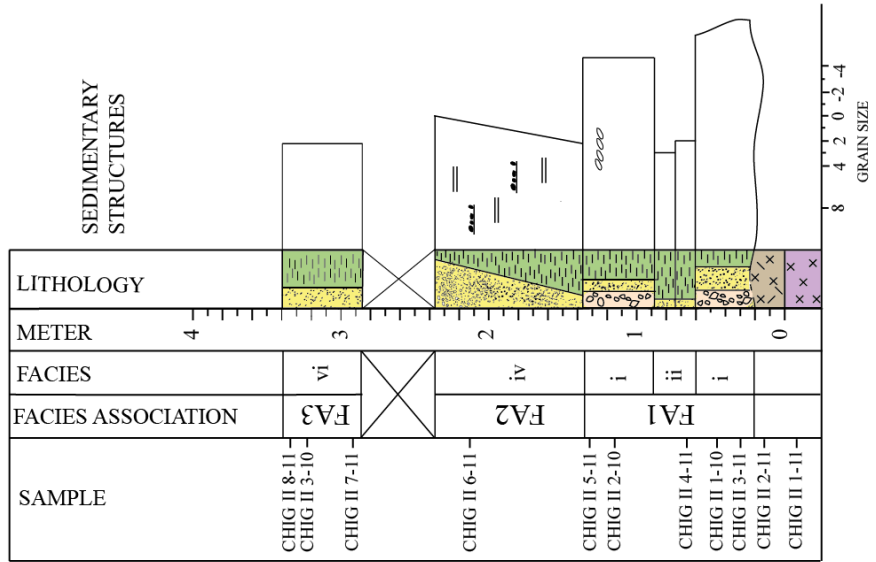
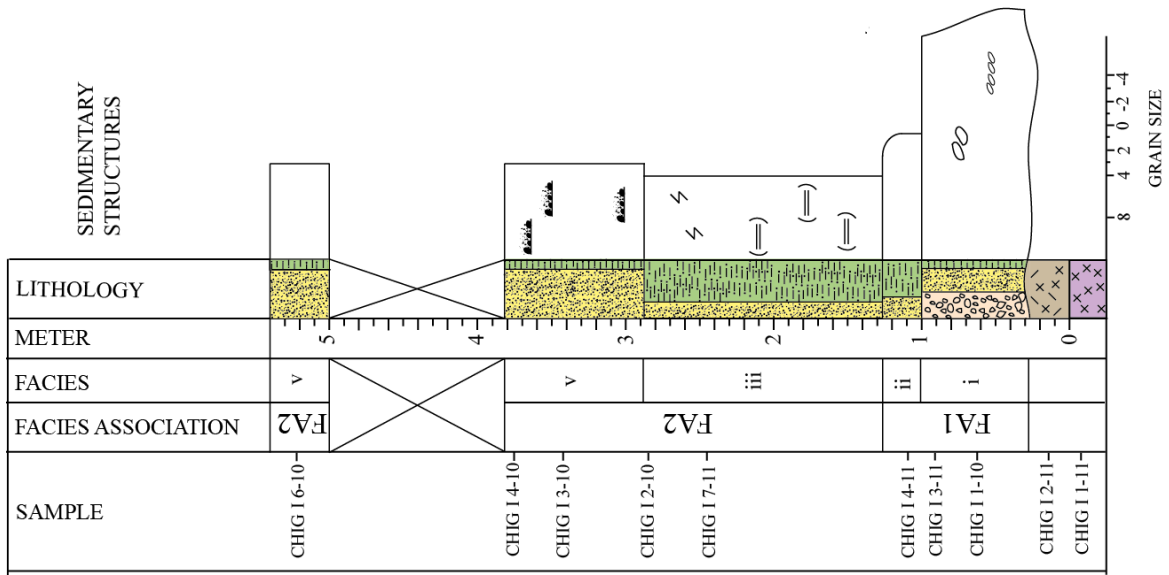


Figure 4.1 View of the dried riverbed. Logged sections. Photo by Dypvik (2010).



Figure 4.2 The exposed riverbed, mainly containing coarse sediments.

Figure 4.2 (Next page) Sedimentological log



LEGEND

- Silt
- Conglomerate
- Sand
- Weathered basement
- Basement
- Imbrication
- Bioturbation
- Parallel lamination
- Possible parallel lamination

Table 4.2 Sedimentary facies in the two CHIG-profiles

Facies nr.	Facies	Grain size	Physical appearance	CHIG I Samples	CHIG II Samples
<i>i</i>	Matrix supported conglomerate	Granule to pebble	Sub-rounded grains, average clast size ~20 mm. Coarse sand to silt matrix. Well cemented by silica. Some grains show imbrication.	1-10, 3-11	3-11, 1-10, 4-10, 2-10, 5-11
<i>ii</i>	Siltstone	Clay to silt	Brownish gray colour, poorly sorted, medium cemented by silica.	4-11	...
<i>iii</i>	Weak horizontally bedded sandy siltstone	Silt to very fine sand	Light gray colour, poorly cemented and highly porous. Weak indications for horizontal bedding. Possible bioturbation marks in the upper parts.	6-11, 7-11, 2-10	...
<i>iv</i>	Upwards coarsening silty sandstone to coarse sandstone	Silt to coarse sand	Upwards coarsening, light gray colour. Poorly sorted, angular grains, moderately silica cemented. Clast concentration is high in some parts.	...	6-11
<i>v</i>	Sandstone	Fine sand	Brownish gray colour, poorly cements and porous. Clast concentration is high in some parts.	3-10, 4-10, 6-10	...
<i>vi</i>	Sandy siltstone	Very fine sand	Brownish gray colour, poorly cements and porous. Clast concentration is high in some parts.	...	7-11, 3-10, 8-11

CHIG I

- i. Matrix supported conglomerate:** this facies consist of a 70 cm thick matrix supported, poorly sorted conglomerate, which lay unevenly upon the weathered basement. Average clast size is 2 cm, but sizes up to 20-30 cm are common. Rounding of grains vary from angular to semi-rounded. Many of the bigger grains had lesser rounding than smaller ones and vice versa.
- ii. Siltstone:** a 20 cm thick unit which lay above (*i*), the upper part showed a minor upwards-fining trend from fine to very fine sand. Poorly sorted, no sedimentary structures.
- iii. Weakly horizontal bedded sandy siltstone:** Almost two-meter high semi-bedded unit of very fine-grained sand follows. The individual beds are of 20-40 cm size, and some of the thin beds show vaguely fining-upwards sequences. Bedding was parallel. Possible bioturbation tracks, 2 mm long, were found and were completely silicified.

- iv. Sandstone:** This facies is situated on top of (iii), between 2.95 to 3.80 meter, and 5 to 5.20 meter. The gap between is covered by sand and gravel, and no rocks were exposed. The unit situated below the cover has some areas with increased clast concentration, but this has not been observed in the uppermost unit. This facies consists of a poorly sorted fine sand unit with little silt content

CHIG I

- i. Matrix supported conglomerate**
- ii. Siltstone:** Situated between two conglomeratic units (i) as a 30 sm thick bed. Fining upwards from fine sand to very fine sand. Poorly sorted, medium silica cemented. No sedimentary structures.
- iii. Upwards coarsening silty sandstone to coarse sandstone:** situated between 1.4 to 2.4 meters above basement. Coarsening upwards, from fine sand to very coarse sand. Weak horizontal bedding at some levels. Concentration of clasts in the coarse sandy parts.

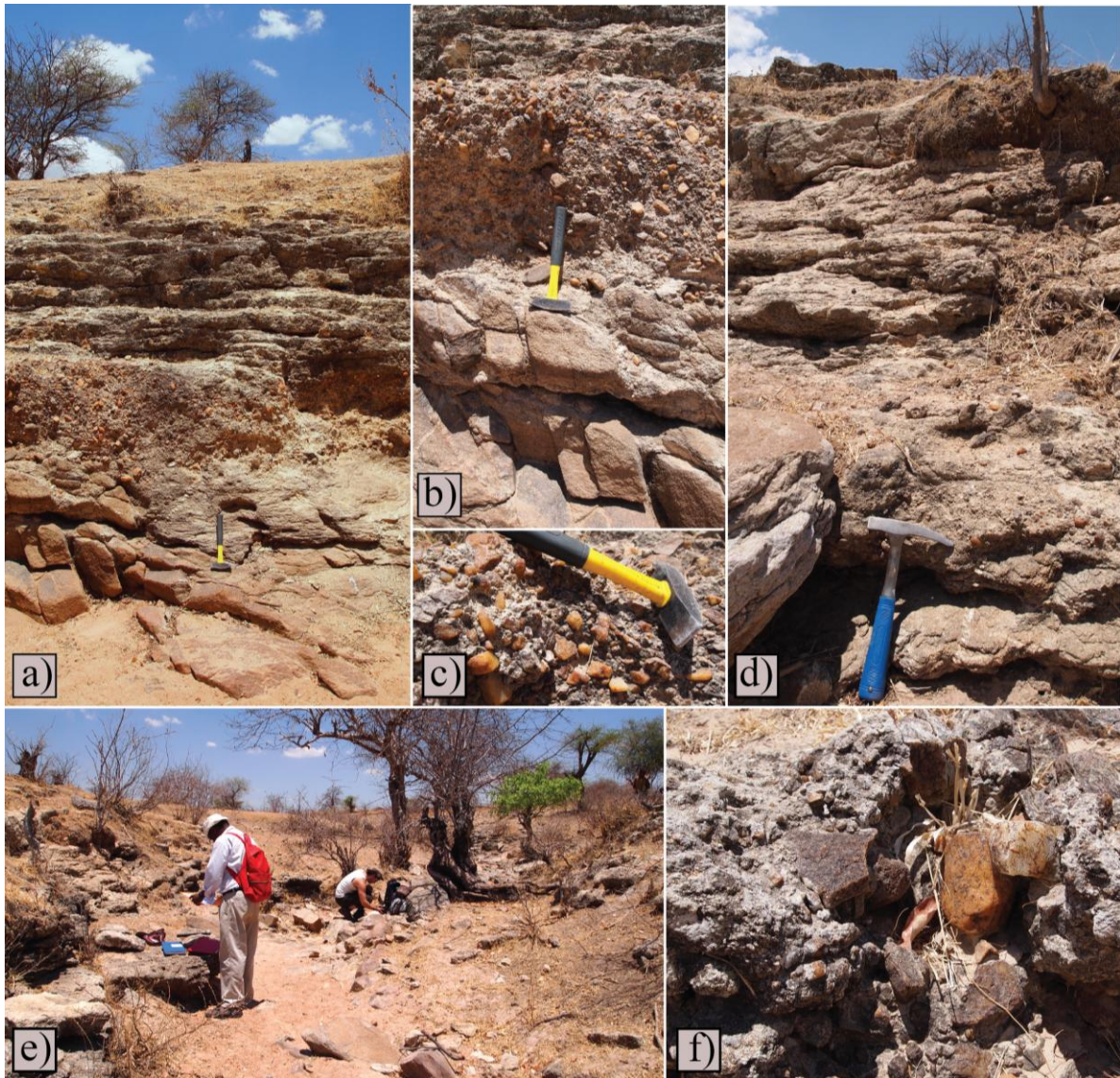


Figure 4.4 a) the CHIG I profile. b) infilling of sediments in the fractured basement. c) Close-up of the basal conglomerate, containing abundant quartz clasts. d) CHIG II profile. e) overview of the river bed. f) Rock fragments and abundant quartz in the basal conglomerate in CHIG II.

Thin section and SEM analysis

CHIG I and CHIG II samples display similar characteristics in mineralogical composition, grain size and shape, sorting, and porosity. Additionally, all samples contain abundant illuviation structures. Here, the results from thin section analysis will only be presented briefly, see Appendix x for more details.

Two photomontages are presented in Figure 3.24 and 3.25 of CHIG I, and CHIG II samples, respectively.

All samples are poorly sorted, and the average grain shape is angular to sub-angular. Most samples are matrix supported, contains little matrix. Porosity varies from between 20 to 60 %. Rock fragments are abundant and normally constitute the ten biggest grains in each thin section. Feldspars are poorly preserved in rock fragments, and most of them have been seriticized. Illuviation structures are found in every sample, and occur in vast numbers. Some samples have found to contain brown biotite and chlorite fragments.

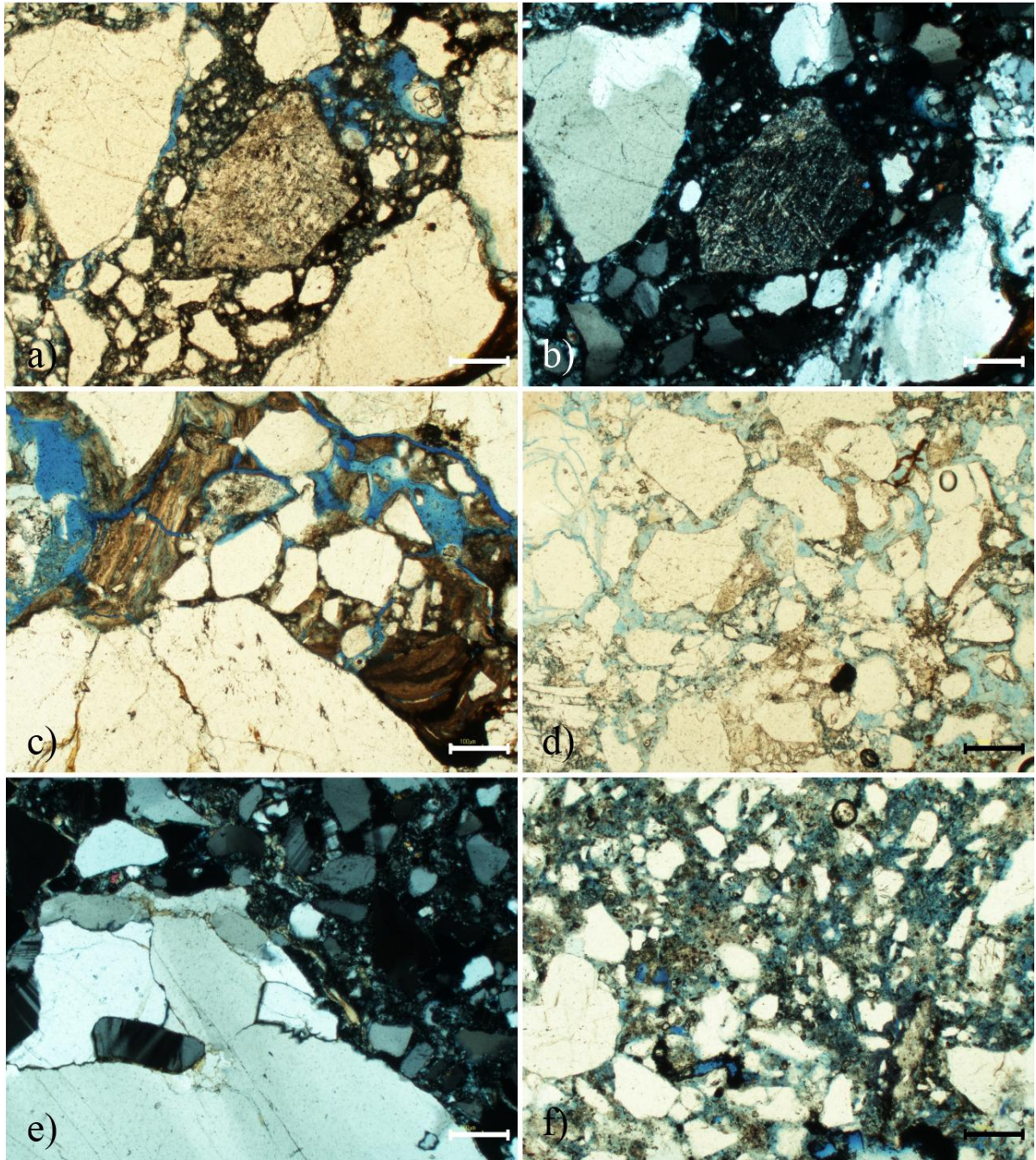


Figure 3.24 Thin section photos of selected CHIG I samples. Scale bar = 200 μm . a) Ppl view of the basal conglomerate (CHIG I 1-10) displaying two types of polycrystalline quartz grains (pegmatitic and granitic) together with a seritized feldspar grain, and smaller grains of quartz b) Xpl view of a). c) Brown clay illuviation in CHIG I 1-10 d) The highly porous and poorly sorted CHIG I 3-10 sample of the sandstone facies (v). e) Large rock fragment in sample CHIG I 4-10 together with smaller, angular quartz and feldspar grains. The sample displays denser grain packing than CHIG I 3-10 (sampled 80 cm below). f) Sample CHIG I 6-10 (uppermost unit in the CHIG I profile).

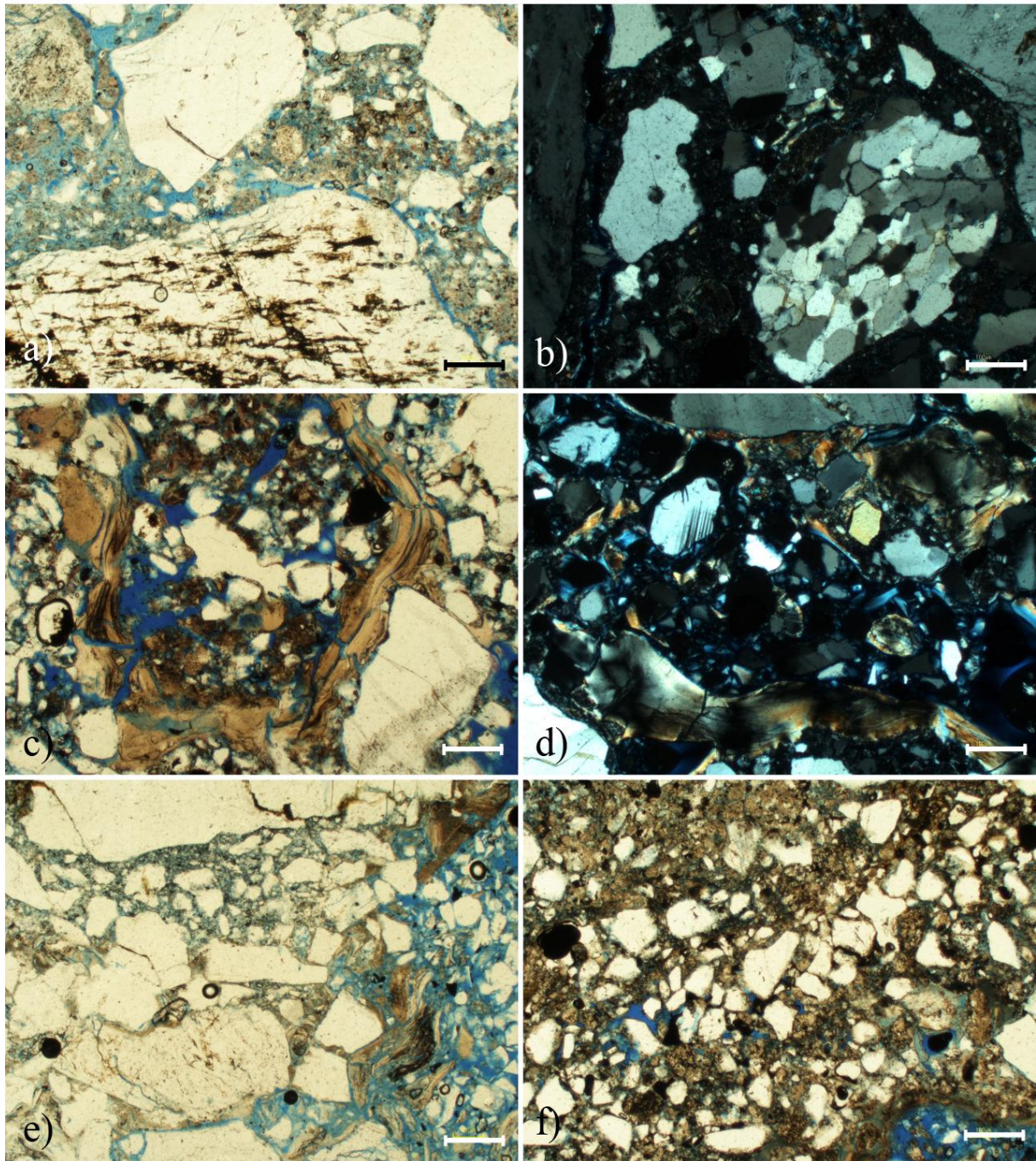


Figure 3.25 Thin section photos of selected CHIG II samples. Scale bar = 200 μm . The basal conglomerate, CHIG II 1-10, contain various grain with varying preservation as seen in a), where poorly preserved feldspar is found together with quartz and rock fragments of various sizes. b) Sub-rounded polycrystalline quartz grain together with larger rock fragments and smaller quartz grains in sample CHIG II 1-10. c) and d) Clay illuviations in the upper most conglomeratic layer in sample CHIG II 3-10, e) The poorly sorted CHIG II

3-10 sample from the sandy siltstone facies (vi), displaying great variations in grain sizes. Detrital brown biotite fragments are scattered around in the sample and are often found as illuviations. f) Sample CHIG II 6-11, collected from the upwards coarsening silty sandstone facies (iv).

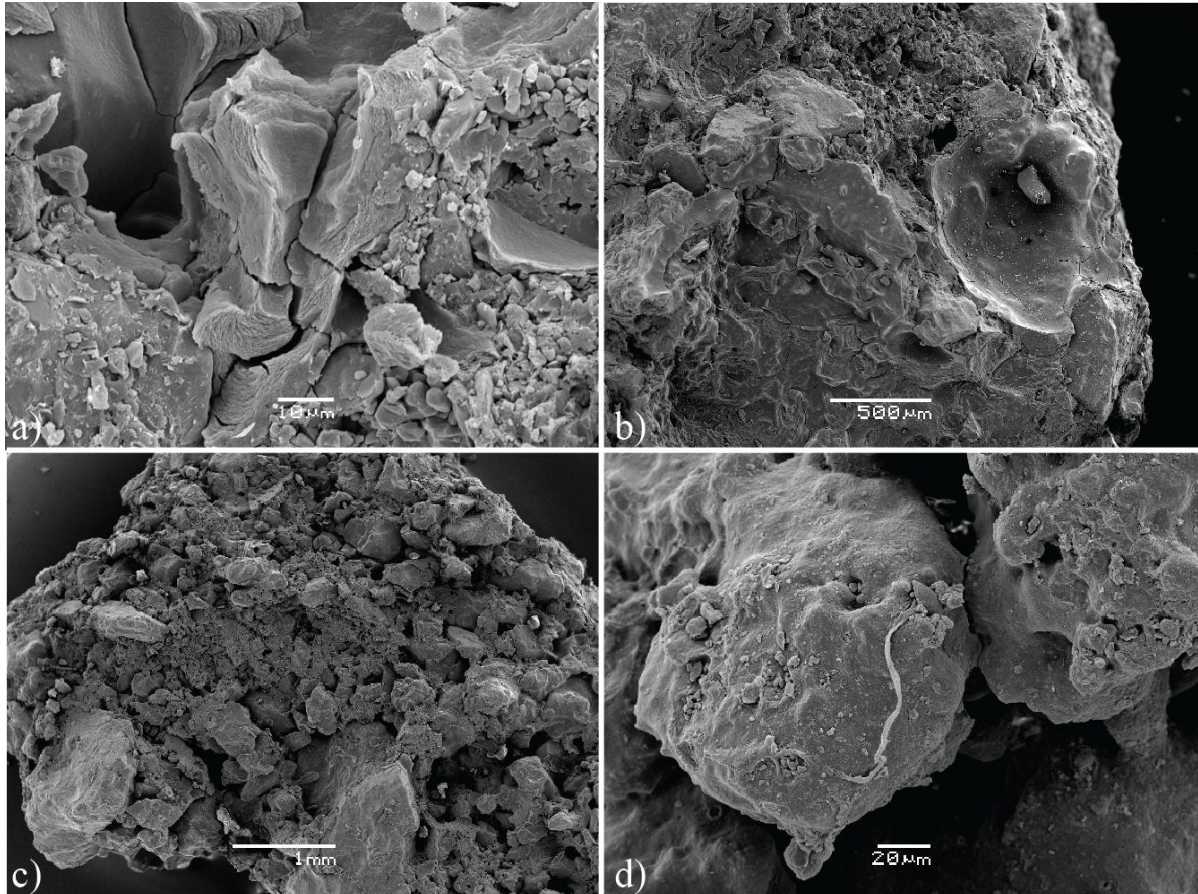


Figure 3.26 SEM (SEI) images of selected samples displaying the crumbly texture typical for CHIG II & I. a) Clay illuviations of Al and Si in CHIG I 1-10 b) Coatings of aluminum and silicon where a detrital grain of sand, CHIG II 2-10 c) Image of CHIG II 3-10, displaying the typical appearance for the Chiguluka-samples. This porous sample is not very well cemented, and has better sorting than the other samples analyzed. d) Detrital mineral grains, coated, and cemented together by a mix of aluminum and silicon, in CHIG I 6-10.

XRD Results

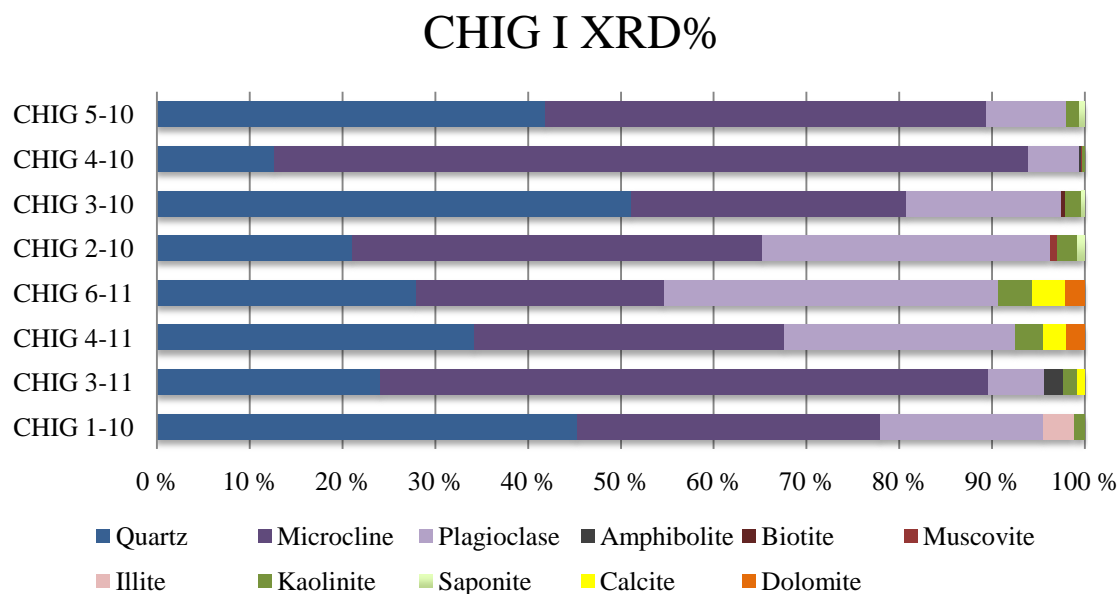


Figure 3.27 results from the XRD analysis of CHIG I samples.

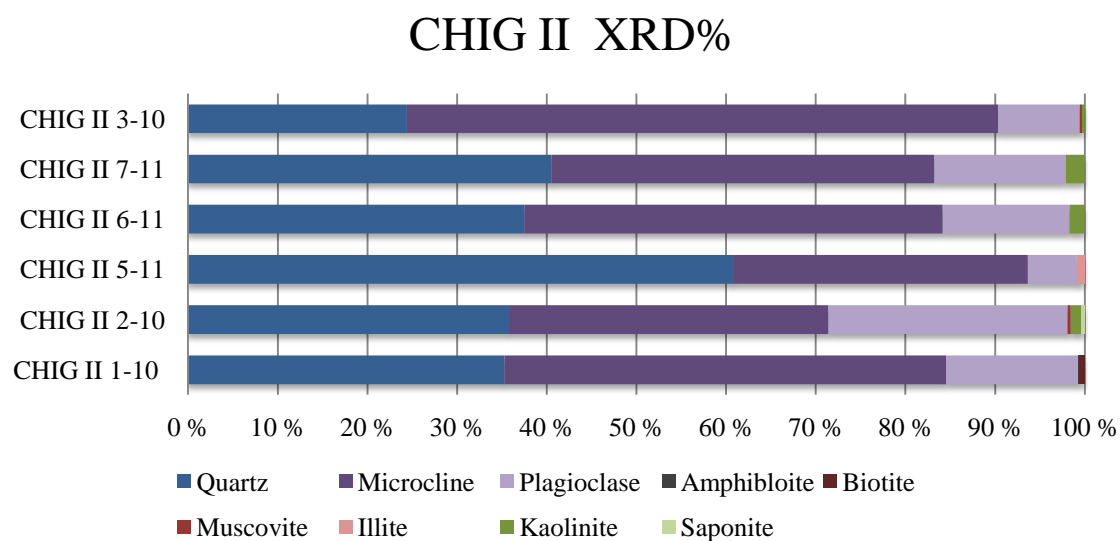


Figure 3.28 results from the XRD analysis of the CHIG II samples.

The CHIG samples have a simple composition compared to SARP, mainly consisting of quartz, microcline, plagioclase, and some clay minerals. The samples are rich in feldspars and the majority of the samples are dominated by i

CHIG I samples contain abundant feldspars, microcline make up the biggest part of the total feldspar content in these samples. Quartz is the second most abundant mineral present, between 13 and 45 XRD%.

FA1: Samples 1-10, and 3-11: Display an upwards decrease in quartz, and plagioclase, while the content of microcline increases. Kaolinite is found in both samples, and exist together with illite in the lowermost samples (CHIG I 1-10). Amphibolite has been detected in CHIG I 3-11 (2 XRD%).

FA2: one sample (CHIG I 4-11) represents the siltstone facies (*ii*) laying on top of the basal conglomerate. Richer in feldspars than quartz, and contain 2.5 XRD% calcite, and 2XRD% dolomite in addition to kaolinite.

Two samples (CHIG I 6-11 and CHIG I 2-10) represents the weak horizontally bedded sandy siltstone facies (*iii*), which show an upwards decrease in quartz, and increase in both plagioclase and microcline. Both have been found to contain kaolinite, CHIG I 2-10 have also been found to contain smaller amounts of muscovite (0.8 XRD%).

Three samples (CHIG I 3-10, CHIG I 4-10, CHIG I 5-10) represent the uppermost sandstone facies (*v*). CHIG I 3-10 and CHIG I 5-10 have a similar mineralogical composition, however biotite have been recorded in CHIG I 3-10. CHIG I 4-10 contains high amounts of microcline (48 XRD%) compared to the other two samples

CHIG II

FA1: Three samples (CHIG II 1-10 and CHIG II 2-10, and CHIG II 5-11) represents matrix supported conglomerate facies (*i*). The basal conglomerate CHIG II 1-10 is dominated by feldspars (49 XRD% microcline and 15 XRD% plagioclase), contain 35 XRD% quartz, and minor amounts of biotite and amphibolite. CHIG II 2-10 and CHIG II 5-11 from the upper conglomerate layer show an upwards increase in quartz, and decrease in both feldspar species. Biotite and kaolinite is found in the lower sample, while illite is found in the upper sample.

FA2: CHIG II 6-11 (upwards coarsening silty sandstone facies, *iv*) is dominated by feldspars, and contains 35 XRD% quartz, and minor amounts of kaolinite.

The uppermost sandy siltstone facies (*vi*) is represented with two samples (CHIG II 7-11 and CHIG II 3-10). The two samples display and upwards decrease in quartz while microcline increases. CHIG II 3-10 is the samples which contain the highest portion of microcline in all CHIG samples (66 XRD%).

5 Discussion

5.1 Depositional environment

The lowermost facies association (FA1) consists of a matrix supported conglomerate facies (*i*), a greenish gray siliceous sandy siltstone facies (*ii*), and a greenish gray siliceous claystone facies (*iii*). The matrix supported conglomerate (*i*) lies unconformably upon weathered Archean granite, and is characterized by having angular grains floating in a fine-grained matrix. The angularity of the clasts appear to be independent of grain size since bigger grains can be seen as both angular or sub-rounded. The degree of rounding is a function of grain size, composition of the grain, type of transport process, and distance of transport (Boggs, 2006). The variations in rounding indicate that some grains have been subjected to more transport than others. These deposits lack both internal bedding and clast imbrications, and the random orientation of the clasts, suggest deposition from cohesive debris flows (Collinson, 1996).

The greenish gray siliceous sandy siltstone facies (*ii*) is matrix dominated, containing poorly sorted deposits, and have few framework grains. Deposits have a high clay and fine silt content, indicating that they were deposited in a low-energy environment from suspension (Collinson, 1996). Furthermore, no sedimentary structures have been found in deposits belonging to this facies, which can indicate rapid deposition. The lack of laminated bedding indicates continuous deposition from suspension, with little or no fluctuations in depositional conditions, and sediments composition (Boggs, 2006). The deposits are characterized as having a greenish gray colour. Most of the samples from FA1 display low Th/U ratios and higher Cr and Ni concentrations. According to Dypvik *et al.* (2006), this can indicate hypoxic to anoxic bottom conditions assuming that the sediment source rock and diagenetic conditions did not change within the section. However, there is only one sample (SARP 5-11) present that strongly indicates hypoxia/anoxia. The idea of low oxygen conditions is strengthened by the absence of bioturbation tracks and fossils in all beds of FA1.

Desiccation cracks, raindrop prints, and red staining from oxidized iron have not been observed in any layers, indicating that these sediments have not been exposed subaerially after deposition. The author believes that the sediments accumulated in a small, possibly balanced, lake. If it was a hydrologically closed lake we would expect to find evidence of

seasonal variations in the deposits since the lake may have experienced considerable fluctuations in water levels due to seasonal flooding (Potter *et al.*, 2005). During the dry-season, the lake would most likely dry up due to high evaporation rates, leaving the lakebed subaerially exposed. Evaporites are often associated with closed lakes, which have evaporation rates that exceed the total inflow of water into the lake (Talbot and Allen, 1996; Potter *et al.*, 2005; Boggs, 2006). It is probable that this lake was continuously fed by groundwater. As groundwater seeps into the lake, the more saline water will mix with meteoric water and reduce salinity. Evaporites have not been found in any samples, thus strengthening this theory of a groundwater fed lake.

As previously mentioned, the contact between FA1 and FA2 was not observed, and it is not known whether the contact was erosional or not. Above lies an upwards coarsening silty sandstone unit. The shift from fine silt and clay to in FA1 to fine to medium sand in FA2 can reflect an increase in the competence of the fluvial regime (Rust, 1981), allowing fluvial transport of coarser particles to the depositional site. The sandy siltstone (*iv*) situated above the upwards coarsening silty sandstone could represent sedimentation in river channel. Three sandy siltstone beds have been deposited above and have been interpreted to be deposited by rapid and frequent channel avulsion.

The individual beds are between 1 to 1,5 m thick, mostly about 1 m thick. The basal surfaces are planar. Parallel bedding is seen in the more sandy upper two meters of this unit. The beds appear massive, which suggest very rapid deposition (Tunbridge, 1984).

Channelized debris flows are associated with distinct levees and terminate in lobate deposits. The base of the Saranda profile has two conglomeratic units, separated by fine sand deposits, in the basal part of the section. The first unit is situated uncomfortably on weathered Archean granite. The conglomerates have been interpreted to have been deposited from a cohesive debris flow deposits with high content of fine-grained matrix. Clasts are normally no larger than a few centimeters and can have travelled some distance from the source area. The sandy siltstones have been interpreted to be fine-grained sedimentation from suspension in a semi-permanent lake, transported by rivers.

The depositional conditions of the Kilimatinde Cement were highly influenced by tectonic activity operating in the area the time of deposition. Normal faulting causing uplift of the Chenene Hills would have produced large alluvial fans downslope from the Sanzawa fault scarp. Tectonic activity affects slopes of the rivers and floodplain, and their supply of water and sediments (Bridge, 2006). During heavy rain, huge areas of the highland would be drained, and sediments and water would be transported down slope and over the fan and eventually spread out over the huge areas on the basin floor. River channels are commonly braided if there is a large supply of water from the hinterland (Bridge, 2006). Normally, not all channels are active at the same time, and channel avulsion is a common feature during flooding. Channels normally decrease in size down-fan due to water infiltrates or may become a sheet flood. Networks of extensive ephemeral streams could have carried sandy sediments over distances of tens and hundreds of kilometers (Tunbridge, 1984), spreading the sediments across the basin floor, and possibly terminating in muddy floodplains, perennial lakes and play lakes.

5.2 Mineralogical composition

Based on the XRD analysis (Fig.3.13), the different mineral assemblages can be used as a base for SARP section subdivision. The Saranda profile can be subdivided into three units based on the mineralogical composition: lower-, middle-, and upper sections. These units are coterminous with the three facies associations FA1, FA3, and FA3.

Common textural features of SARP samples:

- Poor sorting
- Extensive variations in grain sizes
- Majority of the clastic grains are subangular
- High matrix content

Based on mineral composition and texture, all samples can be classified as immature according to Folk (1951).

5.2.1 *Lower section: Level 1 – 6m.*

The mineralogy of the lower unit of the Saranda profile is more complex than the two overlying horizons. The mineralogical content can vary greatly from one sample to another.

Two phases of K-spar (microcline and orthoclase) are present with plagioclase and various amounts of quartz. From the XRD analysis, most samples from the lower section have a feldspar contents which exceeds the amount of quartz. Point counting (Appendix B) of the same samples illustrates that the most common detrital grains are in fact quartz, which exceed the number of feldspar grains. It is most likely that the amount of feldspar is not only from the coarse fraction, but may make up a large part of the matrix component in these rocks. This is supported by SEM and EMP analysis of the matrix. Several samples from the lower unit display matrices composed of small authigenic K-spar crystals together with opaline silica, various clay minerals, and apatite.

Apatite is a major constituent in the SARP 5-11 sample (26 XRD%), and is also present in SARP 5-10 and SARP 3-10 (Fig. 3.13). SEM and electron microprobe analysis reveal that this is authigenic apatite and incorporated in the matrix together with opaline silica and authigenic K-spar. SARP 5-10 and SARP 5-11 are additionally the two samples with highest uranium content. SARP 5-11 is also associated with high concentrations of REE (Table 3.5). Knivslund (2012) has studied the composition of the groundwater in the Saranda area and found that the water is currently oversaturated for fluorapatite.

5.2.2 *Middle section: Level 8 – 16 m.*

Kaolinite is first introduced in the middle section, while plagioclase and orthoclase are absent in all samples (Fig. 3.13). Furthermore, the amount of K-spar has also been drastically reduced when compared to the lower unit, as illustrated. The removal of plagioclase could indicate more intense weathering, or different source rock composition (Cullers, 2000). Plagioclase weathers more readily than K-spar (Nesbitt and Young, 1989). This is supported by point counting data (Appendix B), since plagioclase grains usually display lower preservation than K-spar grains in the SARP samples. Weathering of plagioclase can produce minerals belonging to the kaolinite group (Nesbitt and Young, 1989; Cullers, 2000;

White *et al.*, 2001). Since kaolinite is first introduced in the middle section where plagioclase is absent, this could reflect a plagioclase alteration to kaolinite. SARP 8-10 contains the highest amount of kaolinite in the SARP-samples (Fig.3.13), and is also the sample with the lowest amount of K-spar. When feldspar minerals dissolve, kaolinite precipitates from the pore fluids (Bjørlykke, 2010). The reaction is as follows:



Furthermore, the trace element analysis (Appendix D) reveals that potassium concentrations have decrease in the middle and upper sections (where kaolinite is first introduced) compared to the kaolinite-free lower section. In fact, the two samples containing the highest amount of kaolinite are also the two samples with the lowest percentage of potassium.

5.2.3 Upper section: Level 16- 24.5 m

The mineralogical composition of the upper section is similar to the middle section, except for the absence of opal (**Fig.3.x**). XRD analysis reveals that this is the section contain the highest amount of quartz, (between 80 and 90 XRD%). However, from point counting, this section contains fewer detrital quartz grains than the middle section (Appendix B). It is important to keep in mind that the XRD% are just an estimate, but it can be assumed that the quartz content can be even higher since the second most intense reflection has been used instead of the 3.34Å reflection. Most likely, the large amount of quartz in these samples reflects a fine grained matrix quartz, since it only makes up 40 to 58 % of the thin section. This assumption is strengthened by SEM and thin section analysis, where quartz is found as the main cementing agent in these rocks. The silicification of this section will be discussed later.

The higher quartz / total feldspar ratio in FA2 and FA3 might suggest more intense weathering (Cullers, 2000).

5.3 Nodule formation

The upper unit of the Saranda profile has a similar mineralogical composition as the unit below (**Fig.4.x**), but is quite different in appearance (**Fig. 3.6**). The surfaces of these rocks are entirely covered with rounded nodules with irregular surfaces. Investigations of thin sections and hand samples reveal that these nodules also exist on the inside of these rocks, and are therefore not just a surface phenomenon.

Brewer (1964) defined a *gleabule* as “a pedological term for a concretionary or nodular structure which encloses greater amounts of certain constituents, or has a different fabric, or a distinct boundary with the surrounding matrix”. This term will be used henceforth when addressing these nodular features. The term *nodular* will be used when addressing the weathering surface of these deposits.

5.3.1 Formation of concentric coatings on individual grains

The growth of the concentric pisolith-like structures is through the accretion of new material around a nucleus (detrital grain). How materials accrete onto a clastic grain is best illustrated by studying how the laminations enclose an angular clastic grain. Figure 5.1 is a sketch of a concretion in sample SARP 14-10. Here, a polycrystalline quartz grain is the nuclei from which fine grained material has accreted around. Well developed nodules are always well rounded, and Figure 5.1 illustrates how this form is attained. First, lamina is developed on the most irregular surfaces by mineral accretion. Depending upon the irregularities on the nuclei, several sets of lamina may be necessary to achieve an even, regular contour. This is achieved by accretion from one outer point to another. When all points have been connected by a final set of lamina, and a regular surface has been attained, accretion of new material can accumulate around the entire nodule. This is making the nodule more rounded illustrated by gray-scale

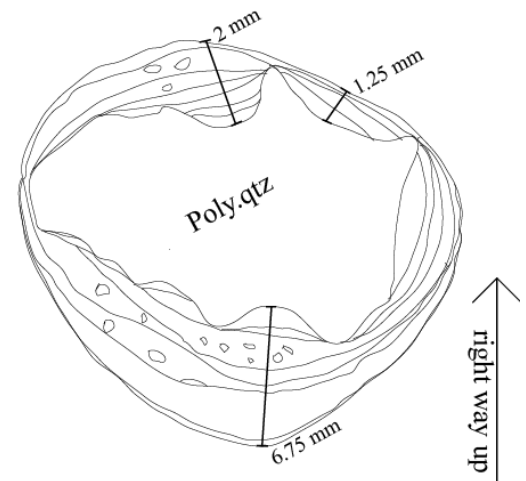


Figure 5.1 Sketch showing how clastic grain acts as a nuclei from which material accrete around. Lamina is first developed on the most irregular surfaces. First when a regular surface is attained, continuous lamina sets can develop around the structure. Example from SARP 14-10

colour in the sketch. Smaller clastic grains may or may not be incorporated in the thicker lamina sets, as illustrated. New material continues to accumulate around the nodule. On well-developed concretions, the thickness tends to be many times greater on the lower grain surface than at the top. In this example (Fig.5.1), the thickness is over three times greater on the lower surface than what it is at the top.

The majority of mineral grains in the nodular unit do not exhibit as many well developed concretions, as the example in Figure 5.1. Most of them only have a few very thin rims of clay around the grain. However, the clay on these grains has been formed in the way described above, with the most irregular surfaces filled first. The concentrically layered coatings can be a result of clay and silt accretion onto a nucleus in a free-rolling environment (Fig.4.2). Wind can transport sand-sized particles along the surface by the process of saltation (Kocurek, 1996). If these grains are moist, they can accumulate finer material when they hit the ground. If the energy is high enough, they will bounce back into the flow, and the sequence is repeated. Continuation of this process will eventually produce several layers of accreted clay and silt.

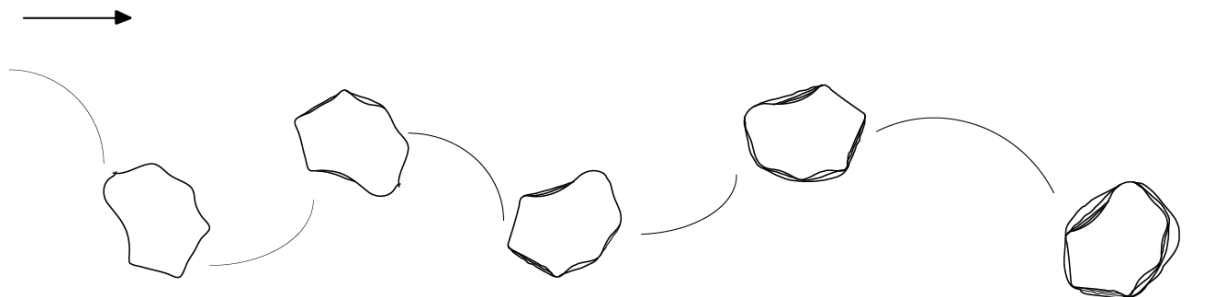


Figure 5.2 Formation of clay coatings by accretion of clay and silt to a saltating, moist mineral grain. The arrow illustrates the wind direction.

This can explain the variations in grain coating in these deposits. Some grains may not have been subjected to this process, and hence may not have coatings. Other grains may have been transported by saltation, and have developed clay coatings. The degree of coating can be an indicator of how long they have been subjected to this process.

5.3.2 Formation of glaebules

The concretions described above are often too small to be visible in hand specimens. The glaebules observed in the field and in hand samples are between one to three centimeters, and consist of numerous individual concretions together with regular clastic grains



Figure 5.3 Simplified sketch of the SARP 11-10 sample, illustrating the colour variations within the glaebules and the matrix. Reddish colour contain abundant oxygenized iron, the bleached areas are rich in Al, and low in Fe.

incorporated by thick lamina sets of silica and kaolinite as seen in Figure 3.12. Smaller grains can be incorporated between two concentrically banded zones (Fig.5.3). Towards the top of the profile, concretions commonly grow together to form larger, often asymmetrical, concretions, and can contain several smaller concretions cemented to detrital grains. The glaebules have a denser grain packing than the surrounding matrix from which the final material accumulates around. Poorly developed glaebules are usually highly porous and contain little matrix, while the well-developed glaebules have established matrix in the interior of the glaebule.

The concentric layers appear as different colours and represent different minerals, alternating between dark brown and light yellow laminas, although several layers of the same material can accumulate before a different type of cement is presented. Reddish stains from oxidized iron can also be found incorporated between lamina sets, and in the matrix. The compositions of the rims are mainly $AlSiO$, where the concentrations of aluminium and oxygen vary between the layers. The lighter coloured laminations are commonly richer in aluminium than the dark brown laminas. Brownish-red mottles are spread around in these deposits, which are probably a result of pedogenic activity formed by migration and accumulation of Fe and Al oxides in the kaolinitic matrix or voids (Anand and Paine, 2002). Some of the kaolinite might be secondary, filling voids and/or the interior of the nodules.

Most of the glaebules investigated under the microscope display a thicker coating at the lower grain surface than at the top, which is a common feature for nodular calcretes (Goudie, 1983). Goudie (1983) explains that this is a gravitational type of cement commonly found in the vadose environment, and is result of hydration and dehydration. When the water has been drained from the pores after rainfall has ceased, a thicker film of water is concentrated at the lower surface of the structure, and lies in the direction of the gravity vector. As a result, minerals will precipitate and cement the nodule (Goudie ,1983).

The glaebular structures have most likely been formed by *in situ* precipitation of new material in a relatively static environment. A possible course of events can be as followed:

- 1) During rainfall, grains are concentrated to other areas by the moving of fluids through pores in the sediment towards areas where the fluid energy is too low for further movement. Finer particles may be washed downwards and accumulate on larger grains. Finer grains may be cemented to larger ones by the precipitation of silica.
- 2) Water is eventually drained out from the pores after rainfall has ceased, leaving a thicker film of water retained at the lower surfaces of the grain clusters.
- 3) Accretionary growth of new minerals occurs on individual grain surfaces, and/or precipitates around clusters of mineral grains.
- 4) A new period of rainfall, filling pores with fresh meteoric water. Downstream movement of water continues to displace detrital grains to areas of lower energy. The composition of the water will change as it percolates through the sediments, and will determine which minerals will be precipitated.
- 5) Dehydration of the sediments after heavy rain, retaining a new film of water at the lower surfaces of grains and grain clusters will cause new minerals to precipitate.
- 6) Matrix minerals will eventually start precipitating within the developing glaebules.
- 7) Continuation of hydration/dehydration and precipitation of new materials will eventually form densely packed glaebules with well established lamina sets. The interior of the glaebules are cemented together. New minerals continue of precipitate on the outer surface of the glaebules, further cementing it together, making them more resistant to weathering.

- 8) As glaebules continue to grow, primary sedimentary structures and fabrics will be disturbed, and eventually no longer be recognizable.

5.3.3 Development of the nodular surface

After the sediments were lithified and exposed at the ground, they started to develop a nodular surface structure (Figs.5.4). The internal glaebules have several sets of lamina around the structure formed by multiple stages of *in situ* precipitation of new minerals, making it harder to weather. From investigation of hand-samples, the matrix surrounding the glaebules seems to weather more easily than the glaebules. And as the matrix weathers out, the more resistant glaebules remain, resulting in a nodular, bumpy surface (Fig.5.4).

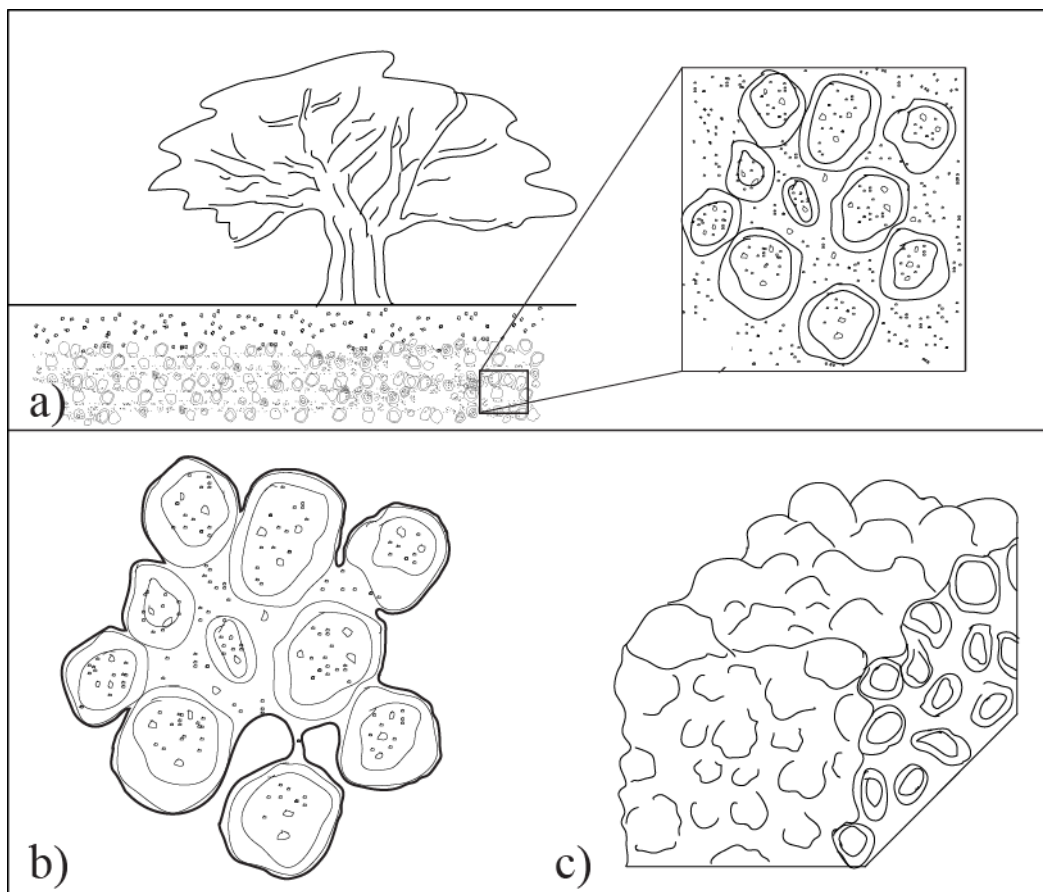


Figure 5.4 Cartoon illustrating the formation of the nodular surface. a) Glaebules and the matrix are protected from weathering by overlying deposits. b) When exposed at the surface, matrix will start to weather out, while the more resistant glaebules remains. c) The removal of the matrix results in an irregular, nodular surface, as illustrated in the cross-section.

- Nodules formed *in situ* when the sediments were still unconsolidated. Each nodule is composed of clusters of clastic grains. Some grains have concentric coatings of fine
After extensive research on these occurrences, no data or published literature was found. Similar structures have been described in nodular calcretes from northern Tanzania (Hay and Reeder, 1978), and other calcretes (Goudie, 1983). However, the mineralogical composition is very different from what is found in calcretes which are mainly composed of calcite. Since there is no explanation for this in the literature, as far as the author knows, it may be possible that this is an undescribed finding.

5.4 Silification

A common feature for samples collected from the Saranda profile are that they are all well-cemented by silica. Silica can precipitate directly as authigenic phases from silica-rich pore solutions. Furthermore, silica species may transform by dissolution and recrystallization into other silica species over time (Williams *et al.*, 1985a). Gradually, the most soluble silica species within the host rock will transform in a step-wise manner until the most stable polymorph has been formed, (Nash and Hopkins, 2004). The sequence of formation is determined by a range of processes, which influence the degree of supersaturation, complexation of silica, absorption by clays, and the neoformation of clays and other silicates (Williams *et al.*, 1985). The silica species present in the Saranda profile will be discussed in the forthcoming section, presented in order of stability from lowest to highest.

Opal occurring as brown, diffuse clouds is a very common opal species that occurs in high abundances in the lower facies association. It is also associated with FA2 but is less abundant. This type is believed to be formed mainly from the transformation or replacement of clay minerals (Thiry and Milnes, 1990). The same authors (1987) argue that alumina is more soluble than silica in acidic conditions, and the major cations are leached from the clay structures while Si remains, forming opal-A. Thiry *et al.* (2006) states that opal-A can be difficult to detect in XRD-recordings if opal-CT is present. If the two phases are present within the same sample, the broad and diffuse opal-A reflection will be camouflaged by the stronger opal-CT reflection, and Thiry *et al.* (2006) argue that it cannot be stated that the recording is exclusively of opal-CT.

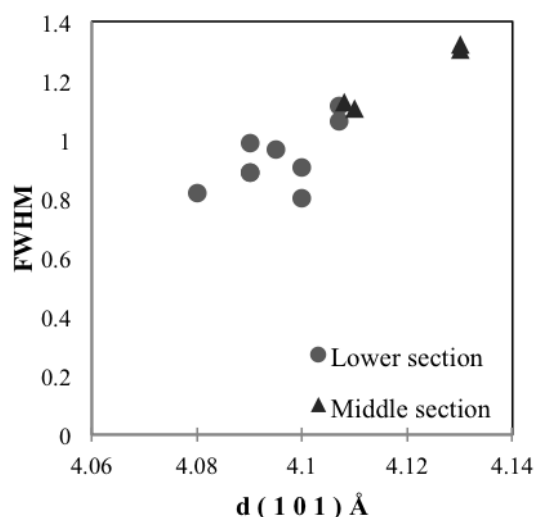


Figure 5.5 Plot of peak width at half height vs. the position of the main peak, displaying the decreasing crystal stability upwards from the lower to middle section

Data from XRD and SEM analysis reveal the complexity of the different opal forms present in the Saranda profile. An attempt to classify the different opaline species from XRD analysis is given in Table 3.4. Additionally, the d -value of XRD analysis can be used as an indicator of structural disorder since the value increases with increasing structural disorder (Williams *et al.*, 1985a, b; Eleza *et al.*, 1994; Smith, 1997).

All opals from the Saranda profile are classified as opal-CT. The most common d -spacing in the SARP samples are 4.11 Å, and Ghisoli *et al.* (2010) argues this d value is the ideal d_{Tryd} , indicating that all the tridymite is

present in the monoclinic low-temperature phase. The lowest value is recorded in the SARP 2-11 sample (4.08 Å), and is therefore the sample with highest structural order.

Eleza *et al.* (1994) found that the degree of ordering in opals can be studied by looking at the width at half height (ΔH) vs. the position of the main peak. The value seems to increase with structural disorder. By applying this method to the silcretes in the Saranda profile, a trend can be followed from the lower section to the middle section (Fig.5.5)

In general, the opals from the lower section display a more ordered crystal structure than opals from the middle section, with an average d -spacing of 4.09 - 4.10 Å. Two samples have also been found together with the tridymite shoulder indicating more ordered opals. Low ΔH also indicates more structural order (Eleza *et al.*, 1994). In the middle section, (Fig.5.5) the ΔH value is higher than one, and this combined with high d -spacing suggests a more disordered crystal structure. The uppermost sample containing opal, SARP 10-10, has the highest recorded d -value (4.12 Å), and is the sample with the lowest ordered opal-CT.

The plot in **Figure 4.4** displays a linear trend where the structural disorder increases upwards in the profile. There may be two explanations for this: 1) the sediments have been flushed by

two different pore fluids of different characteristics, or 2) the degree of ordering is increasing with the age of the deposit (Eleza *et al.*, 1994). Williams *et al.* (1985) states that the *d*-spacing in opal-CT decreases with depth/age, and as opal ages geologically, it de-waters and transforms to chalcedony and quartz (Smith, 1997).

Investigations by SEM reveal that opal-CTs commonly occur as spherical aggregates (lepispheres) in the SARP samples. A variety of different opal-CT lepispheres are reported, illustrated in Figure 3.17. The most common variant is small (ca. 4 - 5µm in diameter) well-bladed lepispheres, found together in clusters or as individuals together with other mineral grains. These small lepispheres, known as *complete lepispheres* (Flörke *et al.*, 1976), are made up of individual euhedral to subhedral opal-CT blades that penetrate each other at a 70° angle. They also occur along cavity walls as hemispherical clusters in several of the analyzed samples. Further precipitation results in the formation of *composite lepispheres*, which form when the entire pore space has been filled with tightly packed microspheres (Flörke *et al.*, 1976). The four samples (SARP 2-10, SARP 2-11, SARP 5-10 and SARP 9-10) contain this form of opal-CT and have between 3.4 to 8.7 % opaline silica.

The opaline vein (sampled approx. 10 meters above basement in the same unit as SARP 6-10 was sampled) displays different varieties of opal-CT lepispheres in the interior of the vein compared to the outer crust. Figure 3.17 (i-j) illustrates the opal-CT variant found in the interior part of the vein. These opal-CT bladed lepispheres are 7µm to 12µm in diameter, and are the largest lepispheres reported from SARP samples. The situation is different when moving away from the interior and out towards the crust where the average size of the individual lepisphere reaches sizes of approx. 1µm to 2µm, and are less developed and more poorly bladed. These poorly crystallized opal-CT lepispheres found at the outer crust of the silica vein can be a response of absorption of ion impurities on the surface of the crystal, which then can prevent further growth (Thiry and Milnes, 1990). Additionally, Williams *et al.* (1985) points out that precipitation rates, concentration of silica in solution, and the presence of impurities are important factors for the precipitation of opaline silica. Gaillou *et al.* (2008) suggest that the variety of the different structures can be a response to different precipitation rates, and proposed that random piling of individual nanograins is the result of rapid growth rates where the individual grains do not have the time to arrange themselves into a larger structure. Gaillou *et al.* (2008) also suggest that lepisphere formation may be a

result of a slower growth rate. This suggests that precipitation rates were higher at the edges of the vein, where nucleation was first achieved and produced less-developed lepispheres. Nucleation and opal-CT precipitation was less rapid in the interior of the vein, producing large, well-bladed opal-CT lepispheres.

Chalcedony is found in the most silicified samples and represents a more stable form than opal-CT. The chalcedony crystals typically occur in voids or cracks and are most likely the recrystallization of opal (Thiry *et al.*, 2006). Furthermore, they argue that chalcedony precipitated in voids is a response to a more dilute solution containing lower concentrations of cations other than Si. Megaquartz, located in void centers have been precipitated last, when the porosity was lowest and pore water movement at its slowest (Summerfield, 1983).

Quartz overgrowths have not been seen in thin sections, not even in the most silicified samples, though overgrowth by opal has been observed on the electron microprobe (Fig.3.16). A possible explanation of this is given by Webb and Golding (1998), who stated that quartz overgrowth in silcretes is more common in sandy sediments with a low content of clays. The lower section has a very high content of fine silt and clay that could explain the lack of overgrowth by quartz in these samples, and Ullyot *et al.* (1998) state that clay matrix tends to favor the formation of opaline and cryptocrystalline silica. Quartz will only precipitate out of solutions undersaturated with respect to opal-A or opal-CT (Williams and Crerar, 1985), and therefore it can be assumed that the pore solutions flushing the lower and middle units were oversaturated with respect to opal-A and/or opal-CT, prohibiting the formation of authigenic quartz.

Opaline silica is absent in the uppermost facies association, however, the sediments are well silicified by quartz, indicating precipitation from solutions are undersaturated with respect to opal-A or opal-CT. Clay can have a retarding effect in the opal-A to opal-CT transformation, but it has been found that clay appears to enhance opal-CT to quartz reaction (Issacs, 1982; Williams *et al.*, 1985).

Vertical oriented chalcedony veins (Fig.3.4c) have frequently been found to cut the two lower sections (FA1 and FA2), indicating that the deposits were already lithified when the silica saturated solutions flowed through fractures in the rocks. The pure chalcedonic veins have been formed from mobile silica sources (Thiry and Milnes, 1990), are different in

appearance and orientation when compared to the siliceous veins found in FA2 (Fig.3.4). These veins are most likely related to hydrothermal activity associated with later rifting. The near lying Bubu fault (Fig.1.7) has been associated with thermal hot springs and hydrothermal activity (Macheyeki *et al.*, 2008), which could be a possible source.

Summary of the different silicification processes:

- 1) Brown opal matrix results from substitution of former clay matrix in the sediment.
- 2) Opal-A transforms → opal-CT transformation
- 3) Opal-CT precipitation
- 4) Chalcedony vein formation, precipitated from mobile silica sources after FA1 and FA2 were lithified, and probably related to a younger rifting stage.
- 5) Microcrystalline quartz precipitation from solutions undersaturated with respect to opal-A and opal-CT in FA3.

5.5 Silcrete classification

Indication of the environment of silcrete formation and post-formational diagenetic transformation can be obtained by identification of the type of silica species present together with analyses of the silcrete fabric (Nash and Hopkinson, 2004). Based upon Sommerfield's classification (1983), outlined in section 1.3.1, the majority of the units have a floating fabric, where both subtypes, massive and glaebular, are present in the profile. Two samples, SARP 8-11 and SARP 5-10, from the lower section, are classified as matrix-fabric since they only contain 1.5% framework grains. Additionally, they belong to the massive sub-type, though variations can occur within a single sample and even in thin sections. The poorly sorted sediments can display a floating fabric in one part of the thin section, and matrix fabric at another part of the same section. In extreme cases, a grain-supported fabric has been observed in pockets of a floating fabric sample. The conglomerates in the lower section have a conglomeratic fabric. The three sections in the Saranda profile display different silcrete morphologies and modes of formation.

5.5.1 Groundwater silcretes

Common features of the sediments belonging to the lower section are the absence of illuviation features and the absence of primary sedimentary structures. Loss of primary structures are common for pedogenically formed silcretes (Summerfield, 1983; Ulliyott et al., 1998; Thiry, 1999; Nash, 2011).

Opal can be formed by *in situ* transformation or replacement of clays, and Milnes and Thiry (1992) state that this can preserve structures and fabrics that are common in groundwater silcretes and deep horizon pedogenic silcretes, though, no sedimentary structures have been observed in the lower section. The absence of sedimentary structures can have two explanations: 1) there were originally no sedimentary structures when these sediments were deposited, or 2) primary structures, textures, and original mineralogy in the host rock is usually not preserved in silcretes that display a floating fabric (van der Graaff, 1983).

The quartz grains do not show any dissolution feature, in which case opal-CT in groundwater silcretes are correlated with the disappearance of clay minerals which were once present in the host rock (Thiry *et al.*, 2006).

Titanium may be present, but in lower concentrations than in pedogenic types (Ulliyott *et al.*, 1998). Samples from the lower section do contain less Ti than for the overlying section.

The lack of clay coatings around detrital grains, nodules, and illuviation features, which are common constituents in pedogenic silcretes, lead to the assumption that these silcretes have formed through the precipitation of groundwater.

5.5.2 Pedogenic silcretes

Silcretes from the middle section are classified as F-fabric, and belong to the massive subtype. Illuviation is a common feature in the middle section. As mentioned above, illuviation structures are a very common feature in pedogenically-formed silcretes, and develop where solutions have percolated. They are especially common at the base of voids, and against the walls of fissures (Thiry *et al.*, 2006).

Opaline silica is usually more common at the base of pedogenic silcretes (Thiry *et al.*, 2006), and is due to silica-saturated solutions in the upper layers, which migrate downwards. The upward decrease in opal in the middle section can be explained by a downward movement of highly concentrated silica solutions, leading to the precipitation of opal in the underlying beds. SARP 8-10 contains as much as 40 XRD% opal, and it is possible that this layer acted as a barrier for a further downward movement of the silica-saturated solution, leading to high precipitation of opal in this layer. Preservation of opal in the lower unit might suggest that it was protected from percolation solutions.

Silcretes from the upper section are classified as F-fabric type, and belong to the nodular subtype. Opal and chalcedony are absent in the upper section, and silica is present as microcrystalline quartz. The absence of opaline silica indicates that the solution was undersaturated with respect to opal-A and opal-CT, and instead quartz was precipitated (Williams *et al.*, 1985).

5.6 Geochemistry

Many factors influence the behavior of trace elements during sedimentary processes, and weathering, physical sorting, provenance, and diagenesis are factors that play an important role (Bhatia, 1986).

The abundance of Ti, Nb, and Ta in the SARP 2-10 samples can be due to the presence of ilmenite in the conglomerate. Nb is correlated positively with Ta (Table 3.4). There is a strong positive correlation between Cr and Ta in the SARP samples (Table 3.4), and the correlation is even stronger when just looking at correlation in FA1 samples (Appendix F). The extremely high Cr content (4520 ppm) in SARP 2-10 can be explained by the high abundance of Cr rich spinles (Table 3.3) and garnets in this sample, and can explain the outlier in Figure 3.19. Additionally, SARP 2-10

Lithium can be concentrated in micas, and can be incorporated in kaolinite during weathering (Middelburg *et al.* 1988). This can explain the very high distribution of Li in both FA2 and FA3 samples. FA2 and FA3 contains have an average kaolinite content of 9.5

XRD%, and 8.8 XRD%, respectively. Highest average Li content is found in FA3 (249 ppm), while FA3 contains an average of 228 ppm Li.

Highest average barium distribution in the Saranda profile is found in FA3 samples (1441 ppm) (Table 3.4). K-spar is considered the most important Ba-bearing mineral in granitic rocks (Nesbitt *et al.* 1980). However, FA3 samples has lower content of K-spar than the two underlying units with the average value of (9 XRD%). FA1 samples contain abundant K-spar with an average content of 44 XRD%. The average Ba distribution in FA1 is 1151 ppm (Table 3.4). Some samples are especially enriched in Ba, e.g. sample SARP 4-11 with 4990 ppm Ba, and some of these are also associated with with a very high K-spar content. However, this is not the case for all Ba-rich samples, e.g. sample SARP 5-10 which is composed of 65 XRD% K-spar (1080 ppm Ba). EMP and SEM analysis revealed that most K-spar present in this sample is of secondary origin, and could be an explanation for the “low” Ba distribution compared with FA3 where the K-spar is mostly detrital.

FA2 samples contain mostly authigenic K-spar, with the average content being 14 XRD%, Ba is found in lower concentration than in FA1 and FA3 (average 538ppm). However, FA3 contain less K-spar than FA2 and has a higher distribution of Ba (1441ppm).

The element Bi show extreme enrichments in sample SARP 5-11 (over 40 times the average value of what is in the crust. This is probably due to the mineral bismoclite (Fig.3.20) which is only detected in this sample.

5.7 Uranium

The uranium content within the SARP profile varies within single units of one facies association, from one unit to another, and in the three facies associations (Table3.4). The highest uranium values are found in the lower facies association, with a peak value of 394 ppm in SARP 5-11. The lowest recorded value in this section is 5.9 ppm in sample SARP 3-11. The mean value for the lower section is 54 ppm. In the middle section, the mean value is 11 ppm, and decreases to even lower values in the upper part to 8 ppm.

In Figure 5.6 the gamma values measured in the field have been correlated with the uranium values from the elemental analysis. The peaks in gamma radiation (red squares) measured in the field roughly match the uranium distribution of the respective layer (black circle). The two distributions seem related with the exception of a few points. This can be due to inhomogeneties in the different layers measured. The scintillation detector also picks up signals from thorium and potassium, which can show higher values than uranium in several samples (Appendix E). If rocks contain high amounts of potassium feldspars, like orthoclase and microcline, this can give high gamma radiation, and thus be responsible for outliers on the red curve.

The search for uranium bearing minerals with SEM and the EMP analysis has been negative. Uranium minerals, like carnotite, schröckingerite, tyuymunite, weeksite, and uranophane were not observed in any of the XRD diffraction patterns. The rocks are clearly enriched in uranium and a possible explanation for the absence of uranium bearing minerals in the XRD recordings could be that uranium is absorbed on minerals (Serra *et al.* 1980), e.g. clay minerals. Knivslund (2012) studied the chemical composition of the groundwater in areas close to the Saranda location. The ground water shows high concentration of uranium in the water samples. However, according to modeling by the PHREEQC program with the Ilnl database, the saturation index is too high for the uranium to be dissolved in the water (Knivslund, 2012). The uranium is most likely occurring as tiny particles, possibly adsorbed onto small clay sized grains (Knivslund, 2012). According to Rachova *et al.* (2010), uranium can migrate in the absorbed form on iron hydroxides, clay particles, and suspended organic matter. Uranium can also, according to Serra *et al.* (1980) and Zielinski (1980), be absorbed by amorphous silica, and in phosphate minerals e.g. apatite (Murray *et al.* 1983; Boyle, 1984). Murray *et al.*, (1983) argue that phosphate minerals have high capacity for retention of uranium and its daughter products. Knivslund (2012) has found that the groundwater in the area is oversaturated for, with amongst others, fluorapatite, hydroxylapatite, aluminosilicates, and iron-oxides, which probably exist as suspended colloids in the water with a diameter less than 0.45 μm . Zielinski (1980) studied uraniferous siliceous deposits in the Shirley Basin, Wyoming, and found that uranium was distributed as uranyl species within chalcedony crystals. Zielinski (1980) argues that this reflects a coprecipitation of dissolved uranium and colloidal silica in a uraniferous silica-gel.

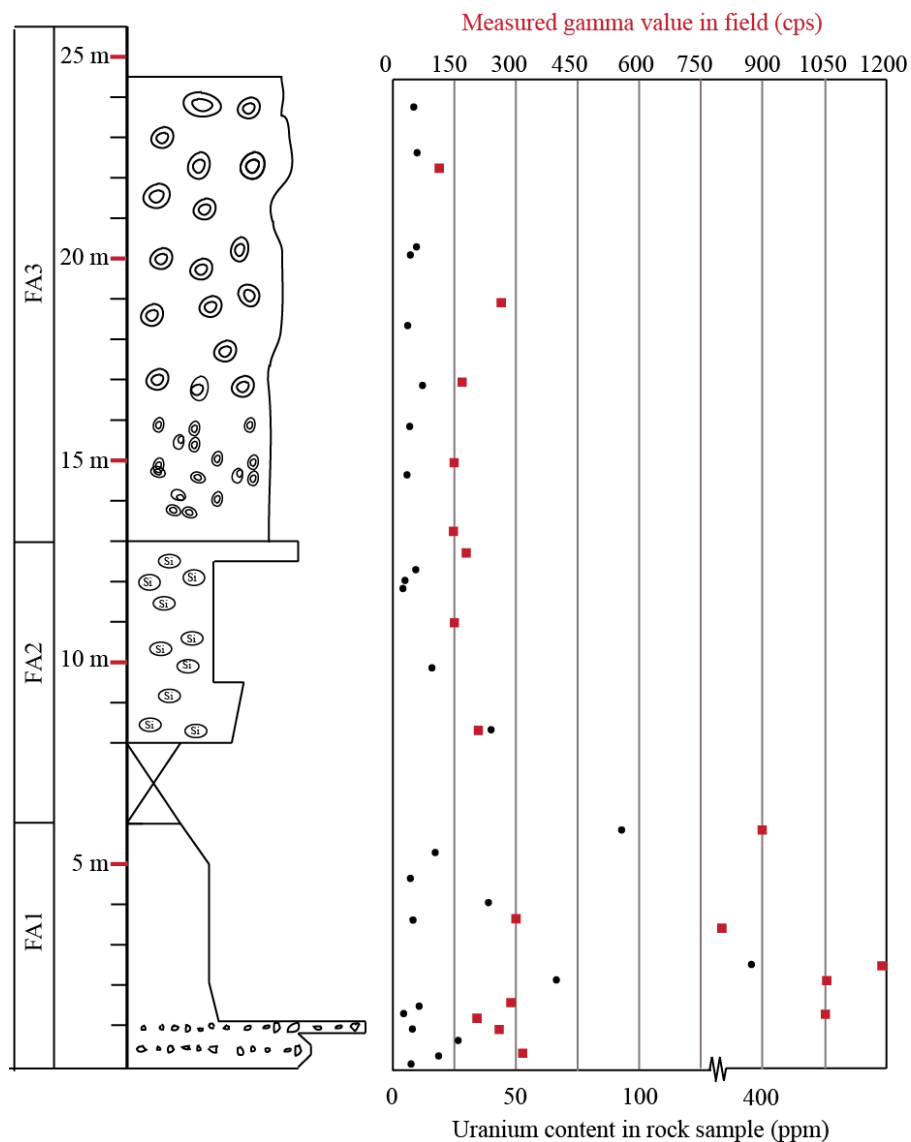


Figure 5.6 Simplified log of SARP profile merged with the uranium distribution (black circles) and measured gamma radiation from the field (red squares). The two lines follow roughly the same trend throughout the profile, and the high uranium content can be correlated with high measurements of natural gamma radiation in the field, except for one abnormally high gamma reading just above the conglomeratic unit. More closely-measured intervals in the field could possibly have produced improved correlation, but problems with the scintillation detector made this difficult.

Though FA1 and FA2 have been found to contain high amounts of opaline silica, there is no obvious correlation between opal and uranium in the SARP-samples (Fig.5.7).

Murray *et al.* 1983: Phosphate minerals like apatite have high capacity for retention of uranium and its daughter products. U and Ba strongly absorbed on apatite

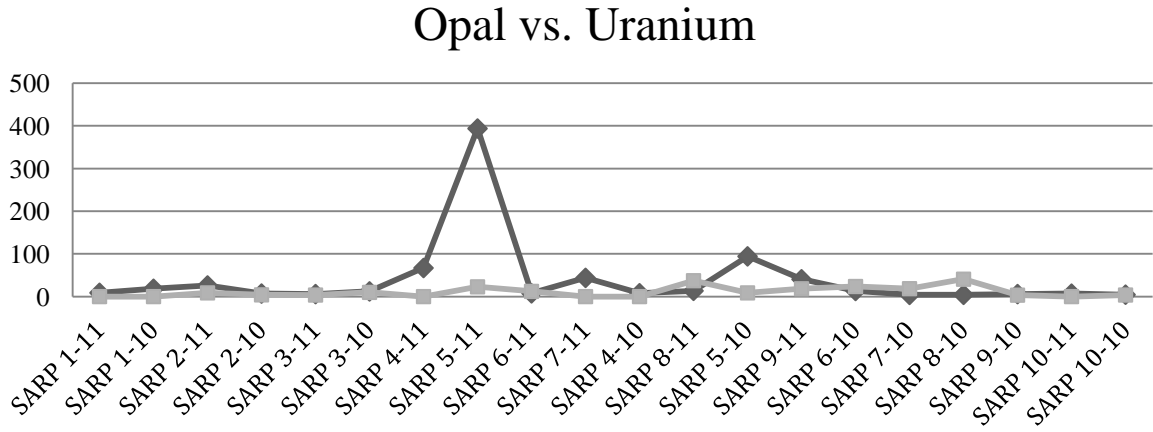


Figure 5.7 Comparison between the percentage of opaline silica (red line), and the uranium distribution in ppm (blue line) in SARP samples from FA1 and FA2.

The two highest recorded uranium values in the entire section are found in the two samples containing the highest portion of apatite: SARP 5-11, containing 394 ppm uranium and 26 XRD% apatite; and SARP 5-10, containing 94 ppm uranium and 5 XRD% apatite. A third sample, SARP 3-10, also contains apatite (2.3 XRD%) has fairly low uranium content compared to the other two samples (12 ppm uranium). Since SARP 5-11 and SARP 5-10 are the only sedimentary units containing apatite (except for SARP 3-10), and have the highest concentrations of uranium, it could indicate that apatite can be positively correlated with uranium. Furthermore, the concentration of uranium compared with the XRD % of apatite in these two samples is very similar, and it is most likely that the enrichments in uranium in these samples are a result of U-absorption in the apatite.

The present-day drainage system does not, most likely, coincide with the palaeodrainage system operating at the time the Kilimatinde Cement was deposited, due to younger generations of fault sets (Fig.1.7) that could have changed the drainage pattern and groundwater flow. It can only be speculated whether the uranium was in a dissolved state within the solutions that flushed the Saranda sediments.

Uranium sources and transport mechanisms

Several basement rocks from the Bahi area, collected in the 2010 field season, were geochemically analyzed for major and trace elements. The highest recorded uranium concentration was found to be 19 ppm (granites), with an average value being 4 ppm (Andresen, pers.com., 2012). The granite situated directly below the Saranda profile was found to contain 1.7 to 17 ppm uranium (Appendix D). These low concentrations in the basement rocks compared to some of the most enriched units the Saranda rocks give indicate that the source of uranium must be situated somewhere else. Geophysical data provided by UDSM can shed some light into this problem. An airborne geophysical survey executed by the Geological Survey of Tanzania in 1976-1980 collected aeromagnetic and radiometric data that can give information on the major structures and geological bodies in the study area and radioactive element distribution. Figure 5.8 shows the major uranium deposits in the area. In Muhalala, uranium occurs in shallow sediments, no deeper than ten meters below the surface (pers.comm. Marobhe 2012). The Uranium-rich deposits at Mytowo also show high concentrations, and further exploration has been planned. Furthermore, the geophysical data from the airborne geophysical survey mapped the Chenene Hills (Fig.1.7) as a highly radioactive body (Fig.5.9) with high enrichments in uranium (pers.comm. Marobhe, 2012). The Chenene Hills may, for this reason, be the closest source of uranium. The Chenene Hills are mapped as a granitic block, and are situated at an elevation of 2,060 m a.s.l. (Macheyeki *et al.*, 2008). The SAPR locality lies between to major fault escarpments, the Bubu fault and the Saranda fault, along the foothills of Chenene Hills. These two fault lines may act as funnels, localizing the sediments and water to the depositional site and thereby enhancing the concentration of uranium and other elements in these rocks. Since there are formations lying above Saranda (Fig.5.8), which are also rich in uranium, there must either be two different sources of uranium operating at different periods, or the source must be the same for both formations and be situated above the uppermost formation containing uranium.

Figure 5.8 *Data from the aeromagnetic study executed by Geological Survey of Tanzania, displaying areas with high natural gamma radiation. a) Geological bodies with high natural radioactivity in area close to Saranda. Areas with highest radiation are shown by red*

colour, low radiation by blue colour. The survey revealed that rocks situated in the Saranda area have high gamma radiation. (No scale). b) Mapping of uranium bodies in the same area showing medium counts in the Saranda area. Data provided by UDSM.

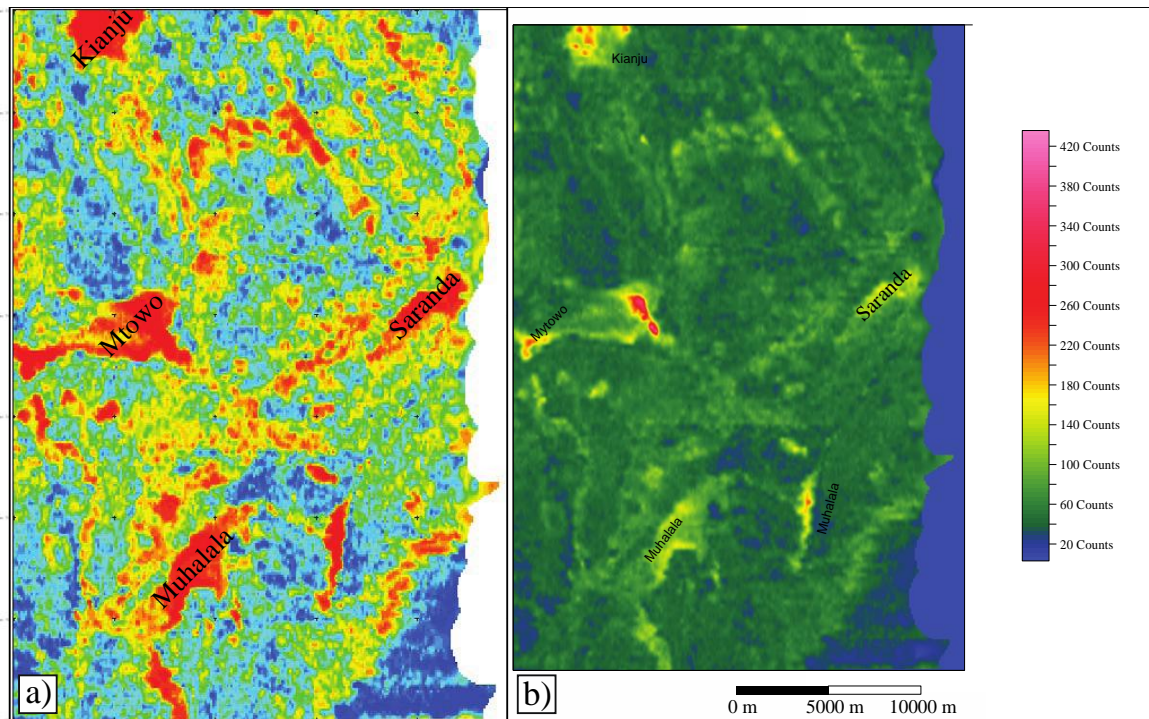


Figure 5.8

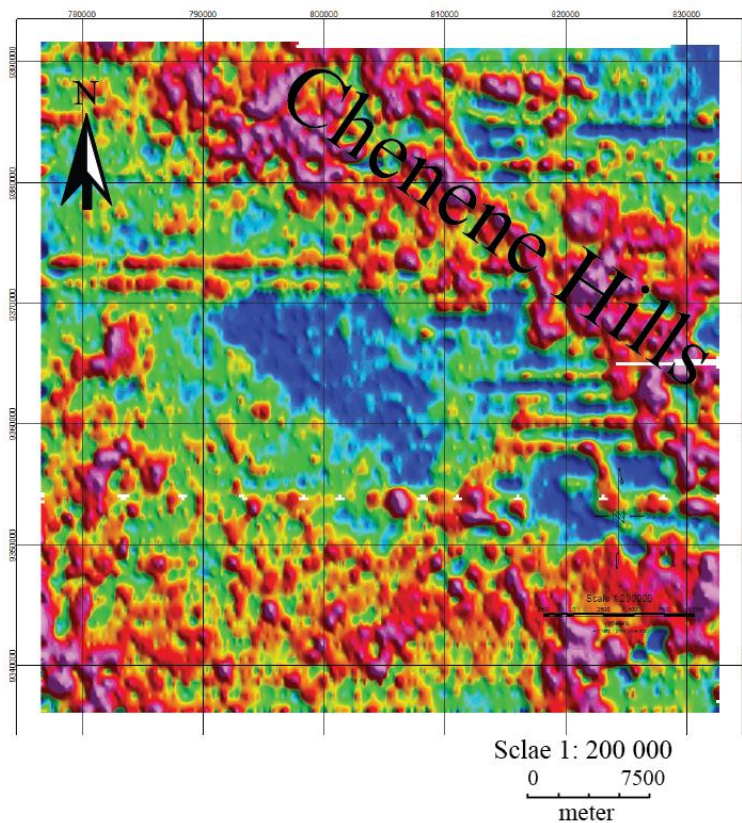


Figure 5.9 Data from the aeromagnetic study executed by Geological Survey of Tanzania reveals high gamma radiation (red) in the Chenene Hills.

The most plausible explanation of a transport mechanism from source to depositional site is groundwater flow within fractures in the basement. The airborne survey and borehole data revealed extensive sets of SW-NE trending fractures in the crust on the Saranda escarpment. Aquifers have also been located at about 70 m depth, which can transport huge volumes of water to the lower areas (pers.comm. Marobhe, 2012). Because of this, aquifers and major sets of fractures are a reasonable explanation.

5.8 Provenance

The composition of sedimentary rocks reflects the lithology of the source area, the processes that are operating during transport, and deposition of the sediments, as well as late diagenetic and weathering alterations. Climate and relief are the most important factors. The study of the detrital mineralogy of sediment or a sedimentary rock can give important information about the source area since each type of source rock tends to yield a distinctive suite of minerals which constitute a guide to the character of that rock (Pettijohn, 1975; Morton and Hallsworth, 1999).

Many rocks sampled from the lower section are rich in heavy minerals (ilmenite, spinel, garnets, perovskite), most of them are found as opaque mineral grains, though isotropic species are also found. SEM and EMP studies of some selected samples reveal that the most common heavy minerals are ilmenite, spinel, and garnet. Quantitative compositional analysis of these three minerals (Table 3.3), reveals unusual and rare compositions, which are usually associated with kimberlites (Clement *et al.*, 1984; Woolley *et al.*, 1996).

Kimberlites are potassic, ultrabasic, igneous rocks, composed of macrocrystals in a fine matrix. Olivine is the most abundant mineral present, and other common macrocrystals include: Mg-rich ilmenite, Cr-spinel, Mg-garnet, Cr-diopside, and enstatite. The most common matrix minerals include: olivine, carbonate, serpentine, diopside, perovskite, ilmenite, and apatite (Clement *et al.*, 1984; Woolley *et al.*, 1996).

Edwards and Howkins (1966) studied kimberlites in Tanzania and found that the main minerals present after olivine to be Mg-rich ilmenite, spinel, and Cr-rich garnet. More than 200 kimberlite localities have been found on the Tanzania Craton. Most of these

occurrences are situated south of Lake Victoria in the Precambrian terrain, through some have formed within the mobile belts (Schlüter, 1997). Presently, some kimberlites are exposed in areas where active erosion is ongoing, e.g. adjacent to rift-related fault scarps (Edwards and Howkins, 1966).

The three frequently occurring minerals in the lower section, Mg-rich ilmenite, Cr-rich spinel, and Cr-rich garnet, especially in the conglomeratic unit (SARP 2-10) where the concentration of heavy minerals are the highest, indicate that sediments are derived from an area where kimberlites are exposed at the surface. Perovskite together with spinel and ilmenite have also been found in one of the samples collected in the lower section, while red spinels, and isotropic minerals have been seen in the middle section, though at a lesser abundance. Red spinels have not been observed in the upper section, though a few isotropic grains have been seen.

The Chenene Hills are considered to be a granitic block (Macheyeki *et al.*, 2008), but the literature on this is sparse. Heavy minerals are not as abundant in the middle as in the lowermost unit, and are almost absent in the uppermost section where only a few grains have been detected in thin sections (Appendix B). The mineralogical composition in FA2 and FA3 are very different from FA1. FA2 and FA3 are mainly composed of quartz, microcline, and kaolinite. Kaolinite is a common weathering product of granites (Butt, 1985; Nesbitt and Young, 1987; Nesbitt *et al.*, 1997; White *et al.*, 2001), and its presence together with microcline and abundant quartz grains strongly indicates a granitic source terrain. FA1 on the other hand is mainly composed of quartz, microcline, orthoclase, and plagioclase, together with kimerberlittic macrocryst grains.

Kimberlites are common in Tanzania, and the author believes that there is a possibility that there could be a kimberlittic intrusion not yet mapped in the Chenene Hills region. Normal faulting and uplift may have exposed kimerblites in this area, and thus mass wasting processes may have transported kimerlittic debris to the depositional site. After a significant period, the outcrop would have been eroded down, and the weathering of granites would have been more severe and produced sediments with a granitic signature.

Minerals associated with kimberlites are also found in the middle unit, but are less abundant, and the detrital minerals yield evidence of more granite derived sediments. If the granite-

derived sediments were a result of reactivation of faults, we would expect to observe an increase in grain sizes, but this has not been observed in any samples. This leads to the assumption that this is probably a result of continuous erosion into deeper layers.

Sediments of the lower and middle section were already lithified when FA3 sediments started to accumulate. The hiatus between the middle and lower section can indicate a period of more stable tectonics where little or no sediments were deposited. If the weathering rate exceeds the ability of transport processes, the weathering products have a longer time to react with the soil and groundwater, thus affecting the composition of the detritus which could explain the abundant kaolinite in the upper section.

The mineralogy of the upper section can be interpreted to reflect a granitic source and few heavy minerals have been found in this part of the section compared to the lower units. The sediments deposited are most likely related to later tectonic activity, which exposed granites that could have been weathered and transported downhill to the depositional site.

If the detritus is quickly removed without significant modification from chemical weathering, the provenance signature of the parent rock is likely to be largely transferred into the transport system.

5.9 Chiguluka – similarities and differences

There are more differences between the Chiguluka and Saranda localities than there are similarities. Common for both field sites are a basal conglomerate situated unconformably upon weathered Archean basement.

The two upwards fining units have been interpreted to be deposited in a fluvial channel. The basal conglomerate is matrix-supported but clast concentration is greater than for the conglomerates in Saranda. Additionally, some clasts are imbricated, and the matrix content is lower than for Saranda. The basal conglomerate has been interpreted to have been deposited from catastrophic flows with high enough energy to transport larger clasts. The sand bed situated above is interpreted to represent waning flood deposit. The upwards fining units at the top of the profile are interpreted to be channel fill deposits. Both sections are composed of poorly sorted sediments, and the most common grain shape is sub-angular. Illuviation structures are found at both locations (except lower Saranda section), but are commonly more abundant in Chiguluka.

The Chiguluka deposits are poorly cemented, and as a result are very porous. Opal has not been detected in any CHIG-samples. Saranda on the other hand contains abundant opal in the lower and middle sections, and the whole section is well silicified.

Major differences exist between the two field sites when it comes to element distribution. Saranda shows enrichments with respect to several elements, while CHIG-samples display a more or less normal element distribution when compared with the crust (Appendix D).

Natural gamma radiation in the Chiguluka beds is very low compared to Saranda, and is continuous with the low uranium distribution in CHIG-samples. Highest uranium concentration in CHIG-samples is 1.5 ppm, which is less than the lowest value in Saranda (4 ppm).

Most likely, two very different solutions have percolated through these two sites since the geochemistry is so unlike. However, even though CHIG and SARP are situated directly upon the same Archean granite, it does not necessarily mean that these two deposits are of the same age. In areas where active tectonics is ongoing, the landscape is constantly changing; and sediment source, drainage, and groundwater paths may be very different.

Table 5.1 Comparison between Chiguluka and Saranda field sites.

	Chiguluka	Saranda	
Transport mechanism	Fluvial	Fluvial	Sediment deposition
Depositional environment	Fluvial	Lacustrine and fluvial	
Unconformably situated on Archean granite	Yes	Yes	Sediment-basement contact
Weathered basement	Yes	Yes	
Basal conglomerate	Yes	Yes	
Fabric	Matrix supported	Matrix supported	Rock characteristics
Maturity	Mature	Immature	
Degree of cementation	Low- very porous	High- very dense	
Sorting	Poor	Poor	
Grain shape	Sub-angular	Sub-angular to sub-rounded	
Opal	Absent	Present in lower and middle section	
Illuviation structures	Present	Present in middle and upper section	
Natural gamma radiation	50-80 cps	110-1200 cps	Geochemistry
Uranium distribution	0.7 - 1.5 ppm	4 - 394 ppm	
Element distribution	Normal	High	

Different water composition, drainage area and source rock would affect the geochemistry of the deposits, and might be the best explanation for the vast variations between the two profiles.

6. Conclusion

The Saranda and Chiguluka profiles reflect tectonically controlled deposition in a semi-arid setting, however, they have a very different geochemistry.

The Saranda sediments represent deposition in a lacustrine and fluvial setting. The profile is divided into three units on the basis of mineralogical composition and lithology. The lower profile has been deposited in a shallow lake, and silica has precipitated from silica saturated groundwater, classified as a groundwater silcrete. The lower and middle sections have been deposited in ephemeral fluvial channels. These deposits are classified as pedogenic silcretes, and cementation has occurred through the downward percolation of silica saturated solutions. Opal is found in samples from the lower and the middle sections, but is absent in the upper section. The percolating solutions must have been oversaturated with respect to both opal-A and opal-CT in the middle and lower sections, ultimately precipitating opal. The structural order of these opals increase downwards, the lower section contains more well-ordered polymorphs than the unit above.

The upper section stands out from the underlying sections due to a particular appearance- the surface is covered in nodules. These have most likely been formed *in situ* by mineral accretion related to the hydration/dehydration of unconsolidated sand, as is evident by the presence of geopetal structures. Moving pore fluids in these sediments may have displaced clastic grains to areas with less energy, causing denser packing in specific areas. During dehydration, a thicker film of water may be retained at the lower surface of these clusters, precipitating new minerals, and cementing them together. After the sediments have consolidated and been subjected to weathering at the surface, the matrix is weathered out more readily than the more resistant nodules, leaving a bumpy appearance that is visible at the outcrop today.

The mineralogical composition in the lower section differs from the middle and upper sections, strongly indicating two different sediment sources. The two upper units reflect a granitic source with the abundance of quartz, together with microcline and kaolinite. Kaolinite is absent in the lower section, but is found to contain orthoclase and plagioclase in addition to quartz and microcline. The assemblage of heavy minerals (Cr-spinel, Mg-rich ilmenite and Cr-rich garnet) in samples from the lower section indicate a kimerlitic source.

A break in sedimentation occurred in the transition between the middle and upper section, and sediment deposition did not occur until after the middle section was lithified. This assumption is based on the absence of vertical oriented chalcedony veins that are frequently found in the two underlying units. The chalcedony veins may be likened to the Bubu fault, which is known for its hot springs and associated chalcedony veins. Therefore, it is likely that the Saranda profile has been influenced by two tectonic events: the sediments of the lower and middle profile are associated with early rifting (Sanzawa fault), while the upper section has been subjected to more recent faulting (Bubu and Saranda fault) .

The Saranda deposits are enriched in several elements, especially uranium with a maximum distribution in the lower section (395 ppm). This is also confirmed by measurement of natural gamma radiation during the field season, with radiation of 300 – 1,200 cps. Uranium has not been found in its mineral form, and is most likely absorbed onto minerals. Maximum distribution is found in samples containing apatite. Based upon geophysical data provided by UDSM, the source of uranium can be pin-pointed to the Chenene Hills, where it is most likely transported by groundwater through fractures within the Archean basement.

It is not known if the Saranda and Chiguluka locations are of the same age. Chiguluka displays a normal uranium distribution and does not lean towards any other particular elemental enrichment.

There can be several explanations for the major differences in the two localities' chemistry: 1) they are not of the same age, 2) they are subject to a different source area, and 3) they both have a different drainage area. These are factors that may affect the composition of the groundwater, and may be responsible for the elemental depletions/enrichments found in these deposits.

References

- Bell, K. and Dodson, M.H. 1981. The Geochronology of the Tanzanian Shield. In: *The Journal of Geology* 89, 109-128.
- Bellucci, J.J., McDonough W. F. and Rudnick R.L. 2011. Thermal history and origin of the Tanzanian Craton from Pb isotope thermochronology of feldspars from lower crustal xenoliths. In (ed) Carlson R.W. *Earth and Planetary Science Letters* 301, 493–501
- Bhatia, M. R. and Crook, A. W. 1986. Trace element characteristics of graywackes and tectonic setting discrimination of sedimentary basins. In *Contributions to Mineralogy and Petrology*. Vol. 92. Pp 181-193.
- Bjørlykke, K. 2010. Petroleum Geoscience. From sedimentary Environments to Rock Physics. Springer-Verlag, 508 pp.
- Boniface, N. and Schenk, V. 2012. Neoproterozoic eclogites in the Paleoproterozoic Ubendian Belt of Tanzania: evidence for a Pan-African suture between the Bangweulu Block and the Tanzania Craton. In (eds.) Cawood, P.A., Parrish R.R. and . Zhao G.C. *Precambrian research* 208-211, 72-89.
- Boggs, S. 2006. Principles of sedimentology and stratigraphy. Upper Saddle River, N.J: Pearson Prentice Hall, 662.
- Bouch, J.E., Hole, M.J., Trewin, N.H., Chenery, S. & Morton, A.C. 2002. Authigenic apatite in a fluvial sandstone sequence: evidence for Rare-Earth Element mobility during diagenesis and a tool for diagenetic correlation. In *Journal of Sedimentary Research* 72, 59-67.
- Boyle, D.R. 1984. The Genesis of surficial uranium deposits. In *Surficial Uranium Deposits*. Report of the working group on uranium geology, International atomic energy agency, Austria 45-52.
- Brock, J. C. 1988. The Influence of Continental Rifting on the Hydrogeology of the Bahi Drainage Basin, Dodoma Province, Central Tanzania. In (eds.) Demissie, M. and Stout. G. E. *Proceedings of The Sahel Forum on the state-of-the-art of hydrology and hydrogeology in the arid and semi-arid areas of Africa*. 450- 460.

- Chesley, T., Rudnick, R. L. and Lee, C. 1999. Re-Os systematics of mantle xenoliths from the East African Rift: Age, structure, and history of the Tanzanian Craton. In *Geochimica et Cosmochimica Acta*, 63, 1203–1217.
- Chorowicz, J. 2005. The East African Rift System. In *Journal of African Earth Sciences*. 43, 379-410.
- Collinson, J. D. 1996. Alluvial sediments. In Reading, H. G. (ed.) *Sedimentary Environments: Processes, Facies and Stratigraphy* (4th edition). UK: Blackwell Publishing, 37-82.
- Compton, R. R. 1962. Manual of field geology. In *Soil Science* 93. New York: Wiley.
- Cullers, R. L. 2000. The geochemistry of shales, siltstones and sandstones of Pennsylvanian-Permian age, Colorado, USA: implications for provenance and metamorphic grade. In *Lithos* 51, 181-203.
- Dawson, J. B. 2008. The Gregory Rift Valley and Neogene – Recent Volcanoes of Northern Tanzania. Geological Society Memoir 33. UK: Geological Society. 99.
- Dypvik, H., Smelror, M., Sandbakken, P.T., Salvigsen, O. & Kalleson, E. 2006. Traces of the marine Mjølnir impact. In *Palaeogeography, Paleoclimatology, Palaeoecology* 241, 621-636.
- Elzea, J.M., Odom, I.E. and Miles, W.J. 1994. Distinguishing well ordered opal-CT and opal-C from high temperature cristobalite by x-ray diffraction. In *Analytica Chimica Acta* 286, 107-116.
- Elzea, J.M. & Rice, S.B. 1996. TEM and X-ray diffraction evidence for cristobalite and tridymite stacking sequences in opal. In *Clay and Clay Minerals* 44, 492-500.
- Flörke, O.W., Hollmann, R., von Rad, U. & Rosch, H. 1976. Intergrowth and Twinning in Opal-CT Lepspheres. In *Contributions to Mineralogy and Petrology* 58, 235-242.

Folk, R.L. 1951. Stages of textural maturity in sedimentary rocks. In *Journal of sedimentary petrology* 21, 127-130.

Folk, R.L. 1954. The Distinction between Grain Size and Mineral Composition in Sedimentary-Rock Nomenclature. In *The Journal of Geology* 62, 344-359.

Fozzard, P. M. H. 1959. The geology of the Mpondi river area; quarter degree sheet 123 (41 N.W.), Kwa Mtoro. In *Records of the Geological Survey of Tanganyika*, 10-15

Gaillou, E., Delaunay, A., Rondeau, B., Bouhnik-le-Coz, Fritsch, E., Cornen, G. and Monnier, C. 2008. The geochemistry of gem opals as evidence of their origin. In *Ore Geology Reviews* 34, 136-126.

Ghisoli, C., Caucia, F. & Marinoni, L. 2010. XRPD patterns of opals: a brief review and new results from recent studies. In *Powder Diffraction* 25. 274-282.

Goudie, A. S. 1983. Calcretes. In Goudie, A.S. and Pye, K. (eds.) *Chemical sediments and geomorphology: precipitates and residua in the near-surface environment*. London: Academic Press, 93-133.

Guthrie, G. D., Bish, D. Jr. L. and Reynolds, R. Jr. C. 1995. Modeling the X-ray diffraction pattern of opal-CT. In *American Mineralogist* 80, 869-872.

Hay, R. L. and Reeder, R. J. 1978. Calcretes of Olduvai Gorge and the Ndolanya Beds of northern Tanzania. In *Sedimentology* 25, 649-673.

Isaacs, C.M. 1982. Influence of rock composition on kinetics of silica phase changes in the Monterey Formation, Santa Barbara area, California. In *Geology* 10, 304-308.

Jones, J. B., and Segnit, E. R. 1971. The nature of opal I. nomenclature and constituent phases. In *Journal of the Geological Society of Australia* 18, 57-86.

Jones, J. B., and Segnit, E. R. 1972. Genesis of cristobalite and tridymite at low temperatures. In *Journal of Geological Society of Australia* 18, 417-422.

Kamber, B. S., Greig, A. and Collerson, K. D. 2004. A new estimate for the composition of weathered young upper continental crust from alluvial sediments, Queensland, Australia. In *Geochemica et Cosmochimica*. 69, 1041-1058.

Kilimajaro Mining Company (2008) *Geology of Tanzania*. Available at : <http://www.kilimanjarominingcompany.com/africanminingoperations/uranium/documents/Uranium%20InTanzania06.08.pdf> (Accessed on November, 2011).

Knivslund, S. 2012. *The main characteristics of the groundwater in the Bahi-Manyoni Basin in Tanzania*. Unpublished master thesis. Oslo, UiO.

Kreuser, T. Wopfner, H., Kaaya, C. Z., Markwort, S., Semikiwa, P. M. and Aslandis, P. 1990. Depositional evolution of permo-triassic karoo basins in Tanzania with reference to their economic potential. In *Journal of African Earth Sciences (and the Middle East)* 10, 151-167.

Lamplugh, G.W. (1902) Calcrete. *Geological Magazine*. 9, 75.

MaCartney, M. 2007. Technical Note: Hydrology of the Bahi wetland, Tanzania. Available at: <http://ideas.repec.org/p/iwt/bosers/h040528.html>. (Accessed: 08.03.2012)

Marobhe, I. University of Dar es Salaam. Pers. Comm. May 31st, 20112)

Macheyeki, A. S., Delvaux, D., Batist, M. De and Mruma, A. 2008. Fault kinematics and tectonic stress in the seismically active Manyara-Dodoma Rift segment in Central Tanzania – Implications for the East African Rift. In *Journal of African Earth Sciences* 51, 163-188.

Middelburg, J. J., Van der Weijden, C. H. and Woittiez, J. R. W. 1988. Chemical processes affecting the mobility of major, minor, and trace elements during weathering of granitic rocks. In *Chemical Geology* 68, 253-273.

Milne, G. 1947. A Soil Reconnaissance Journey Through Parts of Tanganyika Territory December 1935 to February 1936. In *Journal of Ecology* 35, 192-265.

Moore, D.M. and Reynolds, R.C. 1997. *X-Ray Diffraction and the Identification and Analysis of Clay Minerals*: Oxford, Oxford University Press. 378.

- Möller, A. , Appel, P., Mezger, K. & Schenk, V. 1995. Evidence of a 2Ga subduction zone: eclogites in the Usagarian Belt of Tanzania. In *Geology* 23, 1067-1070.
- Murray, F. H., Brown, J.R., Fyfe, W.S. and Kronberg, B.I. 1983. Immobilization of U-Th-Ra in mine wastes by phosphate mineralization. In *Canadian Mineralogist* 21, 607-610.
- Nash, D.J. & Hopkinson, L. 2004. A Reconnaissance Laser Raman and Fourier Transform Infrared Survey of Silcretes from the Kalahari Desert, Botswana. In McLaren, S. J., Nash, D. J. and Goudie, A. S. (eds.) *Earth surface processes and landforms* 29,1541-1558.
- Nash, D. J. 2011. Desert crust and rock coatings. In Thomas, D. S. G. (ed.) *Arid Zone Geomorphology: Process, Form and Change in Drylands*. Chichester, UK: John Wiley & Sons, Ltd, 151-159.
- Nash, D.J. & Ullyott, J.S. 2007. Silcrete. In Nash, D.J. & McLaren (eds.) *Geochemical Sediments and landscapes*. Blackwell publishing Ltd. 95-141.
- Nesbitt, H.W. & Young, G.M. 1989. Formation and Diagenesis of Weathering Profiles. In *Journal of Geology* 97, 129-147.
- Newman, J.L. 1970. Subsistence Change among the Sandawe of Tanzania. In *National Academy of Science, USA*. 199.
- Nyblade, A.A., Birt, C., Langston, C.A., Owens, T.J. and Last, R.J. 1996. Seismic Experiment Reveals Rifting of Craton in Tanzania. In *Eos. Trans. AGU.* 77, 517-528.
- Nyblade, A. and Brazier, R. A. 2002. Precambrian lithospheric controls on the development of the East African rift system. In *Geology* 30, 755-758.
- Milnes, A.R. and Thiry, M. 1992. Silcretes. In Martini, I.P. & Chesworth, W. (eds.) *Weathering, soils and palaeosols. Developments in Earth Surface Processes* 2. Amsterdam: Elsevier. 349-377.
- Owens, T.J., Nyblade, A.A., Gurrola, H. and Langston, C.A. 2000. Mantle Transition Zone Structure Beneath Tanzania, East Africa. In *Geophysical Research Letters* 27, 827-830.

- Petschick, R. 2011. *MacDiff 4.2.6 Manual* Available from: <http://www.geologie.uni-frankfurt.de/staff/homepages/Petschick/PDFs/MacDiff%20Manual%20E.pdf> (Accessed: January 2012)
- Potter, P. E., Maynard, J.B. and Depetris, P.J. 2005. Muddy Depositional Systems. In Potter, P. E., Maynard, J.B. and Depetris, P.J. (eds.) *Mud and Mudstones*. Germany: Springer-Verlag. 75-124.
- Powers, M. C. 1953. A New Roundness Scale for Sedimentary Particles. In *Journal of Sedimentary Petrology* 23, 117-119.
- Rachkova, N. G., Shuktomova, I. I. and Taskaec, A. I. 2010. The State of Natural Radionuclides of Uranium, Radium, and Thorium in Soils. In *Eurasian Soil Science*. Vol. 43, pp. 698-705.
- Rust, B. R. 1981. Sedimentation in arid-zone anastomosing fluvial system: Copper's Creek, Central Australia. In *Journal of Sedimentary Petrology* 51, 745-755.
- Schlüter, T. 1997. *Geology of East Africa*. Germany: Gebrüder Borntraeger. 484 pp.
- Semkiwa, P.M. 2005. Opportunities for Mineral Resource Development Tanzania. Government of the United Republic of Tanzania, Dar es Salaam, 130pp.
- Serra, O., Baldwin, J., and Quirein, J. 1980. Theory, interpretation and practical applications of natural gamma ray spectroscopy. Conference paper. *Society of Petrophysicists and Well-log Analysts*. 30 pp.
- Spence, J. 1951. The Chalcedonic Sandstones exposed in the Makutupora-Manyoni section of the Central Railway Line. In *Records of the Geological Survey of Tanganyika*. Dar Es Salaam, Tanzania. 39-44.
- Smith, D. K. 1997. Evaluation of the detectability and quantification of respirable crystalline silica by X-ray diffraction methods. In *Powder Diffraction* 12, 200-227.
- Smith, D. K. 1998. Opal, cristobalite, and tridymite: Noncrystallinity versus crystallinity, nomenclature of the silica mineral and bibliography. In *Powder Diffraction* 13, 2-19.

- Summerfield, M.A. 1983. Silcretes. In Goudie, A.S. and Pye, K. (eds.) *Chemical sediments and geomorphology: precipitates and residua in the near-surface environment*. London: Academic Press, 59-91.
- Talbot, M. R. and Allen, P. A. 1996. Lakes. In Reading, H. G. (ed.) *Sedimentary Environments: Processes, Facies and Stratigraphy (4th edition)*. UK: Blackwell Publishing, 83-123.
- Taylor, S. R. 1965. The application of trace element data to problems in petrology. In *Physics and Chemistry of the Earth* 6, 133-213.
- Thiry, M. 1999. Diversity of Continental Silicification Features: Examples from the Cenozoic Deposits in the Paris Basin and Neighbouring Basement, In M. Thiry and R. Simon-Coinçon (eds) *Palaeoweathering, Palaeosurfaces and Related Continental Deposits*. Oxford, UK. : Blackwell Publishing Ltd.
- Thiry, M. & Millot, G. 1987. Mineralogical forms of silica and their sequence of formation in silcretes. In *Journal of Sedimentary Research* 57, 343-352.
- Thiry, M. & Milnes, A.R. 1990. Pedogenic and groundwater silcretes at Stuart Creek Opal Field South Australia. In *Journal of Sedimentary Petrology* 61, 111-127.
- Thiry, M., Milnes, A.R., Rayot, V. & Simon-Coinçon, R. 2006. Interpretation of palaeoweathering and successive silicifications in the Tertiary regolith of inland Australia. In *Journal of the Geological Society* 163, 723-736.
- Tunbridge, I. P. 1984. Facies model for sandy ephemeral stream and playa complex; the Middle Devonian Trentishoe Formation of North Devon, U.K. In *Sedimentology* 31, 697-715.
- Ulliyott, J.S., Nash, D.J. & Shaw, P.A. 1998. Recent advantages in silcrete research and their implications for the origin and palaeoenvironmental significance of sarsens. In *Proceedings of the Geologists Association* 109, 255-270.
- Ulliyott, J.S. and Nash, D.J. 2006. Micromorphology and geochemistry of groundwater silcretes in the eastern South Downs, UK. In *Sedimentology* 53, 387-412.

Van der Graaff, W.J.E. 1983. Silcrete in Western Australia: geomorphological settings, textures, and their genetic implications. Geological Society, London, Special Publications 11, 159-166.

Webb, J.A. & Golding, S.D. 1998. Geochemical mass-balance and oxygen-isotope constraints on silcrete formation and its palaeoclimatic implications in southern Australia. In *Australian Journal of Sedimentology* 68, 981-993.

Wentworth, C.K. 1922. A scale of grade and class terms for clastic sediments. In *Journal of geology* 27, 377-392.

White, A. F., Bullen, T. D., Schulz, S., Blum, A. E., Huntington, T. G. and Peters, N. E. 2001. Differential rates of feldspar weathering in granitic regolith. In *Geochimica et Cosmochimica* 65, 847-869.

Williams, L.A., Parks, G.A. & Crerar, D.A. 1985. Silica Diagenesis, I. Solubility Controls. In *Journal of Sedimentary Petrology* 55, 301-311.

Williams, L.A. & Crerar, D.A. 1985. Silica Diagenesis, II. General Mechanisms. In *Journal of Sedimentary Petrology* 55, 312-321.

Wopfner, H. 2002. Tectonic and climatic events controlling deposition in Tanzanian Karoo basins. In *Journal of African Earth Sciences* 34, 167-177.

Zielinski, R.A. 1980. Uranium in Secondary Silica: A Possible Exploration Guide. In *Economic Geology*. Vol. 75. Pp. 592-602.

SARANDA

Appendix A – Thin section data

Facies association	Sample	Height above basement (m)	Facies	Most common grain contact	Average size 10 biggest grains (mm)	Sorting	Predominant grain shape	Preservation feldspar		Silica	Matrix	Remarks	Porosity %
								Plag.	K-spar				
FA1	SARP 1-11	0.1	ii	GS		Good	Angular	4	3	Brownish chess like chalcedony as cavity linings. Also part of cement	Dark yellow with muscovite and biotite fragments	70% of feldspars are seritized. Fractures filled with cement.	> 1
	SARP 1-10	0.33	ii	F	1.4	Poor	Sub-angular to sub-rounded			Some small patches of brown cloudy opal	Dark, yellow-brownish	Isotropic grains	30
	SARP 2-11	0.8	ii	F		Poor	Angular to sub-rounded	2	3	Patches of brown opal. Small chess-like chalcedony as fracture linings	Yellow, light brown, dark brown. Heterogeneous	Fractures, medium connectivity	10-15
	SARP 2-10	1.20	i	F	5.1	Poor	Angular to rounded	5	4	As cement, light translucent	Beige to light brown/yellow	Seritization of feldspars, partial dissolution and/or breakage of rock fragments cemented together. Rim seen enclosing several grains.	10
	SARP 3-11	1.50	ii	F to GS		Medium to poor	Sub-angular to sub-rounded	4	3	As brown isotropic opal	Yellow/green to beige	Well cemented, low to non-permeability. Denser packing of grains than above	5
	SARP 3-10	1.80	ii	F	1.3	Poor	Angular to sub-rounded	5	-	As brown isotropic opal and white translucent matrix	Beige to brown	Very low permeability, grain dissolution (F-spar) and seritization	5
	SARP 4-11	2.10	ii	F to GS		Medium	Sub-rounded			As brown isotropic opal (extensive) and white translucent matrix	Beige to dark brown	dense packing of grains as in 3-11	3
	SARP 5-11	2.50	ii	F to GS		Medium	Not recognizable. Intact grains are angular			As translucent white opal, and dark brown isotropic opal.	Silica	Slide parted in two, 1) Grain dissolution rimmed by dark brown opal, black in xpl.2) ghost grains off-white in ppl, dark gray to light luminous in xpl.	0
	SARP 6-11	3.60	ii	F		Poor	Sub-rounded	4	-	Brown opal, zebraic chalcedony, small crystallites of chalcedony,	Greenish yellow	Ghost of seritized F-spar, filled with small crystals of chalcedony. High portion of rock fragments are fractures, fractures filled with chess-like chalcedony + chalcidonic rim enclosing those grains	1
	SARP 7-11	4.30	ii	F		Poor	Sub-angular	4	-	As brown opal (not as pronounced)	Beige.	High portion of isotropic, some opaque and h.m grains	20
	SARP 4-10	4.9	ii	F to GS	2.35	Medium to poor	Angular to sub-angular	4	4	White? translucent	Pale turquoise to beige	Rock frag. Dissolution. Minor seritization	30
	SARP 8-11	5.5	iii	M		Poor	Sub-rounded	4	-	Brown and white translucent opal. Ca.2 cm chalcedony. 0.025 individual crystals. Zebraic chalcedony average 0.74	Silica: dark brown, yellow to off-white	Very few detrital grains	5
SARP 5-10	5.8	iii	M	0.44	Poor	Sub-rounded	5	4	Dark brown opal, extensive. Chalcedony. Chess-lie chalcedony as cavity/fracture linings, very small	Brown to dark brown	Brown opal occurring as floating structures?	5	
	SARP 9-11	8.5	v	F		Poor	Sub-rounded	4	0	Micro-chalcedony infilling in cavities. Dark brown isotropic opal. White translucent opal	Off-white to yellow and dark brown	Grain concentration varies, some parts densely packed, other parts floating to matrix dominated	5
	SARP 6-10	9.9	iv	F	1.6	Poor	Sub-angular	5	-	White translucent opal, brown opal some places (minority)	Off-white to yellow and brown	Silica precipitated in sec.pores (dissolution of feldspar). Grain concentration varies, very low where white silica	3

FA2	SARP 7-10	11.8	<i>Iv</i>	F	1.8	Poor	Sub-angular	-	5	Brown opal (extensive), and white opal	Dark brown, to yellow and off-white	White silica in broad bands	15
	SARP 8-10	12.7	<i>v</i>	F	2	Poor	Sub-angular	5	-	Homogeneous bands (off-white to yellow) opal, a few small patches of brown opal	Light yellow	Illuviations, especially around cavities and fractures. Homogeneous parts are matrix dominated. Other places the grain to grain	5
	SARP 9-10	12.8	<i>v</i>	F to GS	2.5	poor	Sub-angular	5	4	White homogeneous opal, a few small patches of opal	Yellow to brown	High portion of opaque min. grains. Illuviations. Grain breakage and dissolution.	1
	SARP 10-11	13.2	<i>v</i>	F	2	Poor	Sub-angular	5	4	Non seen	Yellow/beige to brown, coarse	Possible nodule formation. Concentric layer, who has different optical properties under xpl, incorporates some grains. 4 bigger structures are seen enclosed by darker brown matrix, lighter inside nodules.	
	SARP 10-10	14.8	<i>v</i>	F	1.7	Poor	Angular to sub-rounded	5	4	light yellow, homogeneous, numerous in cavities etc.	Light brown, coarse	Lamina is better developed at the lower end, thinner at the top. Numerous opaque grains (sub-rounded).	3
FA3	SARP 11-10	15.8	<i>vi</i>	F	1.85	Poor	Sub-angular	4	-		Coarse dark brown to yellow	Individual and/or cluster of grains are enclosed by concentric rims, with alternating layers, which show different optical properties under xpl. Majority has thicker lamina at the bottom of the grain/structure. Some show different orientation	50
	SARP 11-11	17.0	<i>vi</i>	F	1.7	Poor	Sub-angular	4	5		Beige	Quartz are poorly preserved in many cases, fractured	
	SARP 12-10		<i>vii</i>	F	1.7	Poor	Sub-angular	4	3	One infilling of a pore that could be homogeneous beige silica	Beige to off-white and brown	Fewer grains than 11-10 are enclosed by rims, nodules not as pronounced	30
	SARP 13-10	20.2	<i>vii</i>	F	1.8	Poor	Sub-rounded	-	4		Coarse beige to brown	Illuviations in yellow homogeneous substance (yellow xpl). Illuviations also in matrix. Majority has thicker lamina at the lower part. Grains show different orientation, some has lamina thickest on other sides	30
	SARP 14-10	20.4	<i>vii</i>	F to GS	2.5	Poor		5	4	Possible the lightest homogeneous, found around some concretions and pores	Coarse beige to dark brown	Light brown homo, yellow to black in xpl. Grain enclosed by nodules, different orientations.	40
	SARP 15-10	22.8	<i>vii</i>	F to GS	1.7	Poor	Sub-rounded	-	5				
	SARP 16-10	24	<i>vii</i>	Floating	1.9	Poor	Sub-rounded	4	4		Numerous illuviations	One big nodule, light yellow matrix, finer than above. Iron oxides around fractures, pores. Enclosed by several sets of lamina. Grains within are not enclosed by lamina. A few grains on the outside does, but not as pronounced as below.	10

CHIGULUKA

	Facies	Sample	Height Above basement	Most common grain contact	Average grains size	Average size 10 largest grains	Sorting	Predominant grain shape	Preservation feldspar	K-spar	Matrix	Remarks	Porosity %
									Plag.				
CHIG I	i	CHIG I 1-10	0,6	F to GS	Coarse sand	7,5	Very poor	Angular	5	3	Silty matrix	Contain abundant rock fragment grains, and polycrystalline quartz. Both pegmatitic and granitic types. Very poor preservation on f-spar i R.F (4-5), many are seritized. Numerous brown illuviations.	30
		CHIG I 3-11	0,9	F	Medium sand	6	Poor	Angular to sub-angular	4	3	Brownish, fine silt sized, abundant.	Red staining by oxi.iron. Biggest grains are polycrystalline quartz, and rock fragments. Seritized f-spar in rock fragments.	30
	ii	CHIG I 4-11	1,1	F	Very fine sand	2	Poor	Sub-angular	4	3	Fine silt	Numerous illuviations around fractures and pores. Seritization of f-spars n R-F-	60
		CHIG I 7-11	5,2	F	Fine sand	3,1	Poor	Sub-rounded	4	4	Greenish yellow	Numerous illuviations around fractures and pores. Low concentration of clastic grains. Dark brown staining of oxidized iron.	50
	iii	CHIG I 2-10	2,9	F	Fine sand	2,4	Poor	Sub-angular	5	3	Fine silty matrix, light to dark brown	Abundant heavy mineral grains, Numerous illuviation structures arround cavities and fractures. Majority of the biggest grains are polycrystalline quartz.	60
		CHIG I 3-10	3,4	F	Fine sand	1,7	Poor	Angular to sub-rounded	4	3	Little matrix, fine silt.	Biggest grains are polycrystalline quartz. Seritized F-spars in rock fragments. Loosely cemented. Illuvitaion present.	30
		CHIG I 4-10	3,8	F to GS	Medium sand	3,2	Medium	Angular to sub-angular	4	3	Sparse matrix, fine silt	Red staining. Seritization of feldspars fragments. And some individual grains. Some illuviation	5
	v	CHIG I 6-10	5,2	F	Fine sand	3,7	Poor	Sub-angular	4	4	Fine silt	Illuviations.	60
i		CHIG II 3-11	0,3	F	Coarse sand	6,4	Poor	Sub-angular	4	5	Very spare matrix, highly porous	Biggest grains are fragments. Seritized F-spars and associated dark brown staining by oxidized iron. Some loose biotite peaces in fractures. Some fragments with brown biotite and green chlorite. Some chlorite grains floates in matrix. Minor illuviations	30
	ii	CHIG II 1-10	0,45	F to GS	Coarse sand	5,4	poor	sub-angular	5	4	Beige.	Hhigh portion of isotropic grains, some opaque and heavy mineral grains as well.	30
iii		CHIG II 4-11	0,7	F	Fine sand	2,3	Poor	Sub-angular	4	3	Fine silt	Numerous illuviations around fractures and pores. Seritization of f-spars in rock fragments.	20
	iv	CHIG II 2-10	1,2	F	Medium sand	2,7	Poor	Sub-angular	3	4	Fine silt	Biggest grains are rock fragments with seritized F-spar. Dark red staining is also found in these fragments on top of feldspars. Illuviations around fractures and pores.	30
v		CHIG II 5-11	1,3	GS	Medium sand	2,9	Poorly	Sub-angular	5	3	Sparse matrix, fine silt	Numerous brown illuviations, pores fracture. Polycrystalline quartz and rock fragments biggest grains (feldspars 5).	50
	vi	CHIG II 6-11	2,1	F	Medium sand	3,5	Poorly	Sub-angular	4	4	Fine silt, light brown	Some light brown illuviations. Biggest grains are rock fragments.	50
CHIG II 7-11		2,9	F	Medium sand	1,6	Poor	sub-rounded	3	5	fine silt	Loose biotite grains. Numerous illuviations. Biggest grains are polycrtstalline quartz	50	
CHIG II 3-10	3,2	GS (f)	Fine sand	3	Medium	Sub-rounded	4	5	Sparse, fine silt	F-spar (5), Rock fragments and poly.quartz constitute the biggest grains. Seritization of f-spar on rock fragments. Loosly cemented. Minor illuviations.	30		

Appendix B: Point counting data

	QUARTZ			FELDSPAR							R.F	H.M	ISO.	OPQ.	MATRIX	CEMENT	ILLUV.	OPAL	CDNY.	POR.	FRACT.	HOLE	IRON OX.	SERZ.
	Total qtz.	Monocrystalline		Polycrystalline	Plag.	K-spar	Total																	
		Und.	Non-und.	Und.																				
SARP 1-11	24.0	18.5	4.5	1.0	15.3	13.8	29.0	1.2	0.2	0.0	0.0	0.0	17.7	0.0	5.7	0.0	0.2	0.0	0.0	0.0	0.0	21.7		
SARP 1-10	7.3	7.3	0.0	0.0	4.0	5.6	9.6	0.0	0.0	0.0	0.0	71.3	0.0	0.3	0.3	0.0	10.6	0.0	0.0	0.3	0.0	0.0		
SARP 2-11	9.9	4.3	0.3	5.3	1.0	0.3	1.3	0.0	0.0	0.0	0.0	55.3	0.0	0.6	30.0	0.0	0.0	0.3	0.0	0.0	0.0	0.0		
SARP 2-10	30.0	12.7	0.5	16.8	1.8	0.7	2.5	5.4		9.2	2.7	33.6	0.0	0.0	13.3	0.0	0.0	2.9	0.0	0.0	0.0	0.0		
SARP 3-11	36.2	23.3	2.3	10.6	1.0	0.3	1.3	0.6	0.0	0.0	0.0	49.0	0.0	0.0	12.0	0.0	0.0	0.6	0.0	0.0	0.0	0.0		
SARP 3-10	8.3	4.5	1.5	2.3	1.0	0.0	1.0	0.0	0.0	1.0	0.0	56.8	0.0	0.0	23.8	0.0	9.3	0.0	0.0	0.0	0.0	0.0		
SARP 4-11	36.2	23.3	3.6	9.3	2.3	0.3	2.6	0.6	0.0	0.0	0.0	51.0	0.0	0.0	9.3	0.0	0.0	0.0	0.0	0.0	0.0	0.0		
SARP 5-11	1.3	1.3	0.0	0.0	0.0	0.3	0.3	0.0	0.0	0.0	0.0	46.9	0.0	0.0	48.0	0.0	0.0	0.3	3.5	0.0	0.0	0.0		
SARP 6-11	20.0	15.0	2.0	3.0	0.3	0.0	0.5	1.6	0.0	0.0	0.0	26.3	0.0	0.0	24.6	27.0	0.0	0.0	0.0	0.0	0.0	0.0		
SARP 7-11	7.6	7.0	0.6	0.0	2.6	0.0	2.6	0.0	0.0	0.6	0.0	81.0	0.0	0.0	0.0	0.0	0.0	0.0	0.0	6.0	0.0	2.0		
SARP 4-10	41.7	31.5	3.0	7.5	3.0	2.0	5.0	1.5	0.0	0.7	0.2	44.2	0.0	0.0	6.2	0.0	0.0	0.2	0.0	0.0	0.0	0.0		
SARP 8-11	1.0	1.0	0.0	0.0	0.3	0.0	0.5	0.0	0.0	0.0	0.0	25.6	0.0	0.0	24.3	42.0	0.0	0.0	0.0	6.6	0.0	0.0		
SARP 5-10	2.2	1.8	0.5	0.0	1.8	0.5	2.2	0.0	0.0	7.5	0.2	47.0	0.0	0.0	39.2	1.5	0.0	0.0	0.0	0.0	0.0	0.0		
SARP 9-11	16.6	13.0	0.6	3.0	0.0	0.0	0.0	0.0	0.0	0.0	0.0	46.3	0.0	2.0	25.3	0.0	0.0	0.0	9.0	0.0	0.0	0.0		
SARP 6-10	21.3	15.6	2.7	3.0	1.0	0.0	1.0	1.0	0.0	0.0	0.0	37.6	0.0	0.3	31.0	0.0	0.0	0.0	0.0	7.6	0.0	0.0		
SARP 7-10	44.0	24.0	3.0	17.0	0.0	0.3	0.3	0.0	0.0	0.5	0.0	14.6	0.0	15.0	44.6	0.0	0.0	0.0	0.0	9.6	0.0	0.0		
SARP 8-10	54.6	31.4	1.3	21.3	1.0	0.0	1.0	1.6	0.0	0.3	0.0	5.3	0.0	1.6	34.3	0.0	0.0	0.0	1.0	0.0	0.0	0.0		
SARP 9-10	52.0	32.7	0.3	19.0	2.0	2.3	4.3	1.3	0.0	0.6	0.0	5.0	1.3	4.0	24.6	0.0	0.0	0.0	6.6	0.0	0.0	0.0		
SARP 10-11	39.9	34.3	2.3	3.3	1.0	0.6	1.6	0.3	0.3	0.0	0.0	54.0	0.0	0.3	0.3	0.0	0.0	0.0	2.0	1.3	0.0	0.0		
SARP 10-10	50.0	31.4	4.3	14.3	1.8	0.3	2.0	0.0	0.0	0.0	0.0	39.6	0.0	0.3	1.6	0.0	0.0	0.0	6.3	0.0	0.0	0.0		
SARP 11-10	29.1	21.8	0.0	7.3	0.5	0.0	0.5	0.0	0.0	0.0	0.0	0.0	62.5	0.3	0.0	0.0	3.7	0.0	4.0	0.0	0.0	0.0		
SARP 11-11	38.6	35.3	0.3	3.0	0.0	0.0	0.0	0.0	0.0	0.0	0.0	50.3	0.0	0.3	0.0	0.0	0.0	0.0	8.3	2.3	0.0	0.0		
SARP 12-10	35.0	29.3	1.7	4.0	0.3	1.7	2.0	0.0	0.0	0.0	0.0	0.0	49.6	6.0	0.0	0.0	4.3	0.0	0.0	2.0	0.0	0.0		
SARP 13-10	38.0	30.0	1.0	7.0	0.0	0.3	0.3	0.0	0.0	0.0	0.0	0.0	39.6	4.0	0.0	0.0	16.6	0.0	1.3	0.0	0.0	0.0		
SARP 14-10	43.6	34.6	0.7	8.3	0.3	0.8	1.0	0.0	0.0	0.0	0.0	0.0	40.0	6.0	0.0	0.0	6.0	0.0	3.3	0.0	0.0	0.0		
SARP 15-10	36.6	24.9	1.0	10.7	0.0	0.3	0.5	0.0	0.0	0.0	0.0	0.0	53.0	2.0	0.0	0.0	4.3	0.0	3.6	0.0	0.0	0.0		
SARP 16-10	34.3	27.3	0.0	7.0	0.0	0.0	0.0	0.0	0.0	0.0	0.0	0.0	58.3	5.6	0.0	0.0	0.6	0.0	1.0	13.0	0.0	0.0		

Und. Undulatory extinction. R.F: Rock fragment. H.M: Heavy mineral grain. ISO: Isotropic mineral grain. OPQ: Opaque mineral grain.

Illuv: Illuviation. CDNY: Chalcedony. POR: Porosity. FRACT: Fracture. SERZ: Seritization.

Appendix C – Mineral estimation from XRD

	% Quartz	% Opal	% Microcline	% Orthoclase	% Plagioclase	% Saponite	% Kaolinite	% Illite	% Mont.ill.	% Dolomite	% Calcite	% Apatite
SARP 1-11	14.2	0	43.8	3.9	31.6	0	0	0	0	0	3.9	0
SARP 1-10	37.1	0	0	48.8	0	0	0	2.6	1.46	0	10	
SARP 2-11	36.2	8.7	26.1	26.9	0	2.1	0	0	0	0	0	0
SARP 2-10	70.2	4.1	11.7	10.7	2.9	0	0	0.5	0	0	0	0
SARP 3-11	45.8	3.6	33.4	10.8	3.3	1.7	0	0	0	0	1.5	0
SARP 3-10	28.6	9.9	28.7	21.3	0	0	0	9.3	0	0	0	2.3
SARP 4-11	43.4	0	42.8	9.0	2.1	1.1	0	0	0	0	1.7	0
SARP 5-11	16.2	22.9	9.6	10.8	10.3	4.4	0	0	0	0	0	25.7
SARP 6-11	43.0	12.2	21.9	20.5	2.5	0	0	0	0	0	0	0
SARP 7-11	26.4	0	35.0	26.2	4.6	4.1	0	0	0	0	3.6	0
SARP 4-10	55.0	0	27.8	9.4	7.3	0	0	0.4	0	0	0	0
SARP 8-11	29.9	37.2	16.0	16.9	0	0	0	0	0	0	0	0
SARP 5-10	20.8	8.7	40.4	24.8	0	0	0	0.4	0	0	0	5.0
SARP 9-11	55.1	18.3	16.8	0	0	0	8.4	0	0	0	1.4	0
SARP 6-10	56.6	23.7	12.4	0	0	0	7.3	0	0	0	0	0
SARP 7-10	63.0	18.6	8.9	0	0	0	8.1	0	0.8	0	1.4	0
SARP 8-10	34.2	40.8	2.6	0	0	0	22.4	0	0	0	0	0
SARP 9-10	70.5	3.4	19.2	0	0	0	3.7	0	0	0.64	1.8	0
SARP 10-11	65.0	0	23.9	0	0	0	11.2	0	0	0	0	0
SARP 10-10	75.0	3.7	14.9	0	0	0	5.0	0	0	0	1.3	0
SARP 11-10	74.8	0	18.3	0	0	0	5.4	0	0	0	1.3	0
SARP 11-11	89.6	0	2.3	0	0	0	8.0	0	0	0	0	0
SARP 12-10	84.1	0	8.9	0	0	0	5.6	0	0	0	1.4	0
SARP 13-10	83.9	0	6.9	0	0	0	8.6	0	0	0	0.7	0
SARP 14-10	81.8	0	10.2	0	0	0	6.8	0	0	0.36	0.8	0
SARP 15-10	80.0	0	15.9	0	0	0	15.9	0	0	0	0	0
SARP 16-10	83.2	0	5.8	0	0	0	11.0	0	0	0	0	0

Appendix D – Element distribution

Analyte Symbol	Cu	Ni	Cr	Co	Se	Zn	Pb	Ag	Cd	As	Sn	Sb	Mo	B	Li	Be	V	Mn	Ga	Ge
Unit Symbol	ppm	ppm	ppm	ppm	ppm	ppm	ppm	ppm	ppm	ppm	ppm	ppm	ppm	ppm	ppm	ppm	ppm	ppm	ppm	ppm
Detection Limit	2	10	30	0.2	0.8	30	0.8	10	2	5	0.5	2	1	10	3	3	5	3	0.2	0.7
SARP 1-10	24	120	110	15.9	< 0.8	80	30.2	< 10	< 2	< 5	2.3	< 2	< 1	< 10	36	6	202	118	30.7	3.2
SARP 2-10	18	140	4520	18.3	0.8	40	6.6	< 10	< 2	< 5	8.7	< 2	4	< 10	15	< 3	503	167	11.4	2.2
SARP 3-10	15	190	510	17.4	0.9	70	9.3	< 10	< 2	< 5	0.8	< 2	< 1	< 10	22	5	695	90	19.4	2.8
SARP 4-10	13	70	710	8.1	1.2	40	8.1	< 10	< 2	< 5	1.6	< 2	3	< 10	16	< 3	105	107	13.6	3.2
SARP 5-10	13	80	170	12.6	1.7	90	20	< 10	< 2	< 5	1.1	< 2	< 1	< 10	34	6	512	184	24.3	2.8
SARP 6-10	45	70	340	17.3	< 0.8	70	15.7	< 10	< 2	< 5	1.9	< 2	1	< 10	33	< 3	47	85	17.5	3.2
SARP 7-10	12	80	280	14	1	70	15.1	< 10	< 2	< 5	< 0.5	< 2	< 1	< 10	41	< 3	37	68	20.6	2.3
SARP 8-10	14	40	100	5.7	< 0.8	70	22.2	< 10	< 2	< 5	1.8	< 2	< 1	< 10	59	3	44	32	29	2.3
SARP 9-10	11	20	430	4	< 0.8	30	21.5	< 10	< 2	< 5	< 0.5	< 2	1	< 10	29	< 3	22	63	16.7	2.8
SARP 10-10	11	20	310	4.6	< 0.8	50	20	< 10	< 2	< 5	2.5	< 2	< 1	< 10	42	< 3	25	72	18.5	2.4
SARP 11-10	15	20	290	3.2	0.8	40	34.3	< 10	< 2	< 5	1.8	< 2	2	< 10	35	< 3	26	82	18.9	2.4
SARP 12-10	18	30	490	3	1.3	< 30	38.5	20	< 2	< 5	2.3	< 2	3	< 10	29	< 3	14	67	14.2	2.2
SARP 13-10	13	20	250	3	1	30	24.1	20	< 2	< 5	3.6	< 2	2	< 10	30	< 3	12	58	17.6	2.4
SARP 14-10	12	20	270	3.2	< 0.8	30	26.7	< 10	< 2	< 5	3.9	< 2	1	< 10	35	< 3	14	63	20.2	2.8
SARP 15-10	12	20	280	2.9	< 0.8	40	28.1	< 10	< 2	< 5	3.4	< 2	1	< 10	42	< 3	10	113	23.1	3.1
SARP 16-10	15	20	190	2.9	< 0.8	50	29.6	< 10	< 2	< 5	3.2	< 2	< 1	< 10	44	< 3	24	61	22.9	3.1

SARP 2010 cont.

Analyte Symbol	Rb	Sr	Y	Nb	In	Te	Cs	Ba	La	Ce	Pr	Nd	Sm	Eu	Gd	Tb	Dy	Ho	Er	Tm
Unit Symbol	ppm	ppm	ppm	ppm	ppm	ppm	ppm	ppm	ppm	ppm	ppm	ppm	ppm	ppm	ppm	ppm	ppm	ppm	ppm	ppm
Detection Limit	0.4	3	0.1	2.4	0.2	6	0.1	3	0.4	0.8	0.1	0.4	0.1	0.1	0.1	0.1	0.3	0.2	0.1	0.1
SARP 1-10	260	106	8.7	15.3	< 0.2	< 6	5.2	1370	14.2	39.4	3.7	13.1	2.3	0.3	1.4	0.2	1.3	0.3	0.9	0.1
SARP 2-10	132	26	9.4	34.9	< 0.2	< 6	1.1	228	17.9	39.2	4.3	15	2.6	0.5	1.7	0.2	1.5	0.3	0.8	0.1
SARP 3-10	218	45	21.2	17.7	< 0.2	< 6	2.6	355	31	59.2	7.4	26.7	4.9	0.9	3.6	0.5	3.1	0.6	1.9	0.3
SARP 4-10	139	62	10.5	17.2	< 0.2	< 6	3	481	32.4	89.6	9.9	36.2	6.3	0.9	3.5	0.4	2.3	0.3	1	0.2
SARP 5-10	190	90	35	18.4	< 0.2	< 6	3.8	1080	43.4	78.7	10.2	36.9	7.1	1.2	5.2	0.8	5	1	2.8	0.4
SARP 6-10	30.2	34	19.1	20.3	< 0.2	< 6	2.5	510	41.3	98.7	9.5	33.8	5.6	0.9	3.5	0.5	3	0.5	1.6	0.2
SARP 7-10	39.1	36	8.9	21.8	< 0.2	< 6	3	527	25.9	39	4	11.9	1.8	0.3	1.2	0.2	1.2	0.2	0.7	0.1
SARP 8-10	19.6	39	2.6	22	< 0.2	< 6	3.4	267	20.7	28.4	2.8	7.9	1.1	0.2	0.7	< 0.1	0.5	< 0.2	0.3	< 0.1
SARP 9-10	51.1	36	14.3	17.1	< 0.2	< 6	2.3	1040	34	106	9.6	33	6	0.9	3.6	0.5	3	0.5	1.4	0.2
SARP 10-10	48.6	37	5.9	20	< 0.2	< 6	2.5	351	18.9	26.6	2.7	7.8	1.2	0.1	0.8	0.1	0.9	< 0.2	0.6	0.1
SARP 11-10	52.2	119	10.3	16.9	< 0.2	< 6	2.8	2360	20.3	35.7	3.2	9.4	1.6	0.1	1.1	0.2	1.4	0.3	1	0.2
SARP 12-10	33.8	125	4.9	16.2	< 0.2	< 6	2.4	2370	18.9	41.5	3	9	1.5	0.1	0.9	0.2	0.8	< 0.2	0.5	< 0.1
SARP 13-10	26.7	89	6.6	14.2	< 0.2	< 6	2	1590	17.8	31.1	2.8	8.1	1.3	0.2	0.9	0.2	1	< 0.2	0.6	0.1
SARP 14-10	25.3	91	7.3	22.8	< 0.2	< 6	2	1560	19.6	34.5	3.2	9	1.5	0.2	1	0.2	1.1	0.2	0.7	0.1
SARP 15-10	17.3	44	7.1	25.4	< 0.2	< 6	1.5	702	23.6	46.7	3.7	10.2	1.6	0.2	1.1	0.2	1.2	0.2	0.7	0.1
SARP 16-10	22.6	59	8.7	23	< 0.2	< 6	1.8	868	26.1	60.3	4.5	13.4	2.2	0.3	1.4	0.2	1.4	0.3	0.9	0.1

SARP 2010 cont.

Analyte Symbol	Yb	Hf	Ta	W	Tl	Bi	Th	U	Al	Ca	Fe	K	Mg	P	S	Si	Ti
Unit Symbol	ppm	ppm	ppm	ppm	ppm	ppm	ppm	ppm	%	%	%	%	%	%	%	%	%
Detection Limit	0.1	10	0.2	0.7	0.1	2	0.1	0.1	0.01	0.01	0.05	0.1	0.01	0.005	0.01	0.01	0.01
SARP 1-10	1.2	< 10	1.1	10.9	0.7	< 2	22.8	18.3	8.32	0.32	3.28	10	0.38	0.008	< 0.01	26.3	0.22
SARP 2-10	0.9	< 10	6.3	4.5	0.2	< 2	9.2	7.1	2.95	0.11	1.84	3.6	0.43	0.007	< 0.01	38.1	0.28
SARP 3-10	2	< 10	1.1	3.5	0.3	< 2	13.8	12.2	5.37	0.16	1.59	7.1	0.31	0.012	< 0.01	28.6	0.2
SARP 4-10	1.2	< 10	0.9	5.4	0.3	< 2	10.8	7.9	4.39	0.16	1.29	5.5	0.15	0.014	< 0.01	33.4	0.16
SARP 5-10	2.8	< 10	1.3	5.6	0.4	< 2	13.2	94.3	6.03	1.4	1.42	8.2	0.33	0.606	< 0.01	31.4	0.24
SARP 6-10	1.7	< 10	1.4	5.8	0.3	< 2	12.9	13.2	5.85	0.06	1.2	0.5	0.12	0.014	< 0.01	36.4	0.23
SARP 7-10	0.9	< 10	1.3	5.8	0.3	< 2	9.7	4	6.75	< 0.01	1.48	0.5	0.18	0.009	< 0.01	34	0.24
SARP 8-10	0.3	< 10	1.2	1.5	0.4	< 2	9.8	4.1	9.64	0.12	1.41	0.2	0.06	0.013	< 0.01	29.8	0.22
SARP 9-10	1.5	< 10	1	2.6	0.4	< 2	13.4	5.9	5.51	0.04	0.99	0.9	0.04	0.014	0.01	39.8	0.2
SARP 10-10	0.9	< 10	1.3	3	0.4	< 2	8.4	4.5	6.36	0.08	1.09	0.9	0.05	0.012	< 0.01	39.3	0.24
SARP 11-10	1.4	< 10	1.3	1.9	0.4	< 2	7.4	6.8	6.19	0.08	1.03	1	0.02	0.018	0.09	32.7	0.27
SARP 12-10	0.7	< 10	0.9	2.7	0.3	< 2	5.4	5.8	4.6	0.02	0.91	0.7	0.02	0.036	0.29	36.9	0.17
SARP 13-10	0.9	< 10	1.2	1.9	0.3	< 2	6.8	7.7	5.55	0.08	1.05	0.4	0.03	0.013	0.06	27.5	0.23
SARP 14-10	0.9	< 10	1.4	2.3	0.3	< 2	7.3	8.1	6.12	0.07	1.15	0.4	0.03	0.02	0.05	36	0.26
SARP 15-10	0.9	< 10	1.5	3.2	0.3	< 2	9.5	7.9	7.17	0.13	1.18	0.2	0.03	0.069	< 0.01	34.7	0.28
SARP 16-10	1.1	< 10	1.5	2.6	0.3	< 2	11.4	8.7	7.05	0.06	1.7	0.3	0.03	0.033	0.02	33.5	0.27

SARP 2011

Analyte Symbol Unit	Li ppm	Cd ppm	V ppm	Cr ppm	Mn ppm	Fe %	Hf ppm	Ni ppm	Er ppm	Be ppm	Ho ppm	Ag ppm	Cs ppm	Co ppm	Eu ppm	Bi ppm	Se ppm	Zn ppm	Ga ppm	Ge ppm
Detection Limit	0.5	0.1	1	0.5	1	0.01	0.1	0.5	0.1	0.1	0.1	0.05	0.05	0.1	0.05	0.02	0.1	0.2	0.1	0.1
SARP 11 BASE I	2.3	< 0.1	14	157	56	0.94	1.3	18.6	0.2	1.3	< 0.1	< 0.05	3.34	5.9	0.17	0.13	0.1	9.4	12.8	0.2
SARP 11 BASE II	10.8	< 0.1	26	60.3	116	1.96	2.8	49.8	1.5	7.1	0.6	< 0.05	8.07	8	1.53	0.52	0.5	42.6	28.1	0.4
SARP 1-11	10.6	< 0.1	78	131	64	2.09	2.1	59.7	0.5	2.7	0.1	< 0.05	5.25	7.3	0.16	0.26	< 0.1	22.2	14.4	0.3
SARP 2-11	23.4	< 0.1	167	115	61	1.83	0.5	96.3	0.5	4.1	0.2	< 0.05	4.09	11.1	0.37	0.43	< 0.1	58.7	17.9	0.2
SARP 3-11	18.1	< 0.1	126	497	81	1.56	4.8	74.4	0.7	1.9	0.3	< 0.05	4.36	9.6	0.66	0.37	0.2	50	13.1	< 0.1
SARP 4-11	20.4	< 0.1	103	196	156	1.07	0.1	83.1	1.5	9.2	0.6	< 0.05	4.78	9.8	1.85	0.29	0.2	46.8	11.5	0.5
SARP 5-11	4.3	0.5	68	650	284	3.51	< 0.1	448	9.6	15.3	3.5	< 0.05	3.35	37.8	7.21	0.08	2.5	55.7	12.5	0.4
SARP 6-11	30	< 0.1	32	187	92	1.17	0.5	76.2	1.5	1.7	0.5	< 0.05	3.42	13.8	1.05	0.31	< 0.1	54.6	14	0.2
SARP 7-11	29.1	< 0.1	108	128	140	1.65	1.1	168	1.4	5.5	0.5	< 0.05	4.65	20	0.58	0.41	< 0.1	111	24	0.2
SARP 8-11	13.7	< 0.1	391	248	72	1.13	1.4	48.1	0.5	1.4	0.2	< 0.05	3.37	6.2	0.2	0.17	< 0.1	40.3	8.4	< 0.1
SARP 9-11	10.3	< 0.1	328	224	79	1.19	1.2	38.5	0.4	1.5	0.1	< 0.05	2.99	5.3	0.17	0.17	< 0.1	32.6	7	< 0.1
SARP 10-11	34.4	0.1	19	59.4	53	0.93	4.3	21.4	0.5	1.8	0.2	< 0.05	3.55	2.6	0.2	0.27	0.2	28.1	17.4	0.2
SARP 11-11	13.3	< 0.1	16	111	49	1.23	0.6	21.1	0.7	1.5	0.3	< 0.05	2.29	2.6	0.39	0.32	< 0.1	27.5	15.8	0.4

SARP 2011 cont.

Analyte Symbol Unit	As ppm	Rb ppm	Y ppm	Sr ppm	Zr ppm	Nb ppm	Mo ppm	In ppm	Sn ppm	Sb ppm	Te ppm	Ba ppm	La ppm	Ce ppm	Pr ppm	Nd ppm	Sm ppm	Gd ppm	Tb ppm	Dy ppm
Detection Limit	0.1	0.2	0.1	0.2	1	0.1	0.1	0.1	1	0.1	0.1	1	0.1	0.1	0.1	0.1	0.1	0.1	0.1	0.1
SARP 11 BASE I	1.9	151	2.3	160	42	4.2	3.8	< 0.1	1	0.2	< 0.1	944	5.8	19.2	1.4	4.5	0.7	0.5	< 0.1	0.3
SARP 11 BASE II	1.7	133	16.8	670	120	1.8	< 0.1	< 0.1	2	< 0.1	< 0.1	1220	70.4	117	14.8	50.4	8.5	5.8	0.7	3.7
SARP 1-11	2.4	178	4.3	217	78	5.7	2.4	< 0.1	1	0.2	< 0.1	1510	3.6	10.4	0.9	3.3	0.7	0.7	0.1	0.6
SARP 2-11	0.5	98.8	4.9	79.3	38	12.4	1	< 0.1	2	< 0.1	< 0.1	1340	20.2	46.8	4.8	16.2	2.4	1.6	0.2	1
SARP 3-11	1.1	84.2	6	28.8	161	18.1	3.1	< 0.1	2	0.1	< 0.1	440	22.2	60.5	6.4	22.7	4.2	2.7	0.3	1.5
SARP 4-11	< 0.1	87.6	12.9	213	45	0.3	1.9	< 0.1	< 1	< 0.1	< 0.1	4990	51.4	145	15.9	60	10.4	7.7	0.9	4.3
SARP 5-11	1	43.2	112	225	< 1	< 0.1	2.5	< 0.1	< 1	< 0.1	< 0.1	1560	138	296	37.1	147	35.7	25.3	3.8	20.2
SARP 6-11	0.9	29.2	16.4	32.8	44	1.1	0.3	< 0.1	1	< 0.1	< 0.1	316	46.5	106	11	37.2	6.4	4.8	0.6	3.1
SARP 7-11	< 0.1	97.9	16.6	87.7	48	0.7	< 0.1	< 0.1	< 1	< 0.1	< 0.1	960	25.8	48.9	5.7	19.7	3.5	3.1	0.4	2.5
SARP 8-11	0.5	104	5	30.2	57	9.1	3	< 0.1	2	< 0.1	< 0.1	336	11.9	19.7	2.7	8.7	1.5	1.1	0.2	0.9
SARP 9-11	0.3	88.3	4	27.6	41	9.1	3	< 0.1	2	< 0.1	< 0.1	361	9.2	18.4	2.1	7	1.2	0.9	0.1	0.7
SARP 10-11	0.4	37.3	4.7	224	172	12.8	1.3	< 0.1	2	< 0.1	< 0.1	712	24.1	43	3.6	9.4	1.3	0.9	0.1	0.7
SARP 11-11	0.2	15.2	6.7	39.6	63	3.3	0.7	< 0.1	1	< 0.1	< 0.1	637	27.7	65.2	4.8	14.6	2.4	2	0.3	1.4

SARP 2011 cont.

Analyte Symbol	Cu	Tm	Yb	Lu	Ta	W	Tl	Pb	Sc	Th	U	Al	Ca	Fe	K	Mg	P	S	Ti	P
Unit	ppm	ppm	ppm	ppm	ppm	ppm	ppm	ppm	ppm	ppm	ppm	%	%	%	%	%	%	%	%	%
Detection Limit	0.2	0.1	0.1	0.1	0.1	0.1	0.05	0.5	1	0.1	0.1	0.01	0.01	0.01	0.01	0.01	0.001	0.01	0.0005	0.001
SARP 11 BASE I	6.7	<0.1	0.2	<0.1	<0.1	2.6	1	11.8	<1	6.8	1.7	6.72	0.13	0.94	2.93	0.09	0.003	<0.01	0.0376	0.003
SARP 11 BASE II	16.7	0.2	1.3	0.2	<0.1	1.3	0.62	29.7	2	15.3	17.4	9.81	1.54	1.96	1.74	0.34	0.055	0.01	0.139	0.055
SARP 1-11	9.5	<0.1	0.5	<0.1	0.2	5.2	1.13	21.2	2	13.6	8.9	6.95	0.22	2.09	4.68	0.14	0.005	<0.01	0.0814	0.005
SARP 2-11	9.4	<0.1	0.5	<0.1	0.5	5.8	0.25	10.2	3	7.2	26.1	5.04	0.19	1.83	3.89	0.26	0.059	<0.01	0.184	0.059
SARP 3-11	9.2	0.1	0.9	0.2	1.1	6.3	0.35	10.2	3	9.3	5.9	3.5	0.12	1.56	2.88	0.2	0.008	<0.01	0.212	0.008
SARP 4-11	9.9	0.2	1.4	0.2	<0.1	<0.1	0.44	12.3	4	13.5	67	4.41	0.23	1.07	3.05	0.19	0.172	0.01	0.0625	0.172
SARP 5-11	21.2	1.4	9.5	1.3	<0.1	<0.1	0.18	36.1	13	9.9	394	2.07	5.82	3.51	1.35	0.63	1.44	0.05	0.0078	1.44
SARP 6-11	9.2	0.2	1.6	0.3	<0.1	<0.1	0.3	20	5	15.4	7.6	5.51	0.07	1.17	0.45	0.15	0.005	<0.01	0.254	0.005
SARP 7-11	31.3	0.2	1.5	0.2	<0.1	<0.1	0.47	20.4	7	18.7	43.9	7.46	0.38	1.65	3.86	0.55	0.004	<0.01	0.0703	0.004
SARP 8-11	8.3	<0.1	0.6	<0.1	0.4	3	0.27	6.2	3	8.3	13.5	3.3	0.1	1.13	3.15	0.21	0.004	<0.01	0.185	0.004
SARP 9-11	6.9	<0.1	0.4	<0.1	0.4	3.3	0.21	6.5	3	7.8	40.6	3.17	0.1	1.19	3.31	0.14	0.004	<0.01	0.15	0.004
SARP 10-11	9.8	<0.1	0.6	0.1	0.4	1.2	0.4	33.6	4	6.5	6.9	5.95	0.13	0.93	0.72	0.04	0.032	0.31	0.274	0.032
SARP 11-11	10	0.1	0.8	0.1	0.3	0.2	0.25	31.6	4	11.1	12.1	6.45	0.07	1.23	0.22	0.03	0.039	0.02	0.221	0.039

Analyte Symbol	Cu	Ni	Cr	Co	Se	Zn	Pb	Ag	Cd	As	Sn	Sb	Mo	B	Li	Be	V	Mn	Ga
Unit Symbol	ppm	ppm	ppm	ppm	ppm	ppm	ppm	ppm	ppm	ppm	ppm	ppm	ppm	ppm	ppm	ppm	ppm	ppm	ppm
Detection Limit	2	10	30	0.2	0.8	30	0.8	10	2	5	0.5	2	1	10	3	3	5	3	0.2
CHIG I																			
CHIG 1-10	29	< 10	390	13.5	< 0.8	40	21.5	< 10	< 2	6	3	< 2	2	< 10	26	< 3	< 5	811	3.7
CHIG 2-10	7	< 10	30	4.9	< 0.8	50	15.3	< 10	< 2	< 5	2.6	< 2	< 1	< 10	33	< 3	< 5	235	3.6
CHIG 3-10	16	< 10	< 30	8.5	< 0.8	40	19.7	80	< 2	12	7.8	< 2	2	< 10	44	< 3	< 5	385	2.8
CHIG 4-10	7	< 10	70	3.3	< 0.8	30	14.6	10	< 2	9	3.7	< 2	< 1	< 10	20	< 3	< 5	304	2.8
CHIG 5-10	11	20	< 30	44.7	1.9	30	35	< 10	< 2	9	3.8	< 2	89	< 10	26	< 3	< 5	4550	3.3
CHIG 6-10	9	10	< 30	6.6	1.1	40	15.8	< 10	< 2	< 5	4	< 2	3	< 10	39	< 3	< 5	426	4
CHIG II																			
CHIG II 1-10	13	< 10	300	6.9	< 0.8	40	21.9	< 10	< 2	< 5	< 0.5	< 2	2	10	23	< 3	34	504	17.3
CHIG II 2-10	11	< 10	30	6.3	< 0.8	50	13.3	< 10	< 2	< 5	1.3	< 2	< 1	< 10	23	< 3	23	230	15.9
CHIG II 3-10	9	< 10	60	3	< 0.8	< 30	11.5	< 10	< 2	< 5	< 0.5	< 2	< 1	< 10	12	< 3	11	162	10.8
Analyte Symbol	Ge	Rb	Sr	Y	Nb	In	Te	Cs	Ba	La	Ce	Pr	Nd	Sm	Eu	Gd	Tb	Dy	Ho
Unit Symbol	ppm	ppm	ppm	ppm	ppm	ppm	ppm	ppm	ppm	ppm	ppm	ppm	ppm	ppm	ppm	ppm	ppm	ppm	ppm
Detection Limit	0.7	0.4	3	0.1	2.4	0.2	6	0.1	3	0.4	0.8	0.1	0.4	0.1	0.1	0.1	0.1	0.3	0.2
CHIG I																			
CHIG 1-10	2.7	106	101	12.4	8.7	< 0.2	< 6	4.5	597	16.4	45.7	3.7	12.9	2.6	0.6	1.8	0.3	1.9	0.4
CHIG 2-10	2.6	108	127	9	4.2	< 0.2	< 6	5.7	563	12	24.1	2.9	10.5	2.1	0.5	1.5	0.3	1.5	0.3
CHIG 3-10	2.4	104	174	8.4	4.4	< 0.2	< 6	5.6	650	9.8	54.3	2.3	7.7	1.5	0.4	0.9	0.2	1.3	0.3
CHIG 4-10	2.2	113	118	6.5	3.3	< 0.2	< 6	4.1	729	8.7	18.6	1.9	6.8	1.3	0.3	0.9	0.2	1	< 0.2
CHIG 5-10	3	95	104	17.9	4.9	< 0.2	< 6	4.7	2300	31.6	247	7.4	26.2	5.1	1	2.5	0.6	3.3	0.6
CHIG 6-10	3.1	91	156	12.6	4.6	< 0.2	< 6	5.3	937	16.8	50.2	3.6	12.7	2.5	0.4	1.8	0.3	2	0.4
CHIG II																			
CHIG II 1-10	1.8	106	101	12.4	4.5	< 0.2	< 6	4.1	701	14.1	44	3.1	11.3	2.3	0.5	1.6	0.3	1.8	0.4
CHIG II 2-10	1.8	99.4	75	8.2	3.8	< 0.2	< 6	4.1	516	9.5	28.9	2.2	8	1.7	0.3	1.2	0.2	1.3	0.2
CHIG II 3-10	1.8	99.2	75	8.2	< 2.4	< 0.2	< 6	3.3	579	8.9	20.4	2.1	7.4	1.5	0.3	1.1	0.2	1.2	0.2

Analyte Symbol	Er	Tm	Yb	Hf	Ta	W	Tl	Bi	Th	U	Al	Ca	Fe	K	Mg	P	S	Si	Ti
Unit Symbol	ppm	ppm	ppm	ppm	ppm	ppm	ppm	ppm	ppm	ppm	%	%	%	%	%	%	%	%	%
Detection Limit	0.1	0.1	0.1	10	0.2	0.7	0.1	2	0.1	0.1	0.01	0.01	0.05	0.1	0.01	0.005	0.01	0.01	0.01
CHIG I																			
CHIG 1-10	1	0.1	1	< 10	0.7	1.4	0.5	< 2	4.1	0.9	6.58	0.49	1.98	1.9	0.26	0.01	< 0.01	30.4	0.1
CHIG 2-10	0.8	0.1	0.8	< 10	0.5	< 0.7	0.5	< 2	6.2	1.1	7.37	0.72	2.18	2.1	0.3	0.008	0.02	30.2	0.15
CHIG 3-10	0.7	0.1	0.8	< 10	0.6	1	0.4	< 2	4.3	1.2	6.54	0.74	1.48	2.1	0.25	0.007	0.02	32.8	0.11
CHIG 4-10	0.6	< 0.1	0.7	< 10	0.4	3.7	0.5	< 2	4.2	0.9	5.23	0.47	1.44	2.5	0.14	0.007	0.01		0.08
CHIG 5-10	1.6	0.2	1.4	< 10	0.5	< 0.7	1.1	< 2	6.6	0.9	4.93	0.38	1.39	1.8	0.18	0.008	0.04		0.11
CHIG 6-10	1.1	0.2	1.4	< 10	0.4	< 0.7	0.5	< 2	7.7	0.7	7.1	0.66	1.98	1.8	0.17	0.008	0.02	31.6	0.12
CHIG II																			
CHIG II 1-10	1.1	0.1	1.2	< 10	0.3	0.9	0.6	< 2	4.8	1.1	6.59	0.49	1.46	2.8	0.22	0.009	< 0.01	29.3	0.1
CHIG II 2-10	0.7	< 0.1	0.8	< 10	0.4	< 0.7	0.5	< 2	5.6	1.5	5.89	0.41	1.28	2.2	0.2	0.007	< 0.01		0.11
CHIG II 3-10	0.7	< 0.1	0.8	< 10	0.4	< 0.7	0.5	< 2	3.3	0.8	4.14	0.29	1.36	2.7	0.09	0.005	< 0.01		0.07

APPENDIX E – Natural gamma radiation,
SARP

Height	Cps
Basement	180
0.2	330
0.38	320
0.62	250
1	1000
1.2	270
2.1	1000
2.4	1200
2.6	580
3.8	800
4.15	300
Cover	
8	200
11	150
12.6	180
12.3	150
15	150
16.95	160
19	270
21.2	140
22.5	110

Appendix F – Element correlation

	Cu	Ni	Cr	Co	Se	Zn	Pb	As	Sn	Mo	Li	V	Mn	Ga	Ge	Rb	Sr	Y	Nb	Cs	Ba	Ta	W	Tl	Th	U	REE	
Cu	1.00																											
Ni	0.53	1.00																										
Cr	0.13	0.12	1.00																									
Co	0.63	0.97	0.20	1.00																								
Se	0.30	0.71	0.15	0.68	1.00																							
Zn	0.69	0.20	-0.27	0.33	0.15	1.00																						
Pb	0.51	0.60	-0.32	0.65	0.49	0.34	1.00																					
As	0.20	0.09	-0.35	0.11	-0.45	0.23	0.18	1.00																				
Sn	0.11	-0.05	0.95	0.05	-0.01	-0.25	-0.34	-0.32	1.00																			
Mo	-0.30	0.00	0.60	-0.10	0.15	-0.73	-0.37	-0.40	0.57	1.00																		
Li	0.24	-0.38	-0.29	-0.21	-0.21	0.71	0.11	-0.01	-0.15	-0.74	1.00																	
V	-0.01	-0.04	0.38	-0.03	0.20	0.17	-0.40	-0.60	0.34	0.08	0.14	1.00																
Mn	0.48	0.77	0.26	0.81	0.81	0.25	0.56	-0.11	0.10	0.10	-0.20	-0.01	1.00															
Ga	0.58	0.01	-0.31	0.13	0.12	0.79	0.45	-0.01	-0.21	-0.68	0.78	0.14	0.02	1.00														
Ge	0.23	-0.04	0.25	0.00	0.47	0.21	-0.03	-0.79	0.23	0.02	0.34	0.54	0.13	0.48	1.00													
Rb	0.20	-0.22	-0.01	-0.22	0.11	0.21	0.03	-0.55	0.06	-0.10	0.37	0.53	-0.20	0.64	0.75	1.00												
Sr	0.10	0.41	-0.29	0.32	0.28	-0.15	0.60	0.22	-0.36	-0.02	-0.34	-0.44	0.45	-0.02	-0.22	-0.04	1.00											
Y	0.32	0.91	-0.03	0.87	0.83	0.15	0.66	0.01	-0.20	0.01	-0.36	-0.10	0.85	-0.06	-0.06	-0.30	0.48	1.00										
Nb	-0.05	-0.22	0.71	-0.17	0.14	-0.11	-0.48	-0.63	0.75	0.48	0.05	0.64	-0.10	0.06	0.62	0.47	-0.57	-0.31	1.00									
Cs	0.04	-0.21	-0.77	-0.24	-0.33	0.20	0.43	0.47	-0.63	-0.43	0.29	-0.57	-0.22	0.40	-0.32	0.13	0.51	-0.15	-0.60	1.00								
Ba	-0.08	0.03	-0.26	-0.02	-0.06	-0.06	0.18	0.16	-0.27	-0.10	-0.02	-0.33	0.26	-0.05	-0.20	-0.09	0.74	0.09	-0.47	0.49	1.00							
Ta	0.12	-0.03	0.96	0.07	0.12	-0.16	-0.35	-0.46	0.96	0.52	-0.08	0.52	0.15	-0.11	0.41	0.20	-0.40	-0.16	0.85	-0.70	-0.31	1.00						
W	-0.04	-0.36	0.04	-0.35	0.01	-0.02	-0.03	-0.46	0.23	0.15	0.30	0.20	-0.35	0.48	0.55	0.73	-0.23	-0.39	0.60	0.18	-0.25	0.26	1.00					
Tl	0.02	-0.31	-0.32	-0.32	-0.30	-0.12	0.32	0.14	-0.25	-0.14	0.09	-0.26	-0.31	0.32	-0.02	0.48	0.48	-0.31	-0.22	0.69	0.23	-0.25	0.34	1.00				
Th	0.59	-0.03	-0.31	0.10	-0.08	0.57	0.53	0.04	-0.26	-0.62	0.66	-0.13	0.02	0.76	0.31	0.46	0.15	-0.11	-0.25	0.48	0.14	-0.22	0.16	0.50	1.00			
U	0.30	0.88	-0.06	0.83	0.77	0.10	0.66	0.09	-0.21	0.05	-0.41	-0.20	0.85	-0.10	-0.16	-0.34	0.59	0.98	-0.38	-0.03	0.23	-0.21	-0.39	-0.26	-0.14	1.00		
REE	0.18	0.82	-0.06	0.78	0.72	0.03	0.56	0.04	-0.25	0.03	-0.38	-0.27	0.82	-0.21	-0.13	-0.47	0.52	0.93	-0.42	-0.11	0.30	-0.24	-0.51	-0.38	-0.14	0.93	1.00	

Correlation coefficients for FA1

	Cu	Ni	Cr	Co	Se	Zn	Pb	As	Sn	Mo	Li	V	Mn	Ga	Ge	Rb	Sr	Y	Nb	Cs	Ba	Ta	W	Tl	Th	U	REE	
Cu	1.00																											
Ni	0.54	1.00																										
Cr	0.29	0.14	1.00																									
Co	0.78	0.93	0.34	1.00																								
Se	0.33	0.43	0.50	0.51	1.00																							
Zn	0.55	0.76	0.03	0.75	0.71	1.00																						
Pb	-0.12	-0.47	-0.43	-0.43	-0.03	-0.23	1.00																					
As	-0.25	-0.37	-0.66	-0.43	-0.69	-0.56	0.66	1.00																				
Sn	0.12	-0.34	-0.43	-0.23	-0.46	-0.06	0.08	0.27	1.00																			
Mo	-0.33	-0.11	-0.18	-0.25	-0.79	-0.47	-0.57	0.14	0.26	1.00																		
Li	0.08	0.09	-0.30	0.07	0.63	0.64	0.48	-0.16	0.01	-0.77	1.00																	
V	-0.23	0.02	-0.08	-0.11	-0.65	-0.30	-0.72	-0.06	0.23	0.98	-0.72	1.00																
Mn	0.40	0.32	0.63	0.48	-0.07	-0.07	-0.60	-0.23	0.06	0.32	-0.69	0.36	1.00															
Ga	0.12	0.14	-0.28	0.10	0.65	0.64	0.47	-0.17	-0.12	-0.77	0.98	-0.72	-0.73	1.00														
Ge	0.57	0.34	0.64	0.53	0.92	0.63	-0.07	-0.72	-0.33	-0.74	0.48	-0.60	0.08	0.51	1.00													
Rb	-0.43	-0.25	0.23	-0.31	-0.59	-0.62	-0.59	-0.01	0.08	0.86	-0.87	0.83	0.53	-0.90	-0.55	1.00												
Sr	-0.20	-0.36	-0.64	-0.40	-0.53	-0.46	0.79	0.98	0.22	-0.06	0.01	-0.26	-0.32	0.00	-0.57	-0.19	1.00											
Y	0.76	0.39	0.74	0.64	0.44	0.20	-0.14	-0.33	-0.37	-0.37	-0.19	-0.30	0.56	-0.11	0.66	-0.19	-0.27	1.00										
Nb	0.39	0.43	0.23	0.50	0.94	0.83	0.11	-0.56	-0.24	-0.84	0.82	-0.71	-0.23	0.82	0.85	-0.77	-0.39	0.29	1.00									
Cs	-0.34	0.00	-0.97	-0.26	-0.45	0.00	0.38	0.63	0.21	0.18	0.27	0.09	-0.64	0.28	-0.64	-0.22	0.61	-0.71	-0.21	1.00								
Ba	-0.06	-0.27	0.42	-0.17	0.03	-0.53	0.39	0.24	-0.62	-0.25	-0.28	-0.35	0.05	-0.18	0.12	0.02	0.29	0.50	-0.17	-0.33	1.00							
Ta	0.52	0.48	0.48	0.61	0.95	0.81	-0.13	-0.73	-0.19	-0.72	0.61	-0.56	0.07	0.59	0.93	-0.59	-0.59	0.47	0.94	-0.48	-0.18	1.00						
W	0.58	0.85	0.56	0.92	0.46	0.56	-0.61	-0.51	-0.31	-0.08	-0.18	0.05	0.71	-0.17	0.46	0.02	-0.51	0.63	0.35	-0.46	-0.09	0.54	1.00					
Tl	-0.15	-0.55	-0.12	-0.45	0.33	-0.07	0.85	0.20	0.01	-0.74	0.67	-0.82	-0.64	0.65	0.31	-0.62	0.37	-0.09	0.41	0.04	0.31	0.23	-0.59	1.00				
Th	0.58	0.29	0.75	0.48	0.63	0.31	-0.20	-0.63	-0.52	-0.43	0.06	-0.30	0.21	0.17	0.83	-0.27	-0.55	0.84	0.47	-0.70	0.43	0.60	0.43	0.06	1.00			
U	-0.08	0.02	-0.03	-0.04	-0.70	-0.35	-0.68	0.01	0.27	0.96	-0.81	0.97	0.48	-0.80	-0.58	0.82	-0.19	-0.14	-0.76	0.02	-0.26	-0.58	0.10	-0.83	-0.23	1.00		
REE	0.64	0.16	0.64	0.41	0.38	0.04	0.11	-0.19	-0.44	-0.45	-0.10	-0.42	0.29	0.01	0.62	-0.28	-0.11	0.93	0.24	-0.61	0.69	0.35	0.34	0.16	0.87	-0.26	1.00	

Correlation coefficients for FA2

	Cu	Ni	Cr	Co	Se	Zn	Pb	As	Sn	Mo	Li	V	Mn	Ga	Ge	Rb	Sr	Y	Nb	Cs	Ba	Ta	W	Tl	Th	U	REE	
Cu	1.00																											
Ni	0.68	1.00																										
Cr	0.79	0.78	1.00																									
Co	0.43	-0.03	0.52	1.00																								
Se	0.81	0.52	0.86	0.63	1.00																							
Zn	0.28	-0.34	-0.15	0.11	0.10	1.00																						
Pb	0.64	0.76	0.54	-0.02	0.19	-0.01	1.00																					
As	-0.60	-0.06	-0.60	-0.80	-0.86	-0.42	0.11	1.00																				
Sn	0.01	-0.27	0.15	0.48	0.51	0.20	-0.67	-0.72	1.00																			
Mo	0.82	0.74	0.85	0.42	0.79	-0.22	0.55	-0.44	-0.08	1.00																		
Li	0.35	-0.25	0.22	0.52	0.51	0.78	-0.22	-0.84	0.69	-0.03	1.00																	
V	0.33	-0.19	-0.20	0.20	-0.14	0.60	0.35	-0.04	-0.37	0.00	0.19	1.00																
Mn	0.05	-0.12	0.29	0.23	0.23	0.39	0.01	-0.44	0.24	-0.01	0.59	-0.19	1.00															
Ga	-0.22	-0.67	-0.34	0.17	-0.06	0.76	-0.52	-0.41	0.58	-0.59	0.81	0.15	0.53	1.00														
Ge	0.38	-0.17	0.35	0.64	0.65	0.62	-0.28	-0.92	0.81	0.09	0.97	0.04	0.54	0.71	1.00													
Rb	0.61	0.17	0.48	0.71	0.43	0.12	0.48	-0.44	-0.21	0.64	0.16	0.58	0.10	-0.22	0.17	1.00												
Sr	0.74	0.51	0.76	0.75	0.71	-0.19	0.47	-0.53	0.00	0.86	0.06	0.23	-0.08	-0.46	0.19	0.85	1.00											
Y	-0.05	-0.66	-0.40	0.35	-0.25	0.65	-0.09	-0.17	-0.07	-0.30	0.41	0.80	0.20	0.54	0.27	0.48	0.01	1.00										
Nb	0.28	-0.16	0.32	0.57	0.53	0.60	-0.24	-0.83	0.77	-0.05	0.95	-0.01	0.62	0.77	0.96	0.06	0.08	0.24	1.00									
Cs	0.35	0.32	0.24	0.26	0.00	-0.28	0.65	0.18	-0.68	0.52	-0.47	0.53	-0.33	-0.66	-0.47	0.78	0.67	0.24	-0.53	1.00								
Ba	0.72	0.51	0.75	0.72	0.66	-0.21	0.51	-0.48	-0.08	0.86	0.02	0.24	-0.04	-0.49	0.13	0.88	0.99	0.03	0.02	0.72	1.00							
Ta	0.24	-0.36	0.19	0.66	0.51	0.65	-0.38	-0.88	0.79	-0.03	0.96	0.13	0.54	0.79	0.98	0.21	0.14	0.44	0.94	-0.43	0.09	1.00						
W	0.52	0.17	0.60	0.51	0.76	0.49	-0.02	-0.88	0.69	0.28	0.87	-0.16	0.65	0.52	0.91	0.11	0.23	-0.03	0.92	-0.46	0.19	0.82	1.00					
Tl	0.45	-0.13	0.32	0.75	0.36	0.39	0.25	-0.56	-0.02	0.40	0.44	0.59	0.39	0.17	0.41	0.91	0.63	0.71	0.32	0.52	0.66	0.49	0.29	1.00				
Th	-0.53	-0.53	-0.82	-0.68	-0.75	0.48	-0.24	0.52	-0.20	-0.83	0.02	0.26	-0.04	0.50	-0.19	-0.58	-0.87	0.33	-0.09	-0.41	-0.87	-0.10	-0.30	-0.38	1.00			
U	-0.80	-0.43	-0.88	-0.77	-0.94	-0.16	-0.28	0.88	-0.39	-0.78	-0.55	-0.01	-0.40	0.01	-0.66	-0.65	-0.80	0.02	-0.56	-0.17	-0.78	-0.57	-0.75	-0.62	0.78	1.00		
REE	0.34	0.72	0.16	-0.61	-0.07	-0.21	0.69	0.51	-0.66	0.33	-0.56	0.07	-0.44	-0.67	-0.61	-0.12	0.02	-0.49	-0.60	0.32	0.03	-0.74	-0.35	-0.42	0.09	0.20	1.00	

Correlation coefficients for FA3